SLAC-R-602

Parity Violation in Decays of Z Bosons into Heavy Quarks at SLD

T. R. Wright

Stanford Linear Accelerator Center
Stanford University
Stanford, CA 94309

SLAC-Report-602
September 2002

Prepared for the Department of Energy
under contract number DE-AC03-76SF00515

---

*Ph.D. thesis, University of Wisconsin-Madison

Parity Violation in Decays of Z Bosons into Heavy Quarks at SLD

by

Thomas R. Wright

A dissertation submitted in partial fulfillment of the requirements for the degree of

Doctor of Philosophy

(Physics)

at the

UNIVERSITY OF WISCONSIN-MADISON

2001

Abstract

This work presents measurements of the parity-violation parameters A_c and A_b made at the Z pole. These measurements include the data taken with the SLD detector at the SLAC Linear Collider (SLC) during the period 1996-98. Heavy flavor events are selected with high efficiency and purity by searching for displaced vertices, identified with the SLD precision CCD vertex detector. Two methods are used for quark/antiquark discrimination: the net charge of the displaced vertex, and tracks in the displaced vertex identified as kaons by the SLD Cherenkov Ring Imaging Detector (CRID). The signal purities and analyzing powers are calibrated from the data to reduce the systematic errors and avoid experimental bias. The results are $A_c = 0.673 \pm 0.029 \pm 0.023$ and $A_b = 0.919 \pm 0.018 \pm 0.017$, where the first error is statistical and the second systematic. Fits to the electroweak data performed by the LEP Electroweak Working Group are used to study the consistency of the Standard Model, and to constrain the mass of the Standard Model Higgs boson.

Acknowledgments

Many people have contributed to the completion of this Thesis. I thank all of the SLD and SLC physicists and technical staff for making the experimental program successful. Without their efforts this work would not have been possible.

Special thanks to my advisor Dick Prepost for supporting me all of these years and allowing me to work on so many interesting projects. Thanks also to Henry Band and Jim Johnson for reminding me that physics is more than just data analysis, and to Sridhara Dasu for valuable discussions on the nature of the high-energy business. Working with the Wisconsin group has been a privilege that I will not forget.

Among the SLD physicists, I would like to especially thank a few who have gone out of their way to help me. Thanks first of all to Bruce Schumm for running enjoyable and productive analysis group meetings, and for his enthusiasm about this work. Nicolo de Groot was very generous with his time when I was first starting SLD data analysis. Su Dong always knew what to try next when I ran into problems. John Jaros has a sixth sense for developing attitude problems and knew when a pep talk was in order. Thanks also to Peter Rowson and Richard Dubois for important baseball-related discussions. I count myself very lucky to have worked in such a friendly and supportive collaboration.

Thanks to all of the SLD students I have worked with: Aaron, Cheng-Ju, Danning, Gavin, Giulia, Hermann, Hyejoo, Jodi, John, Jorge, Julia, Matt, Sean, Thomas, and Vincenzo. I could not have asked for a nicer group of colleagues. Special thanks to Aaron and Hyejoo for helping me get out of the house once in awhile and keeping me current on the latest videogame and Food Network developments.

I thank my brother Scott for quitting a well-paying job and going back to school, his decision made me feel better about my own lack of career progress. I also thank Catherine and him for their invitations to have some fun in the big city. Above all I thank my parents. Their encouragement to continue my education and pride in me inspired this work. To them I dedicate this Thesis.

Contents

List of Figures

List of Tables

Chapter 1

Introduction

Until 1956 the invariance of physical law under parity transformations ($\vec{x} \rightarrow -\vec{x}$) had gone unchallenged. In that year, Lee and Yang [1] proposed parity violation in the weak interactions as a solution to the $\tau - \theta$ puzzle. Two particles, at that time called τ and θ (now K^+), had been discovered which appeared to have the same mass, spin, charge, etc. However, the θ decayed into two pions, while the τ decayed to three pions, states with opposite parity. Lee and Yang proposed that the τ and θ were in fact the same particle, and that both decay modes are allowed through violation of parity invariance in weak interactions. At that time there was much evidence for parity invariance in strong and electromagnetic interactions, but no direct tests for the weak force. Lee and Yang proposed a test involving the β-decay of polarized Co^{60} nuclei, and in 1957 C.S. Wu reported [2] her results, which showed that Lee and Yang were right. Confirmation of parity violation was reported in a study of μ decay [3] soon afterwards.

These results involved only the charged weak currents. In 1973 neutral weak currents, which had been predicted by the theory now known as the Standard Model, were discovered in elastic $\nu_\mu - e^-$ scattering at CERN [4]. A few years later, using an innovative polarized e^- beam, parity violation in neutral weak currents was demonstrated at SLAC in deep inelastic e-D scattering [5]. This effect has subsequently been observed in lepton scattering off a variety of atomic nuclei [6, 7, 8]. Parity violation has also been seen in the atomic transitions of Cs [9] and Tl [10]. The E158 experiment [11] currently in progress at SLAC aims to measure a parity-violating asymmetry in polarized Møller e^-e^- scattering.

All of the neutral weak current experiments described above suffer from contamination by the parity-conserving electromagnetic current. At low energies, the weak interaction is only a small part of the total neutral current, so the parity-violating effects are extremely diluted. Using higher energy processes, such as e^+e^- annihilation at $\sqrt{s} \sim M_Z$, it is possible to study the neutral weak current with very little electromagnetic contamination. The results presented in this Thesis comprise just such a study.

1.1 The Standard Model

The theory of elementary particles and their interactions which has come to be known as the Standard Model began with the unification of the electromagnetic and weak interactions by Glashow [12], Weinberg [13], and Salam [14]. Detailed descriptions of the theory can be found in [15] and [16]. In this Section a brief overview will be presented.

The fundamental particles within the Standard Model are the quarks and leptons which make up ordinary matter, and the gauge bosons which mediate their interactions. The quarks and leptons, which are all spin-$\frac{1}{2}$ fermions, are summarized in Table 1.1. They are grouped into three generations, and within each family the leptons and quarks are organized into left-handed doublets and right-handed singlets. The electric charge Q is related to the third component of the weak isospin T_3 and the weak hypercharge Y by:

$$Q = T_3 + \frac{Y}{2}. \tag{1.1}$$

Table 1.1: The three fermion families and select quantum numbers.

1^{st}	2^{nd}	3^{rd}	Q	T_3	Y
$\begin{pmatrix} \nu_e \\ e \end{pmatrix}_L$	$\begin{pmatrix} \nu_\mu \\ \mu \end{pmatrix}_L$	$\begin{pmatrix} \nu_\tau \\ \tau \end{pmatrix}_L$	$\begin{pmatrix} 0 \\ -1 \end{pmatrix}$	$\begin{pmatrix} +\frac{1}{2} \\ -\frac{1}{2} \end{pmatrix}$	$\begin{pmatrix} -1 \\ -1 \end{pmatrix}$
$\begin{pmatrix} u \\ d \end{pmatrix}_L$	$\begin{pmatrix} c \\ s \end{pmatrix}_L$	$\begin{pmatrix} t \\ b \end{pmatrix}_L$	$\begin{pmatrix} +\frac{2}{3} \\ -\frac{1}{3} \end{pmatrix}$	$\begin{pmatrix} +\frac{1}{2} \\ -\frac{1}{2} \end{pmatrix}$	$\begin{pmatrix} +\frac{1}{3} \\ -\frac{1}{3} \end{pmatrix}$
e_R	μ_R	τ_R	-1	0	-2
u_R	c_R	t_R	$+\frac{2}{3}$	0	$+\frac{4}{3}$
d_R	s_R	b_R	$-\frac{1}{3}$	0	$-\frac{2}{3}$

Table 1.2: Gauge bosons of the Standard Model.

boson	spin	mass	force
γ	1	0	electromagnetic
$W^\pm$	1	80 GeV/c^2	weak
Z	1	91 GeV/c^2	weak
gluon	1	0	strong

Because the neutrino is assumed to be massless in the Standard Model, there is no right-handed neutrino singlet. Recent evidence of neutrino oscillations [17, 18], however, indicate nonzero neutrino masses. It is not yet clear what modifications to the Standard Model are required to accomodate this new information.

The gauge bosons which mediate the interactions between quarks and leptons are listed in Table 1.2. The photon (γ) carries the electromagnetic force, the $W^\pm$ and Z bosons are responsible for weak interactions, and the gluons carry the strong force. Not listed is the graviton, which is thought to carry the gravitational force. Gravity has not been incorporated into the Standard Model, but its effects are neglible in most particle physics contexts. The neutrinos are affected only by the weak interactions, the charged leptons also feel the electromagnetic force, and the quarks participate in all three interactions.

1.1.1 Electroweak Interactions

The Dirac Lagrangian for a free particle can be written as:

$$\mathcal{L} = i\bar{\psi}\gamma^{\mu}\partial\psi - m\bar{\psi}\psi \tag{1.2}$$

where ψ is the spinor of wavefunctions, $\bar{\psi} = \psi^{\dagger}\gamma^{0}$ is its adjoint, the γ^{μ} are the Dirac matrices, and m is the mass of the particle. This Lagrangian is invariant under global gauge transformations $\psi \rightarrow e^{i\theta}\psi$, with θ real. However, if invariance under local gauge transformations $\psi \rightarrow e^{i\theta(x)}\psi$ is demanded, the derivatives introduce extra terms which must be compensated by adding an interaction term:

$$-iQ\bar{\psi}\gamma_{\mu}\psi A^{\mu} = -iQj_{\mu}^{em}A^{\mu} \tag{1.3}$$

in which the fermion fields ψ are coupled to a vector field A^{μ} through the current j_{μ}^{em}, with strength proportional to the fermion charge Q. The vector field A^{μ} is then identified with the electromagnetic field, and in this way quantum electrodynamics can be derived from the free-particle Langrangian.

In the electroweak Standard Model, the Lagrangian for the left-handed doublets is required to be invariant under local SU(2) rotations, and also under U(1) hypercharge transformations. This introduces analogous current terms:

$$-ig(J^{i})^{\mu}W_{\mu}^{i} - \frac{1}{2}ig'(j^{Y})^{\mu}B_{\mu} \tag{1.4}$$

where the W_{μ}^{i} are an SU(2) triplet of vector fields coupling with strength g to the weak isospin currents J_{μ}^{i}, and B_{μ} is a U(1) isosinglet vector field coupling with strength g' to the weak hypercharge current j_{μ}^{Y}.

The gauge bosons listed in Table 1.2 are linear combinations of these fields:

$$A_\mu = B_\mu \cos\theta_W + W_\mu^3 \sin\theta_W \tag{1.5}$$

$$Z_\mu = -B_\mu \sin\theta_W + W_\mu^3 \cos\theta_W \tag{1.6}$$

$$W_\mu^\pm = \frac{1}{\sqrt{2}}(W_\mu^1 \mp iW_\mu^2) \tag{1.7}$$

where θ_W is known as the weak mixing angle. Rewriting the neutral part of the electroweak interaction term as:

$$-i(g\sin\theta_W J_\mu^3 + \frac{1}{2}g'\cos\theta_W j_\mu^Y)A^\mu - i(g\cos\theta_W J_\mu^3 - \frac{1}{2}g'\sin\theta_W j_\mu^Y)Z^\mu \tag{1.8}$$

and comparing the first term with the electromagnetic interaction, the identifications:

$$j_\mu^{em} = J_\mu^3 + \frac{1}{2}j_\mu^Y \tag{1.9}$$

$$g\sin\theta_W = g'\cos\theta_W = Q \tag{1.10}$$

can be made, so that the weak mixing angle is given by $\tan\theta_W = g'/g$. The second term representing the weak neutral current then gives:

$$J_\mu^{NC} = J_\mu^3 - j_\mu^{em}\sin^2\theta_W \tag{1.11}$$

.

Replacing the current densities with their expressions in terms of the fermion fields, the factor for a $Zf\bar{f}$ vertex is given by:

$$-i\frac{g}{\cos\theta_W}J_\mu^{NC}Z^\mu = -i\frac{g}{\cos\theta_W}\bar{\psi}_f\gamma^\mu(\frac{1}{2}(1-\gamma^5)T_3 - Q\sin^2\theta_W)\psi_f Z_\mu \tag{1.12}$$

$$= \quad -i\frac{g}{2\cos\theta_W}\gamma^\mu(v_f - a_f\gamma^5) \tag{1.13}$$

where $\gamma^5 = i\gamma^0\gamma^1\gamma^2\gamma^3$, and v_f and a_f are the vector and axial-vector couplings at this vertex, respectively. These couplings are therefore firmly predicted by the Standard Model:

$$v_f \quad = \quad g_{Lf} + g_{Rf} \;=\; T_{3,f} - 2Q_f\sin^2\theta_W \tag{1.14}$$

$$a_f \quad = \quad g_{Lf} - g_{Rf} \;=\; T_{3,f} \tag{1.15}$$

once $\sin^2\theta_W$ is known. Also given are the relations to the commonly used g_{Lf} and g_{Rf}, the left- and right-handed couplings. This addition of a vector to an axial vector is the source of the parity violation in the neutral weak current, since they transform differently under $\vec{x} \to -\vec{x}$.

The principle of local gauge invariance has allowed the derivation of the structure and strength of the neutral weak interaction, but one problem remains. The vector fields which are introduced must be massless, otherwise the gauge invariance is spoiled. However, it is known that the $W^\pm$ and Z bosons are quite massive. This situation is resolved through the Higgs mechanism [19]. A doublet of scalar fields is introduced, which have nonzero vacuum expectation values. This is used to spontaneously break the $SU(2)_L \otimes U(1)_Y$ symmetry of the theory, in such a way that A_μ remains massless, $W^\pm_\mu$ and Z^μ acquire mass terms in the Lagrangian, and the gauge invariance is preserved. These Higgs fields should have associated quanta, or particles, which so far have not been observed. Understanding the nature of this spontaneous symmetry breaking is one of the top priorities of particle physics.

Figure 1.1: The tree-level diagrams for s-channel e^+e^- annihilation.

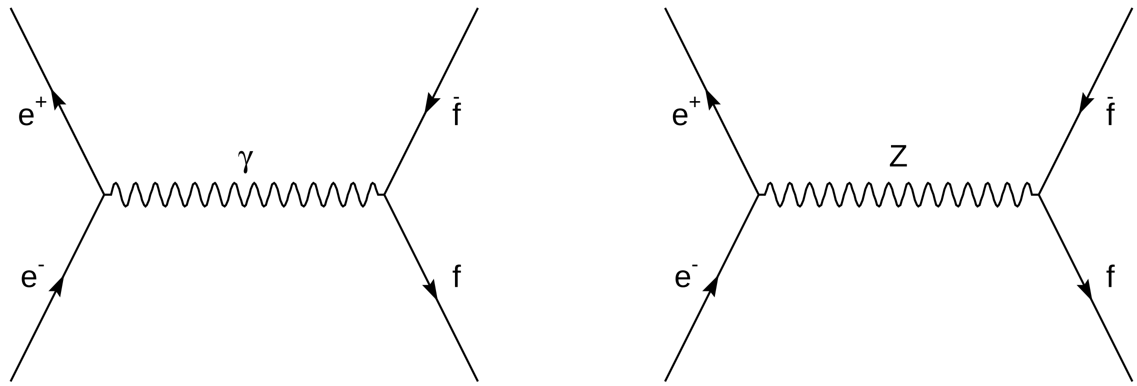

1.2 Electron-Positron Annihilation at $\sqrt{s} \sim M_Z$

The process $e^+e^- \to Z/\gamma \to f\bar{f}$, where f is a fermion (other than an electron), at tree level can only go through s-channel production of a virtual Z or γ. The Feynman diagrams for these two processes are shown in Figure 1.1.

The differential cross section for a reaction expresses the rate for that process into a particular region of the final state phase space. For annihilation in the center of momentum frame, it can be written as:

$$\frac{d\sigma}{d\Omega} = \frac{1}{64\pi^2 s}\frac{p_f}{p_e}|\mathcal{M}_Z + \mathcal{M}_\gamma|^2 \tag{1.16}$$

where $\mathcal{M}_Z$ and $\mathcal{M}_\gamma$ are the matrix elements for Z and γ exchange, $\sqrt{s}$ is the total energy, and p_e and p_f are the magnitudes of the incoming electron and outgoing fermion momenta.

The matrix element $\mathcal{M}_Z$ can be written as:

$$\mathcal{M}_Z = -\frac{g^2}{4\cos^2\theta_W}[\bar{f}\gamma^\nu(v_f - a_f\gamma^5)f]\frac{g_{\nu\mu} - k_\nu k_\mu/M_Z^2}{k^2 - M_Z^2 + iM_Z\Gamma_Z}[\bar{e}\gamma^\mu(v_e - a_e\gamma^5)e] \tag{1.17}$$

where e and f are the electron and fermion spinors, M_Z and Γ_Z are the mass and width of the Z, and k is the four-momentum of the virtual Z. From this, differential cross sections for left- and right-handed electrons can be calculated [20], averaging over the positron spin and summing the final-stage fermion spins:

$$\frac{d\sigma_L}{d\Omega} \propto (g_{Lf}^2 + g_{Rf}^2)(1 + \cos^2\theta_f) + 2(g_{Lf}^2 - g_{Rf}^2)\cos\theta_f \tag{1.18}$$

$$\frac{d\sigma_R}{d\Omega} \propto (g_{Lf}^2 + g_{Rf}^2)(1 + \cos^2\theta_f) - 2(g_{Lf}^2 - g_{Rf}^2)\cos\theta_f \tag{1.19}$$

where $L(R)$ refers to the electron helicity and θ_f is the angle between the incoming electron and the outgoing fermion.

For an electron beam with polarization P_e, the left- and right-handed differential cross sections can be expressed together as:

$$\frac{d\sigma}{d\Omega} \propto (1 - A_e P_e)(1 + \cos^2\theta_f) + 2(A_e - P_e)A_f \cos\theta_f \tag{1.20}$$

using the asymmetry parameters A_e and A_f, given by:

$$A_f = \frac{g_{Lf}^2 - g_{Rf}^2}{g_{Lf}^2 + g_{Rf}^2} = \frac{2v_f a_f}{v_f^2 + a_f^2}. \tag{1.21}$$

Values of A_f for the various fermion species are shown in Table 1.3, along with their dependence on $\sin^2\theta_W$ (a value of $\sin^2\theta_W = 0.231$ was used). Because of their large dependence, measurements of leptonic coupling asymmetries are sensitive probes of the value of $\sin^2\theta_W$. The quark coupling asymmetries, which are less dependent upon $\sin^2\theta_W$, provide tests of the flavor structure of the Standard Model.

Complementary to the coupling asymmetry is the partial width into a fermion type f:

$$\Gamma_f \propto a_f^2 + v_f^2 \propto g_{Lf}^2 + g_{Rf}^2 \tag{1.22}$$

Table 1.3: Coupling asymmetries A_f for the fermions.

fermion	A_f	$\partial A_f / \partial \sin^2 \theta_W$
ν_e, ν_μ, ν_τ	1	0
e, μ, τ	0.151	-7.86
u, c, t	0.669	-3.45
d, s, b	0.936	-0.64

Table 1.4: Measured values of the Z branching ratios.

fermion	Γ_f/Γ_Z (%)
e^+e^-	3.367±0.005
$\mu^+\mu^-$	3.367±0.008
$\tau^+\tau^-$	3.371±0.009
invisible ($\nu\bar{\nu}$)	20.02±0.06
hadrons	69.89±0.07
$(u\bar{u} + c\bar{c})/2$	10.1±1.1
$(d\bar{d} + s\bar{s} + b\bar{b})/3$	16.6±0.6
$c\bar{c}$	11.68±0.34
$b\bar{b}$	15.13±0.05

which is proportional to the total strength of the vertex couplings. The measured branching ratios Γ_f/Γ_Z [21] for various fermions are given in Table 1.4. For quarks what is commonly measured is the related quantity $R_f = \Gamma_f/\Gamma_{\text{hadrons}}$, the hadronic partial width. Measuring both R_f and A_f allows extraction of the two couplings g_{Lf} and g_{Rf}.

The total cross section for $e^+e^- \to Z/\gamma \to$ hadrons ($\sim$70% of Z decays) is shown in Figure 1.2. At the Z pole, the Z-exchange term is $\sim$800 times the γ-exchange one, and the contribution from γ/Z interference is exactly zero. In what follows $\mathcal{M}_\gamma$ will be neglected, and only $\mathcal{M}_Z$ will be considered.

Figure 1.2: The $e^+e^- \to$ hadrons cross section.

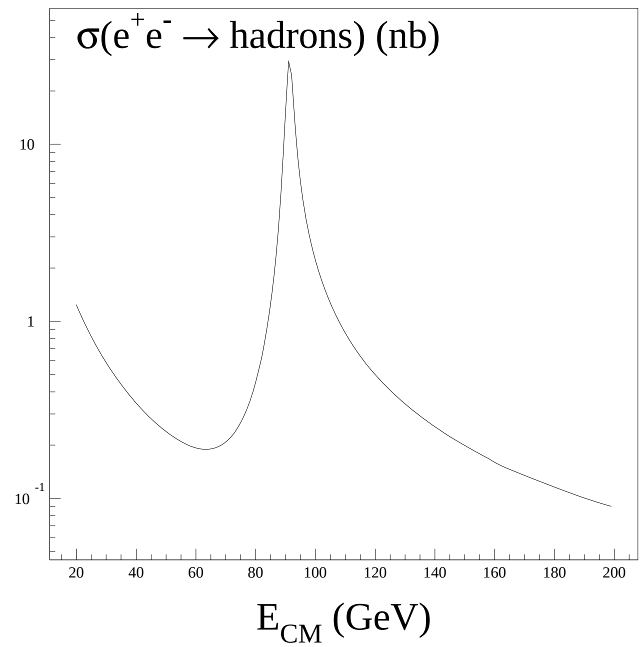

1.3 Electroweak Asymmetries

A number of observable quantities can be constructed to isolate the coupling asymmetry parameters A_f in the cross section shown in Equation 1.20. These are usually constructed as asymmetries themselves to avoid dependence upon absolute luminosity measurements. There are two signs which can be manipulated, that of the beam polarization P_e and that of $\cos\theta_f$. Using these it is possible to construct observable asymmetries which depend only upon either the initial-state coupling asymmetry A_e or the final-state coupling asymmetry A_f.

1.3.1 Left-Right Asymmetry A_{LR}

The left-right asymmetry, formed using the sign of the beam polaraization P_e, is defined as:

$$A_{LR} = \frac{\sigma_L - \sigma_R}{\sigma_L + \sigma_R} = |P_e| A_e \tag{1.23}$$

where σ_L and σ_R are the cross sections for Z production using a left- or right-handed electron beam, integrated over the detector acceptance. This asymmetry is the simplest way to measure A_e at the Z-pole, as no final-state fermion identification or angular distribution fitting are required. The exception is that final-state electrons must be rejected due to their additional t-channel scattering contribution, and in practice only hadronic decays of the Z are used. The SLD measurement of A_{LR} provides the most precise determination of $\sin^2\theta_W$ currently available.

1.3.2 Forward-Backward Asymmetry A_{FB}^f

The forward-backward asymmetry, formed using the sign of $\cos\theta_f$, the polar angle of the outgoing fermion w.r.t. the electron beam direction, is defined as:

$$A_{FB}^f(|z|) = \frac{\sigma(z>0)-\sigma(z<0)}{\sigma(z>0)+\sigma(z<0)} = 2\frac{A_e - P_e}{1-A_eP_e}A_f\frac{|z|}{1+z^2} \tag{1.24}$$

where $z = \cos\theta_f$. Unlike A_{LR}, this asymmetry can be formed for an unpolarized beam, although a polarized beam allows for the production of much larger asymmetries as shown in Figure 1.3. For the $P_e = 0$ case, A_{FB}^f is proportional to A_eA_f, so the initial- and final-state asymmetries cannot be individually extracted. If a lepton $\ell = e, \mu, \tau$ final state is selected and lepton universality is assumed, A_{FB}^f will be proportional to A_ℓ^2. This allows a direct determination of $\sin^2\theta_W$, although the statistics will be limited due to the small raw asymmetry. If the Standard Model values for the quark coupling asymmetries are assumed, the forward-backward asymmetry can be interpreted as a measurement of A_e. In the case of down-type quarks where $A_f \sim 1$, the raw asymmetry is only slightly diluted and high-statistics measurements are possible. The measurements of A_{FB}^b from LEP can be used to derive a value of $\sin^2\theta_W$ which is nearly as precise as that provided by A_{LR}.

Figure 1.3: Normalized fermion production cross sections for polarized and unpolarized beams.

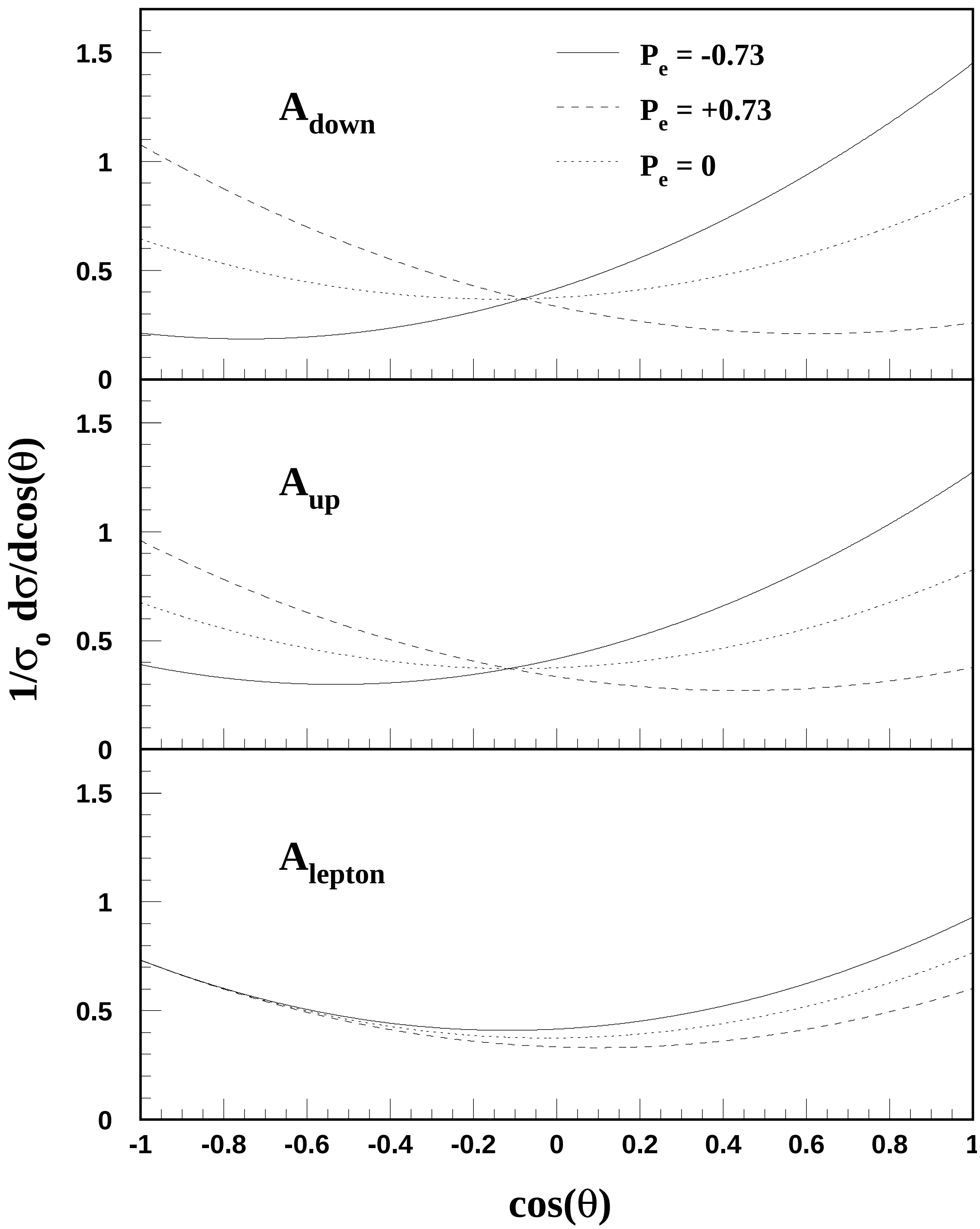

1.3.3 Left-Right-Forward-Backward Asymmetry $\tilde{A}^f_{FB}$

The left-right-forward-backward asymmetry is a double asymmetry formed using both the beam polarization sign and the sign of $\cos\theta_f$. This asymmetry is defined as:

$$\begin{aligned}\tilde{A}^f_{FB}(|z|) &= \frac{[\sigma_L(z>0)-\sigma_R(z>0)]-[\sigma_L(z<0)-\sigma_R(z<0)]}{[\sigma_L(z>0)+\sigma_R(z>0)]+[\sigma_L(z<0)+\sigma_R(z<0)]} \\ &= 2|P_e|A_f\frac{|z|}{1+z^2} \qquad (1.25)\end{aligned}$$

where $L(R)$ refer to left(right)-handed electron beams and $z = \cos\theta_f$. In contrast to A^f_{FB}, this asymmetry allows a measurement of A_f independent of A_e. At SLD this asymmetry has been used with lepton final states to make direct measurements of A_μ and A_τ, which are useful both as determinations of $\sin^2\theta_W$ and as tests of lepton universality. This observable has also been used to make measurements of A_s, A_c, and A_b which provide direct tests of the flavor structure of the Standard Model in the quark sector.

1.3.4 Radiative Corrections

The cross section given in Equation 1.20 was calculated only for the tree-level Z exchange process. However, there are several higher-order processes that also contribute to e^+e^- annihilation, which must be taken into account in measurements of A_e and A_f. They include propagator corrections, vertex corrections, and initial- and final-state radiation.

The propagator corrections are related to vacuum polarization effects. The two processes of most interest are shown in Figure 1.4. The effect of these processes is to modify the observed value of $\sin^2\theta_W$. This observable or "effective" value, denoted by $\sin^2\theta_{eff}$, is dependent upon the top quark mass as ($\propto \frac{m_t^2}{m_Z^2}$) and the Higgs mass as ($\propto \log\frac{m_H^2}{m_Z^2}$). Precise determinations of $\sin^2\theta_{eff}$ and m_t can be used to indirectly constrain the mass of the Standard Model Higgs boson, as will be discussed in Chapter 6.

Figure 1.4: Propagator corrections to $e^+e^- \to Z \to f\bar{f}$.

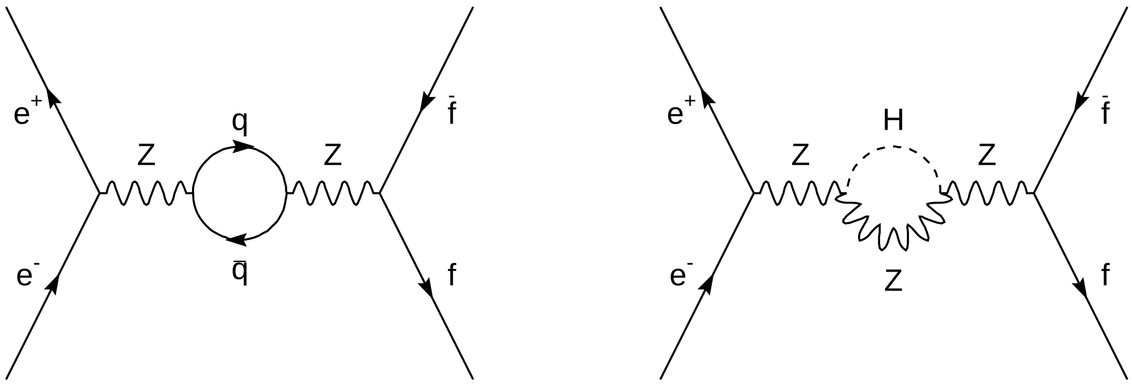

Figure 1.5: Vertex corrections to $e^+e^- \to Z \to b\bar{b}$.

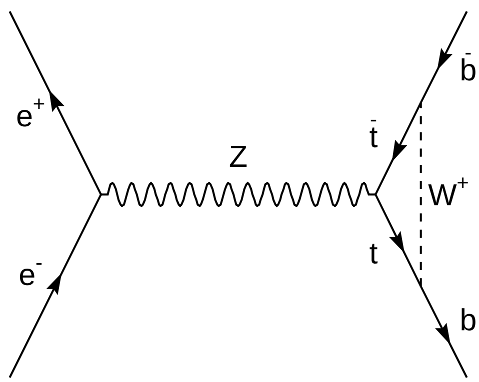

The most important of the vertex correction processes is shown in Figure 1.5. Because the correction scales as m_t^2 it is only significant for the $Zb\bar{b}$ vertex. The change in Γ_b caused by this process makes R_b sensitive to the value of m_t. The asymmetries A_{FB}^b and $\tilde{A}_{FB}^b$ are not sensitive to these corrections, because the increased width will cancel in the ratio of cross sections.

The first-order initial- and final-state radiation processes are shown in Figure 1.6. In the inital state, only photon radiation is possible. This lowers the average center-of-momentum energy of the colliding beams by ~20 MeV, and also broadens its width. These changes in the energy scale affect the value of $\sin^2\theta_{eff}$ which will be observed as discussed above.

Figure 1.6: Lowest order initial- and final-state radiation diagrams.

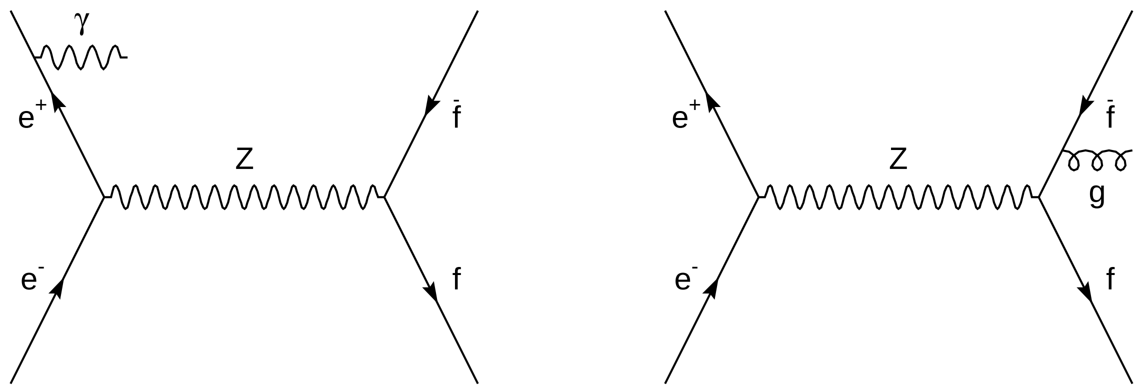

In addition, since the annihilation will not occur exactly at the Z-pole, the effects of γ/Z interference in the propagator will not vanish. Because they depend upon the experimental conditions, initial-state radiation effects are always removed from electroweak asymmetry measurements before the results are quoted.

Final-state radiation can either be photons, or in the case of quark decays of the Z, gluons. Because this process occurs after the decay of the Z, it does not affect the energy scale. The radiation increases the phase space for the Z decay, increasing its width. This will change R_b but not the asymmetries in the same way as the vertex corrections. There is another effect, however, which applies to A^f_{FB} and $\tilde{A}^f_{FB}$. Because these asymmetries are functions of the outgoing fermion polar angle, the distortion of the angular spectrum from final-state radiation will change the observed asymmetry. For photon radiation the effect is negligible, but gluon radiation produces a significant change in A^f_{FB} and $\tilde{A}^f_{FB}$ (the correction is the same for both). Because it is universal for R_b no correction is generally made, and the reported results include the effects of QCD radiation. The asymmetry measurements, however, will generally have different sensitivity to QCD radiation due to differences in experimental technique. The convention is to remove these effects before reporting results.

One last higher-order process of interest is shown in Figure 1.7. These fermion loop

Figure 1.7: Radiative correction to the Higgs propagator.

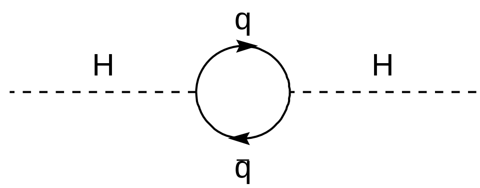

corrections to the Higgs propagator cause the Higgs mass to diverge quadratically if the Standard Model is assumed valid up to the Planck scale $M_{Pl} \sim 10^{18}$ GeV/c^2, where the effect of gravity becomes comparable to the other forces. These corrections can be canceled by fine-tuning parameters of the theory, but this unstable hierarchy between the weak scale and the Planck scale is generally thought to indicate that the Standard Model is not a complete theory. One solution is to cancel the divergent terms by incorporating a new symmetry, in which each fermion has a bosonic partner. Since the bosonic loop corrections to the Higgs propagator enter with the opposite sign, the divergent terms can be made to cancel order-by-order without any fine-tuning. Because the Higgs is part of a symmetry group it is massless at tree level in such a theory, with its mass generated by the breaking of the symmetry. The Higgs mass is therefore protected against divergences above the symmetry-breaking scale, in the same way that the photon and Z masses are protected in the Standard Model. This "supersymmetric" extension to the Standard Model is the most popular solution to the so-called "hierarchy problem", although at the moment no evidence has been found for any of the superpartner particles.

This Thesis will present an analysis of the $e^+e^- \to Z \to Q\bar{Q}$ process, with $Q\bar{Q} = c\bar{c}$ and $b\bar{b}$. The coupling asymmetry parameters A_c and A_b will be determined from measurements of the left-right-forward-backward asymmetries $\tilde{A}^c_{FB}$ and $\tilde{A}^b_{FB}$. The results obtained will then be combined with other precise electroweak measurements to study the $Zc\bar{c}$ and $Zb\bar{b}$ vertices. Finally, the consistency of the Standard Model with these and other measurements and the constraints which can be placed on the Higgs mass m_H will be discussed.

Chapter 2

Experimental Apparatus

The measurements presented in this thesis were made using the SLAC Large Detector at the SLAC Linear Collider. This facility produces electron-positron annihilations at a center-of-mass energy of 91.26 GeV, the peak of the Z resonance. The SLD detector surrounds the collision point of the two beams, and observes the decays of the produced Z bosons. This chapter presents a brief discussion of the elements of this experimental program.

2.1 SLAC Linear Collider

The SLAC Linear Collider (SLC) [22] is an electron-positron colliding-beams machine located at the Stanford Linear Accelerator Center (SLAC). The SLC consists of a polarized electron source, a two-mile-long linear accelerator (linac) which is used to accelerate both electrons and positrons, and two arcs which transport the electron and positron bunches into the collision region. A schematic view of the SLC is shown in Figure 2.1.

The SLC operates on a 120 Hz cycle. Two longitudinally polarized electron bunches are produced at the source, accelerated to 1.19 GeV, and diverted into the north damping ring. This energy was chosen such that the total field seen by the bunchs in traversing the bending

Figure 2.1: Schematic view of the SLAC linear collider. The arrows indicate the direction of the electron spin at each point.

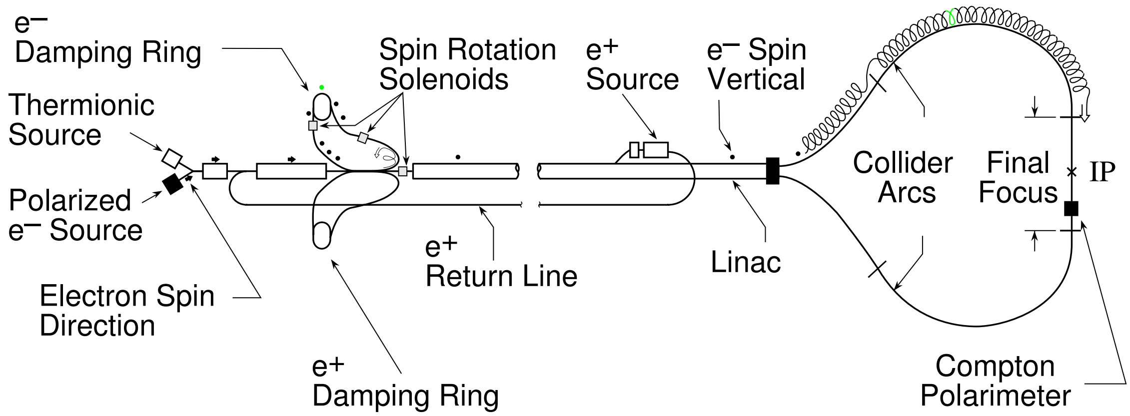

magnets will precess the electron spins so that they are transverse to the beam direction in the horizontal plane. A spin rotation solenoid then rotates the polarization into the vertical direction, where it can survive in the damping ring. The electron bunches are stored for one machine cycle (8.3 ms). One positron bunch from the return line is also accelerated to 1.19 GeV and stored in the south damping ring. The positrons require two cycles of cooling (16.7 ms). After the electron bunches have been damped, the second positron bunch stored in the damping ring during the previous cycle is extracted and inserted into the linac. Followed by the two damped electron bunches, it is accelerated to 46.7 GeV. The spin rotation solenoids on the damping ring return line and at the beginning of the linac shown in Figure 2.1 can be used at this point to manipulate the electron spin into any direction. For standard SLD operations, however, these solenoids were not used and the electron polarization was left in the vertical direction during acceleration. The positron bunch is sent into the south arc and the first electron bunch into the north arc by a dipole magnet in the beam switchyard at the end of the linac. The bunches lose around 1.1 GeV of energy through synchrotron radiation as they traverse the 1 km arcs to the interaction point (IP). The arcs of the machine do not line in a plane, but rather follow the vertical rise and fall of the terrain. The beams must therefore be bent both horizontally and vertically as they traverse the arcs. The north arc bends are equivalent to 26 rotations of the electron spin vector, and by a combination of the horizontal bending and the vertical perturbations in the orbit ("spin bumps" [23]) the electron spin is brought around to longitudinal at the IP.

The second electron bunch is accelerated to 30 GeV and directed onto a tungsten target. Positrons filtered from the ensuing electromagnetic shower are accelerated into the return line back to the front of the linac to be used in the next machine cycle.

As the electron and positron bunches enter the final focus, a series of superconducting quadrupole magnets are used to focus them down to a $1.5 \times 0.8 \times 700\mu$m (horizontal, vertical, longitudinal) luminous region at the IP. This focusing is critical to reaching high Z boson production rates. The luminosity history of the SLC is shown in Figure 2.2. The dramatic improvement seen in the 1997-98 run was due to improvements in the final focus optics. The results presented in this Thesis use only the data taken in 1996-98, a sample of $\sim$400,000 Z decays.

2.1.1 Polarized Source

The electron bunches used for SLC collisions are produced using the SLC polarized source, shown in Figure 2.3. Light from a Nd:YAG-pumped Ti:sapphire laser is passed through a circular polarizer and brought onto a GaAs photocathode. The light excites electrons from the valence to the conduction band. The surface of the photocathode is treated with cesium and NF_3 to attain a negative electron affinity surface, allowing the excited electrons to escape the photocathode with a quantum efficiency of about 0.1%.

The energy level diagram of GaAs for the states of interest is shown in Figure 2.4. The upper diagram is for bulk GaAs, the type of photocathode used in the 1992 SLC running. The laser wavelength is tuned to 850-860 nm to match the 1.52 eV bandgap energy. A problem

Figure 2.2: History of the SLD recorded luminosity.

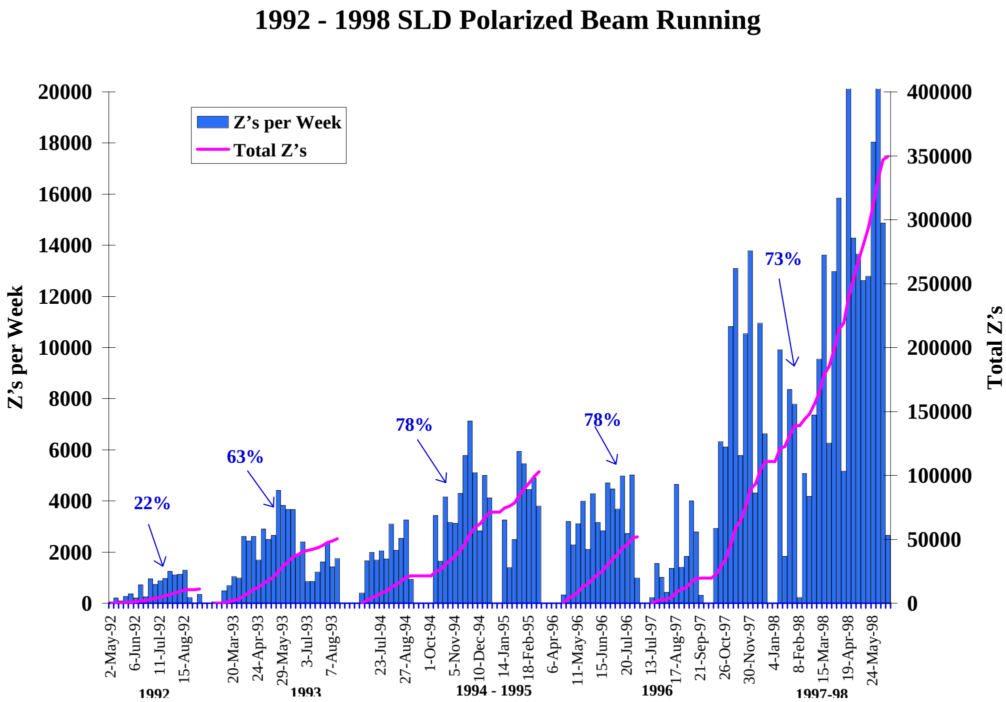

with this type of photocathode is the degeneracy between the $m_j = 3/2$ and $m_j = 1/2$ states in the valence band. A right-polarized photon can excite either the $m_j = -3/2 \rightarrow -1/2$ transition, with relative strength 3, or the $m_j = -1/2 \rightarrow +1/2$ transition with relative strength 1. Therefore the maximum polarization achievable with such a photocathode is 50%.

The lower diagram in Figure 2.4 shows the energy levels for a layer of GaAs grown upon a substrate of GaAsP. The small difference in the lattice spacing between the two materials is of sufficient magnitude to generate a mechanical strain on the surface large enough to break the degeneracy between the $m_j = 3/2$ and $m_j = 1/2$ states in the valence band. The laser light can now selectively pump only the $m_j = 3/2 \rightarrow 1/2$ transitions, for a theoretical maximum polarization of 100%.

The history of SLC electron beam polarization is shown in Figure 2.5. In 1992 a bulk

Figure 2.3: The SLC polarized source.

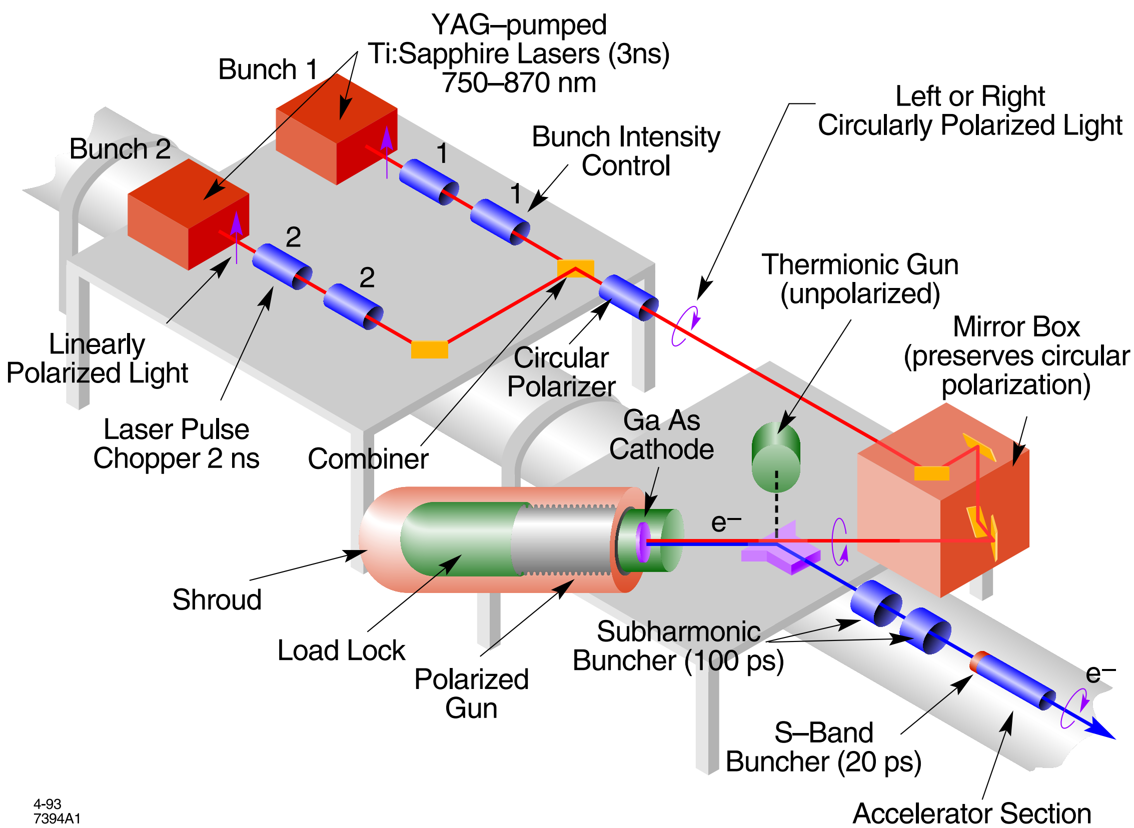

Figure 2.4: Energy-level diagram for (top) bulk GaAs and (bottom) strained GaAs.

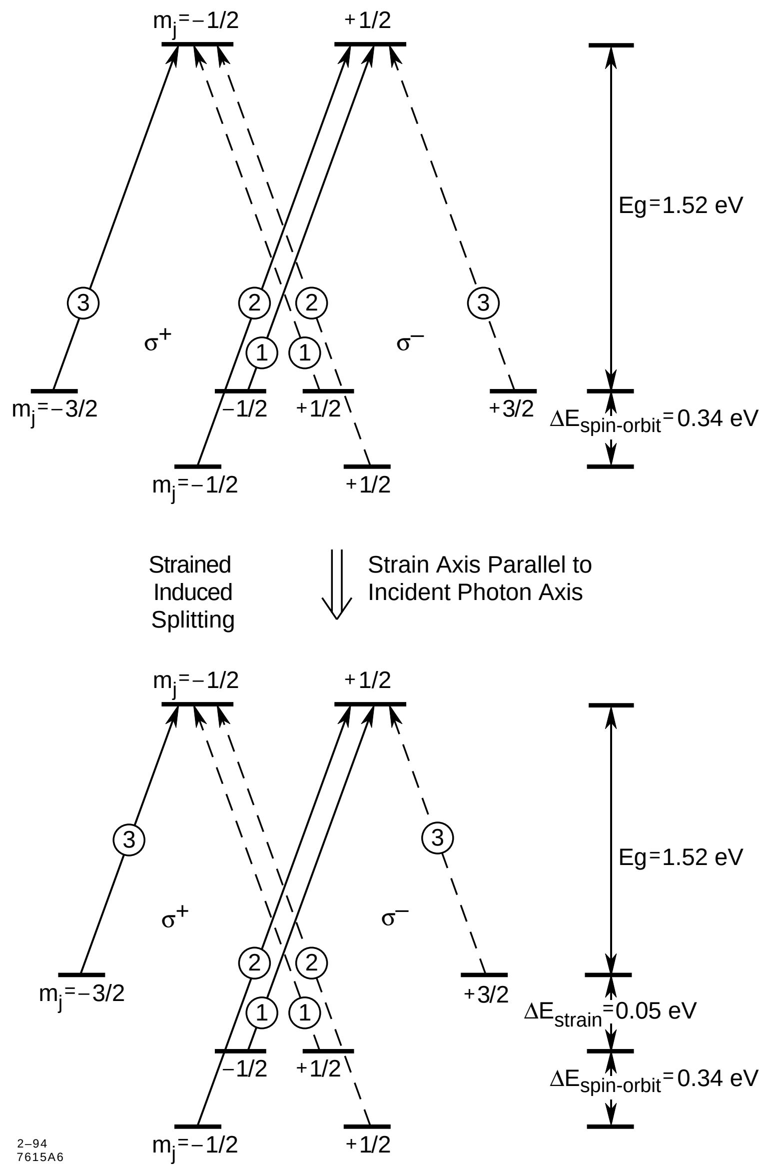

Figure 2.5: History of the SLC electron beam polarization.

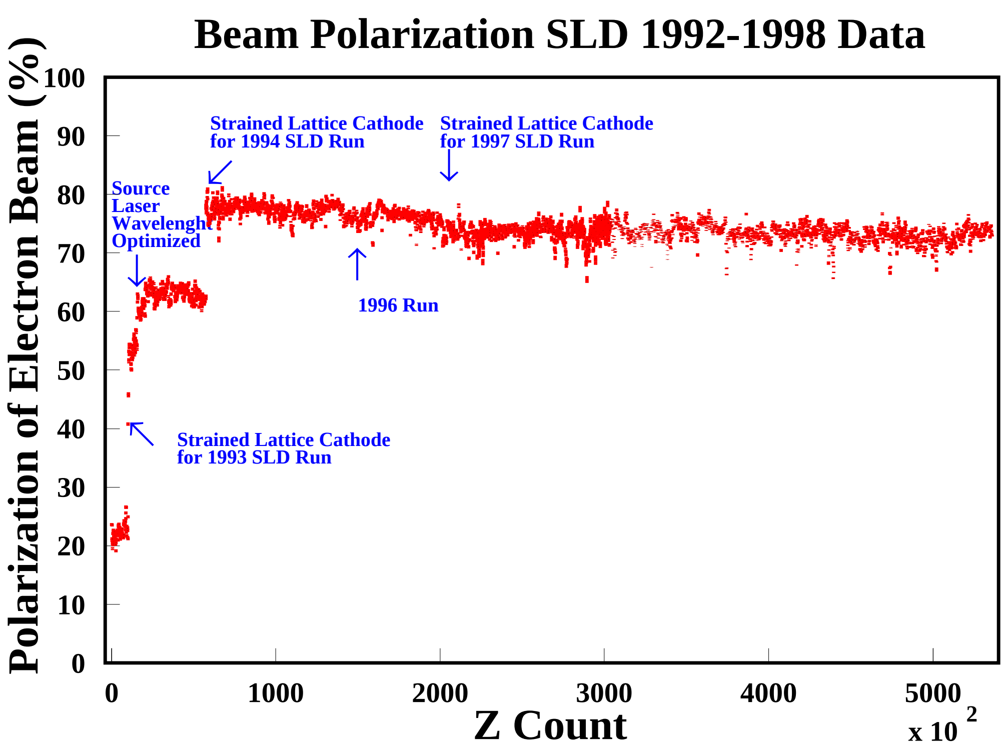

GaAs photocathode was used to attain a polarization of 22%. In 1993 a strained photocathode with a GaAs layer of 300 nm was installed, increasing the SLC polarization to 63%. A photocathode with a thinner layer of 100 nm was introduced for the 1994-95 run, reaching a polarization of 77%. This style of photocathode was used in the 1996 and 1997-98 runs as well, with average polarizations of 76% and 73% respectively.

2.1.2 Compton Polarimeter

The polarization of the SLC electron beam is measured using Compton scattering. The SLC polarimetry system is shown in Figure 2.6. Circularly polarized 2.33 eV photons from a frequency-doubled YAG laser are collided with the electron beam at a point 33 m downstream from the SLC interaction point. The helicity of the laser is chosen pseudorandomly pulse-by-pulse to avoid any SLC periodicities. The backscattered electrons are separated from the main beam by a precisely measured dipole bend magnet and directed upon a Cherenkov detector. This detector uses a array of propane radiators coupled to PMT readouts to measure the energy spectrum of the scattered electrons in the range 17 to 30 GeV. Each channel of the detector is related to a range of electron energies through its distance from the beam line and the spectrometer optics. The position of the kinematic endpoint at 17.36 GeV was found by frequent horizontal scanning of the detector position. This point was used to calibrate the position-energy relation, which was the main source of systematic error for the polarization measurement.

For each Cherenkov channel j an asymmetry A_j^{meas} is formed of the signal observed with the electron and photon polarizations parallel and antiparallel.

$$A_j^{meas} = \frac{\sigma_j(J_z = 3/2) - \sigma_j(J_z = 1/2)}{\sigma_j(J_z = 3/2) + \sigma_j(J_z = 1/2)} = |P_e||P_\gamma|a_j \tag{2.1}$$

The analyzing power a_j is the cross section weighted Compton scattering asymmetry

Figure 2.6: The SLC Compton polarimeter.

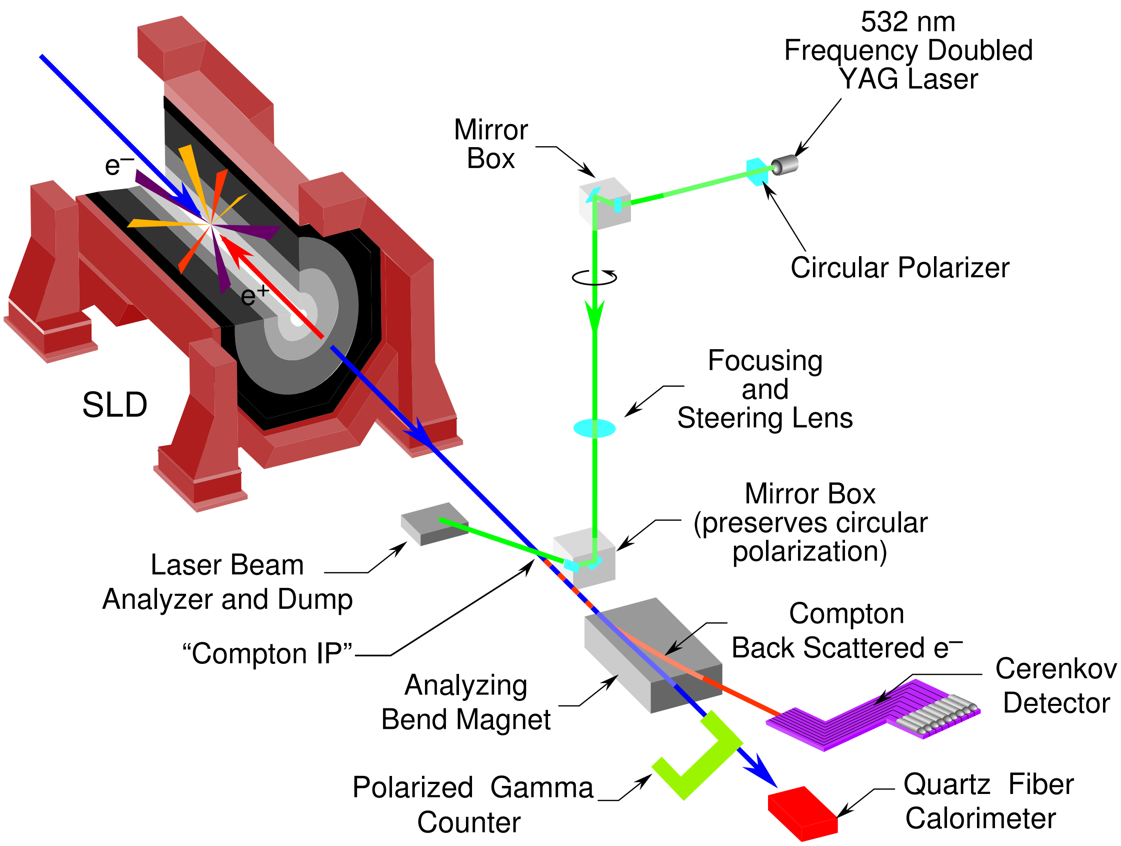

calculable in QED, convoluted with the detector response function for each detector channel. These differed from the theoretical Compton asymmetry evaluated at the mean energy accepted by that channel by typically $\sim 1\%$. The P_e and P_γ factors are the longitudinal components of the electron and photon polarizations. With a known P_γ a measurement of P_e can be extracted from the raw asymmetry observed in each channel.

Two other detectors were also used, the polarized gamma counter (PGC) and the quartz fiber calorimeter (QFC). They work by observing the scattered photons rather than the electrons, as shown in Figure 2.6. Because of bremstrahlung backgrounds these detectors could only be operated when the beams were not in collision, but they provide useful consistency checks of the Cherenkov analyzing power calibration.

The default polarization values are taken from the Cherenkov channel nearest the kinematic edge, which has the highest Compton asymmetry. The adjacent channel and the two photon detectors are used to set a relative 0.4% systematic error due to analyzing power determination. Other uncertainties related to electronics noise and linearity increase the relative systematic uncertainty to 0.5% for the 1996-98 data.

Polarization data were taken continuously during SLC running, and luminosity-weighted average polarizations $\langle P_e \rangle$ for each of the run periods were calculated. A variety of small corrections for beam energy spread and polarization transport effects were also applied. For the 1996 run $\langle P_e \rangle = 76.16 \pm 0.40\%$ and for the 1997-98 run $\langle P_e \rangle = 72.92 \pm 0.38\%$ [24].

To verify that the positron beam was unpolarized, a separate test was performed [25]. The SLC positron beam was transported to End Station A, where a Møller polarimeter [26] which had been constructed for fixed-target DIS experiments was used to measure its polarization. The result of $P_{e^+} = -0.02 \pm 0.07\%$ was consistent with zero as expected.

Figure 2.7: Schematic view of the SLC energy spectrometer.

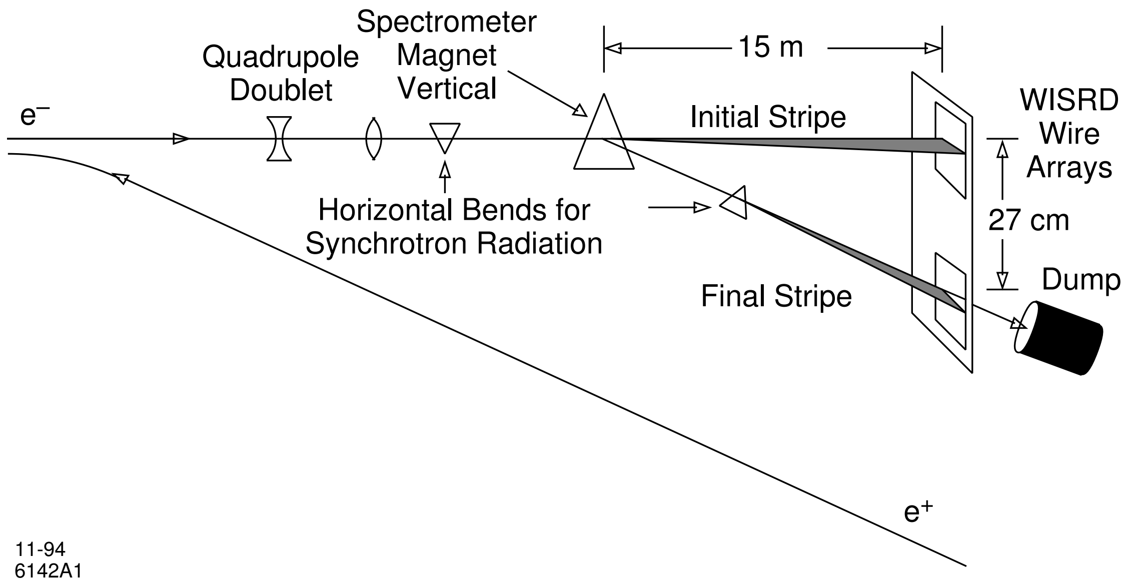

2.1.3 Energy Spectrometer

The energies of the electron and positron beams are measured pulse-by-pulse using spectrometers downstream of the IP. The layout of a spectrometer is shown in Figure 2.7. Each spectrometer consists of a horizontal bend, a precisely calibrated vertical bending magnet, followed by a second horizontal bend. The bursts of synchrotron radiation produced by the horizontal bends are measured using wire chambers. The distance between the stripes gives the vertical bending angle, and therefore the beam energy. During the 1997-98 SLD run a scan of the Z peak was performed to verify the calibration of the spectrometers. The resulting luminosity-weighted average center-of-momentum collision energy for the 1997-98 run was 91.237±0.029 GeV.

2.2 SLC Large Detector

The SLC Large Detector (SLD) [27], situated around the SLC interaction point, provides the means to study the decays of the produced Z bosons. Isometric and sectional views of the SLD are shown in Figure 2.8 and Figure 2.9. The SLD consists of a barrel section and two endcaps, to achieve $\sim 98\%$ of 4π-steradian solid-angle coverage. These sections are built up of layers, with each layer a detector subsystem. The layer closest to the IP is the vertex detector (VXD), used for measuring the position of charged particle trajectories. Also at small radius is the luminosity monitor (LUM). Outside of these is the drift chamber, in barrel (CDC) and endcap (EDC) sections. These provide measurements of both the position and momentum of charged particles. The next layer is a Cherenkov ring-imaging detector (CRID), which is used for particle identification. The liquid-argon calorimeter (LAC) provides energy measurements for charged and also for neutral particles. The magnet coil is a superconducting solenoid that produces the uniform 0.6 T field used for momentum measurements. The final layer is the warm iron calorimeter (WIC), which is used for muon identification and also provides the magnetic flux return. Each of these subsections will be described in more detail later in this chapter.

The SLD coordinate system is defined so that the z-axis points north, along the positron beam direction. The x-axis then points west and the y-axis upwards to maintain a right-handed system.

2.2.1 Luminosity Monitor

The luminosity of the SLC is measured using the luminosity monitor, shown in Figure 2.10. This is done by monitoring the rate of small-angle Bhabha scattering, which can be precisely calculated in QED. The LUM consists of a pair of highly-segmented tungsten-silicon calorimeters. The luminosity monitor/small-angle trigger (LMSAT) covers the polar-angle

Figure 2.8: Isometric view of the SLD detector.

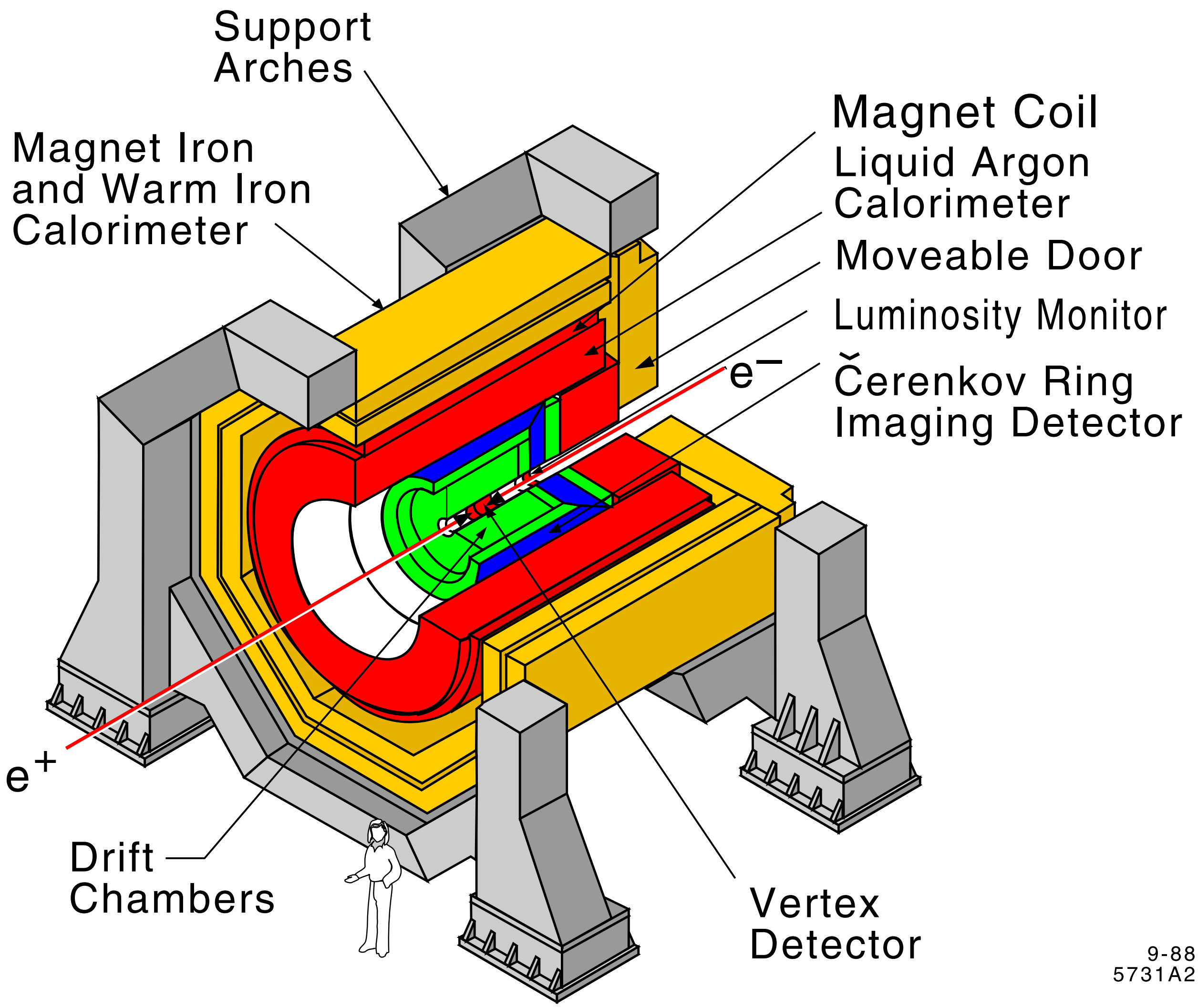

Figure 2.9: Sectional view of one quadrant of the SLD detector.

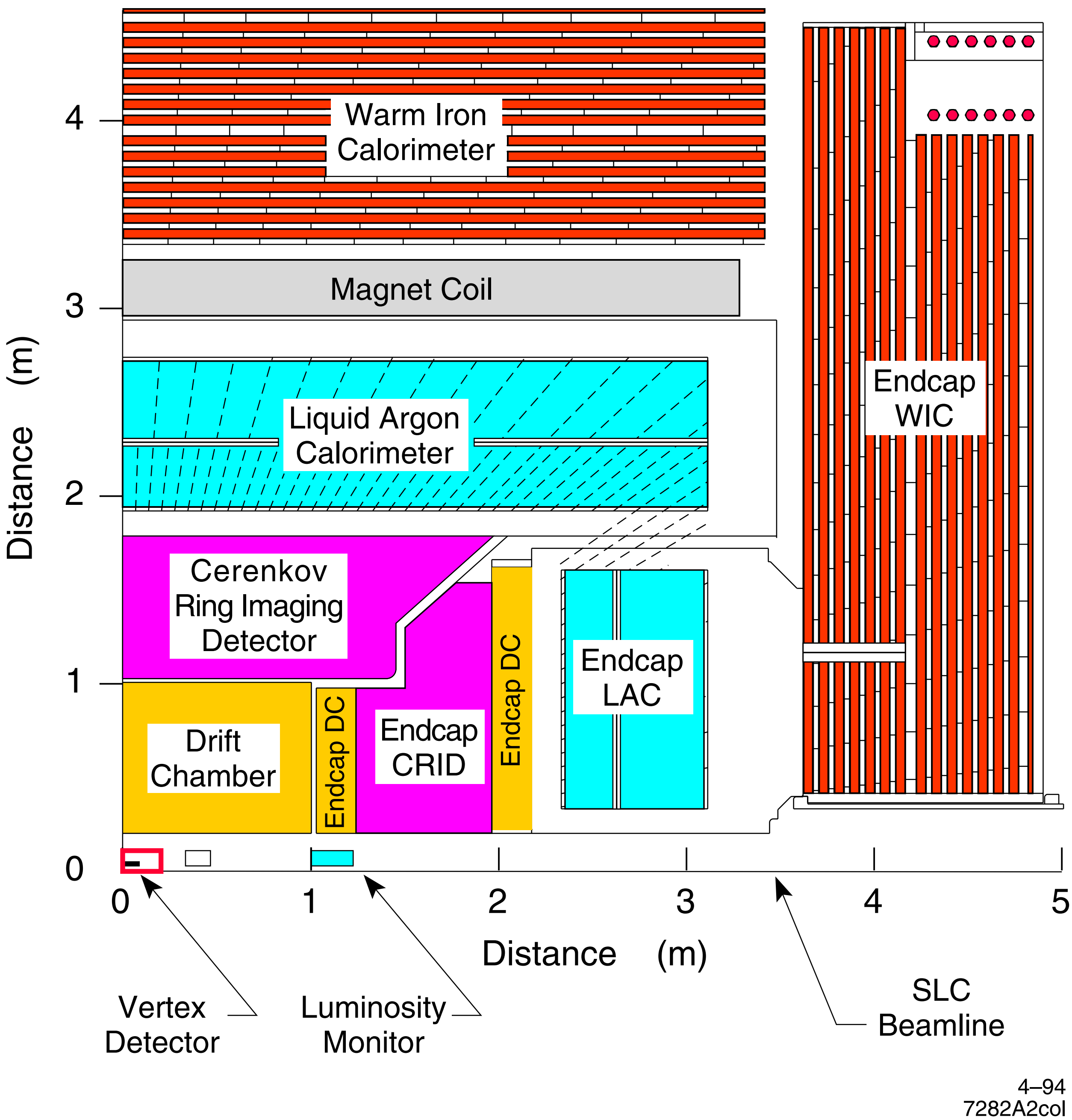

Figure 2.10: The SLD luminosity monitor.

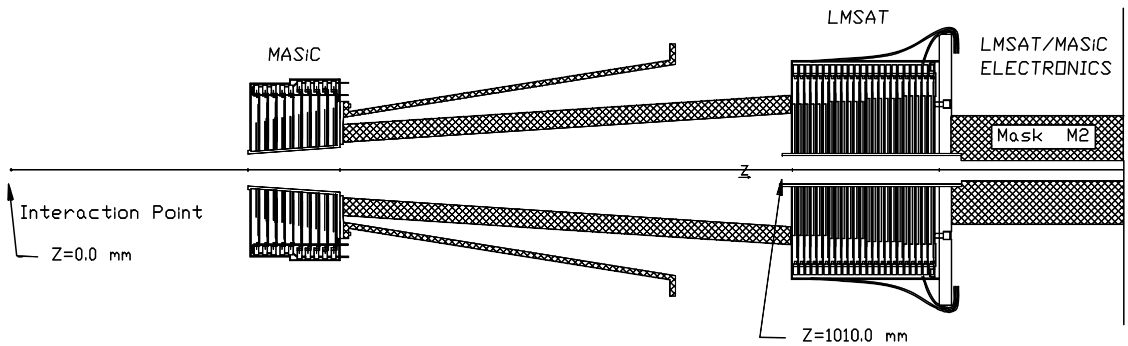

range from 28 to 68 mrad, and the medium-angle silicon calorimeter extends from 68 to 200 mrad. Because the asymmetry measurements presented in this thesis don't depend on absolute luminosity, the LUM results are not used.

2.2.2 Vertex Detector

The positions of charged particle trajectories are measured using the SLD vertex detector (VXD). The SLD has had two vertex detectors, both of them based upon charge coupled device (CCD) technology. The original detector, VXD2, was installed for the data collected in 1992-95. Because these results only use the data collected from 1996-98 it will not be described here. In 1996 an improved vertex detector VXD3 [28] was installed, to take advantage of improvements in CCD technology that permit custom fabrication of much larger active area devices.

VXD3 uses CCDs with active area measuring 80×16 mm^2. Each individual pixel is $20 \times 20 \mu$m^2, for a total of 4000×800 pixels. Two CCDs are mounted on a beryllium substrate to form a ladder, as shown in Figure 2.11. The two CCDs overlap by $\sim$1 mm to allow their relative alignment using charged tracks. These ladders were mounted onto a series of three concentric beryllium annuli in a shingled arrangement, so that complete azimuthal coverage was attained, with $\sim 500\mu$m overlap between adjacent ladders for alignment purposes. Views

Figure 2.11: Two-CCD VXD ladder.

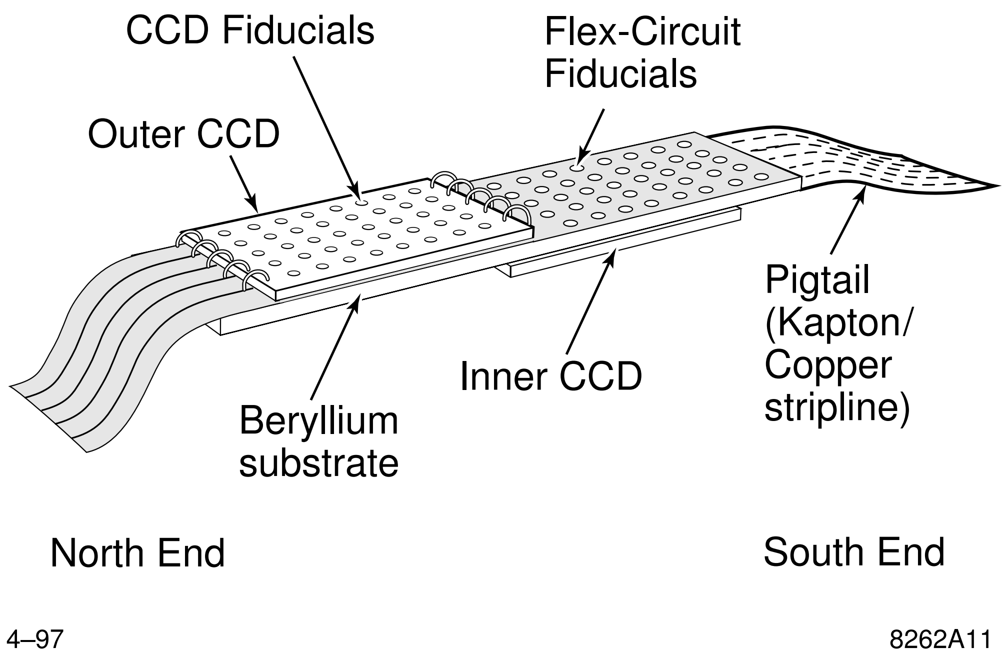

of the VXD3 ladder layout transverse and parallel to the beamline are shown in Figure 2.12 and Figure 2.13. The beampipe radius of 23.2 mm was set based on accelerator-related backgrounds, which fixes the layer one mean radius at 28 mm. The layer three mean radius of 48.3 mm was determined by requiring three-layer acceptance for tracks with $|\cos\theta| \leq 0.85$, to match the effective acceptance of the central drift chamber. The layer two mean radius of 38.2 mm provides acceptable lever arm for tracks with a missing hit on layer one or three, and provides a third space point for enhanced pattern recognition at high $|\cos\theta|$ and for self-tracking purposes. A total of 48 ladders are used, for a net pixel count of 307 million. Each layer contributes a radiation thickness of only $0.4\%X_0$, which is important for reducing the tracking errors caused by multiple scattering.

The bias voltage applied to the CCDs was $\sim$10 V, producing a depletion zone of around 20 μm thickness. A minimum-ionizing particle produces about 1200 electron/hole pairs. The charge which is collected in each pixel is read out in a doubly-serial manner. Each CCD is

Figure 2.12: Schematic layout of VXD3 in the $r\phi$ view.

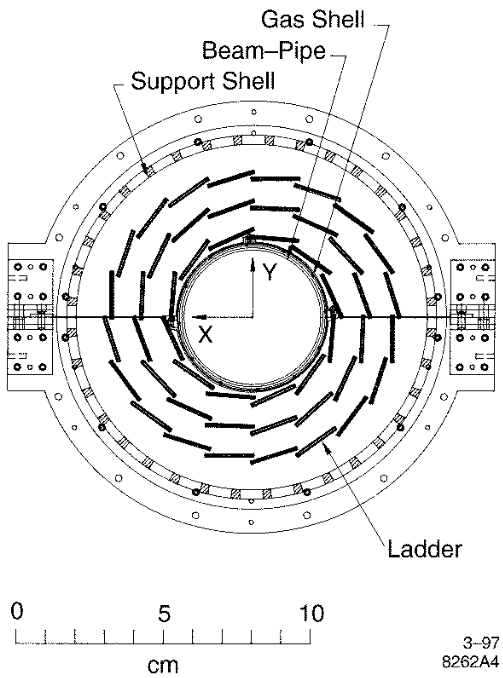

Figure 2.13: Schematic layout of VXD3 in the rz view.

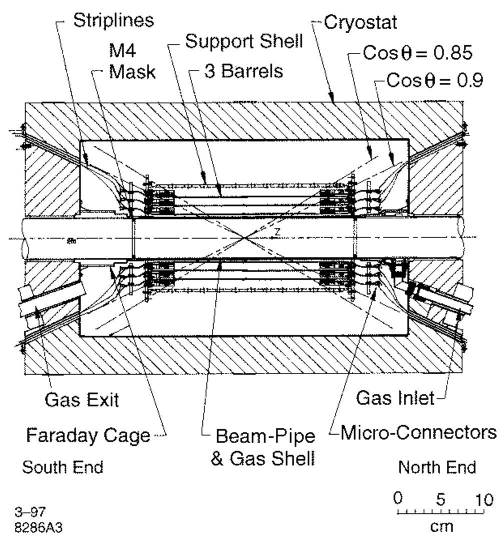

divided into four quadrants, with one output amplifier for each located at the four corners of the CCD. One clock (the I clock) causes rows of pixel charges to shift towards the two shorter sides of the CCD, where the readout registers are located. Once a row has been loaded into the readout register, the R clock successively moves each pixel charge in the register into the output amplifier. To read out the entire dectector takes 0.2 seconds or about 26 beam crossings at 120 Hz. Because the pixel occupancy is $< 10^{-4}$ rejecting the background pileup hits is not difficult.

The full assembly is mounted in a nitrogen gas cryostat and maintained at a temperature of around 185 K. It is necessary to operate the detector at low temperatures to reduce lattice defects caused by radiation damage, which can cause trapping centers to develop in the silicon. Because CCDs are read out serially, a trapping center affects not just nearby pixels, but can impact the charge transfer out of all pixels behind it in that column.

Figure 2.14: Miss distance of tracks in $Z \to \mu^+\mu^-$ events, in the $r\phi$ (left) and rz (right) projections.

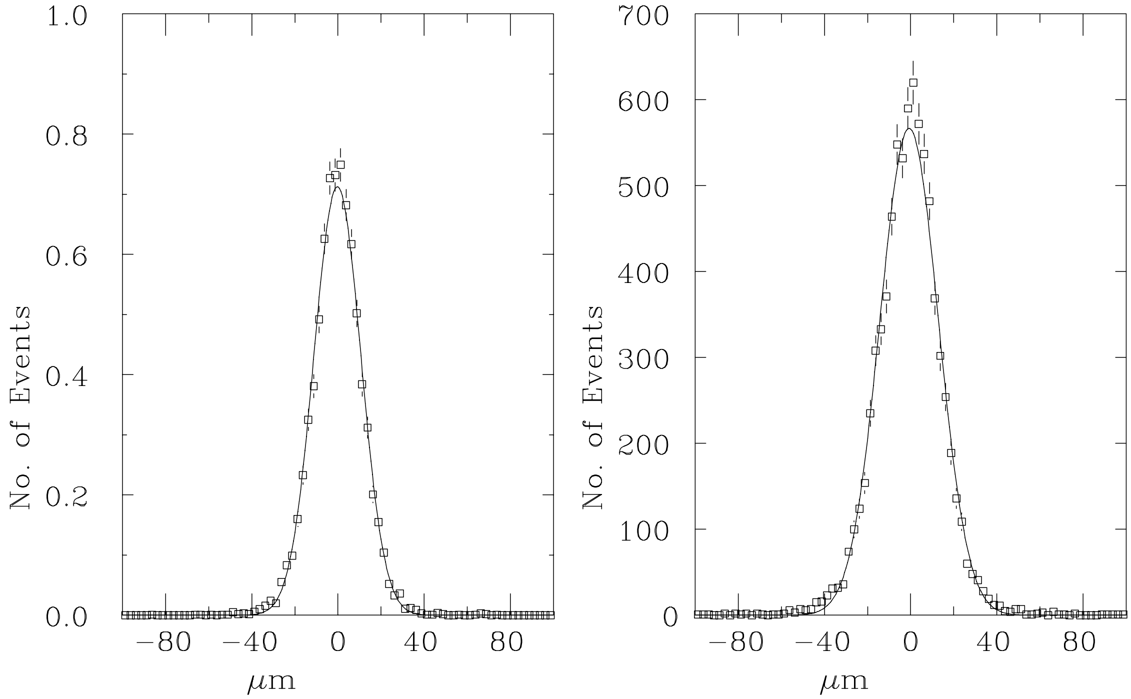

The detector is aligned internally using charged tracks which traverse the CCD overlap regions, and also tracks with a hit on all three layers. The positions and orientations of the individual CCDs are adjusted to minimized the residuals of the reconstructed to the expected hits. An optical survey to determine the shape of each CCD after mounting on its ladder and of the assembled ladder positions provided the starting point for this procedure. The residuals from the best-fit alignment indicate $< 4\mu$m single-hit resolution. The track position resolution at the IP can be estimated from the miss distance of the two tracks in $Z \to \mu^+\mu^-$ decays, shown in Figure 2.14. The widths indicate asymptotic resolutions of 7.7 μm in $r\phi$ μm and 9.6 μm in rz.

2.2.3 Drift Chamber

Just outside of VXD3 lie the drift chambers, used for measuring the positions and momenta of charged particles. The SLD drift chamber system consists of a barrel-shaped central drift chamber (CDC) and two endcap drift chamber (EDC) sections. Due to excessive backgrounds the EDC systems have not been successfully incorporated into the SLD track reconstruction procedure, so only the CDC will be discussed here.

The CDC [29] is a cylindrical drift chamber, which extends from 0.2 m to 1.0 m in radius and from -1.0 m to +1.0 m in z, as shown in Figure 2.9. The effective polar angle range for charged particle tracking is therefore $|\cos\theta| < 0.85$. The chamber is arranged in ten concentric superlayers, as shown in Figure 2.15. There are four axial layers, in which the wires run parallel to the z-axis, and three pairs of stereo layers, in which the wires run at angles of ± 41 mrad to the z-axis. Each superlayer is divided azimuthally into cells which measure about 6 cm in width and 5 cm in height. Each cell contains a vector of eight sense wires surrounded by a grid of field-shaping wires, embedded within a framework of field wires. The field wires, made of 150 μm gold-coated aluminum and held at an average voltage of -5300 V, produce a uniform drift field of 0.9 kV/cm. The field-shaping wires, also made of 150 μm gold-coated aluminum but held at a lower voltage of -3027 V, focus the electric field lines to produce a charge amplification of about 10^5 in the region near the sense wires. These sense wires, made of 25 μ gold-coated tungsten, are spaced at 5 mm intervals within the cell.

The volume of the CDC is filled with a gas mixture of 75% CO_2, 21% Ar, 4% isobutane, and 0.2% H_2O. The choice of CO_2 was driven by its low drift velocity, about 7.9 μm/ns for the CDC field configuration. Slower drift translates into better position resolution for a given drift time resolution, and allows easier separation of multiple hits on a single wire. The Ar is added to increase the gain, the isobutane acts as a quencher, and the water reduces the

Figure 2.15: Schematic layout of the CDC in the $r\phi$ view, showing the cell structure of the superlayers.

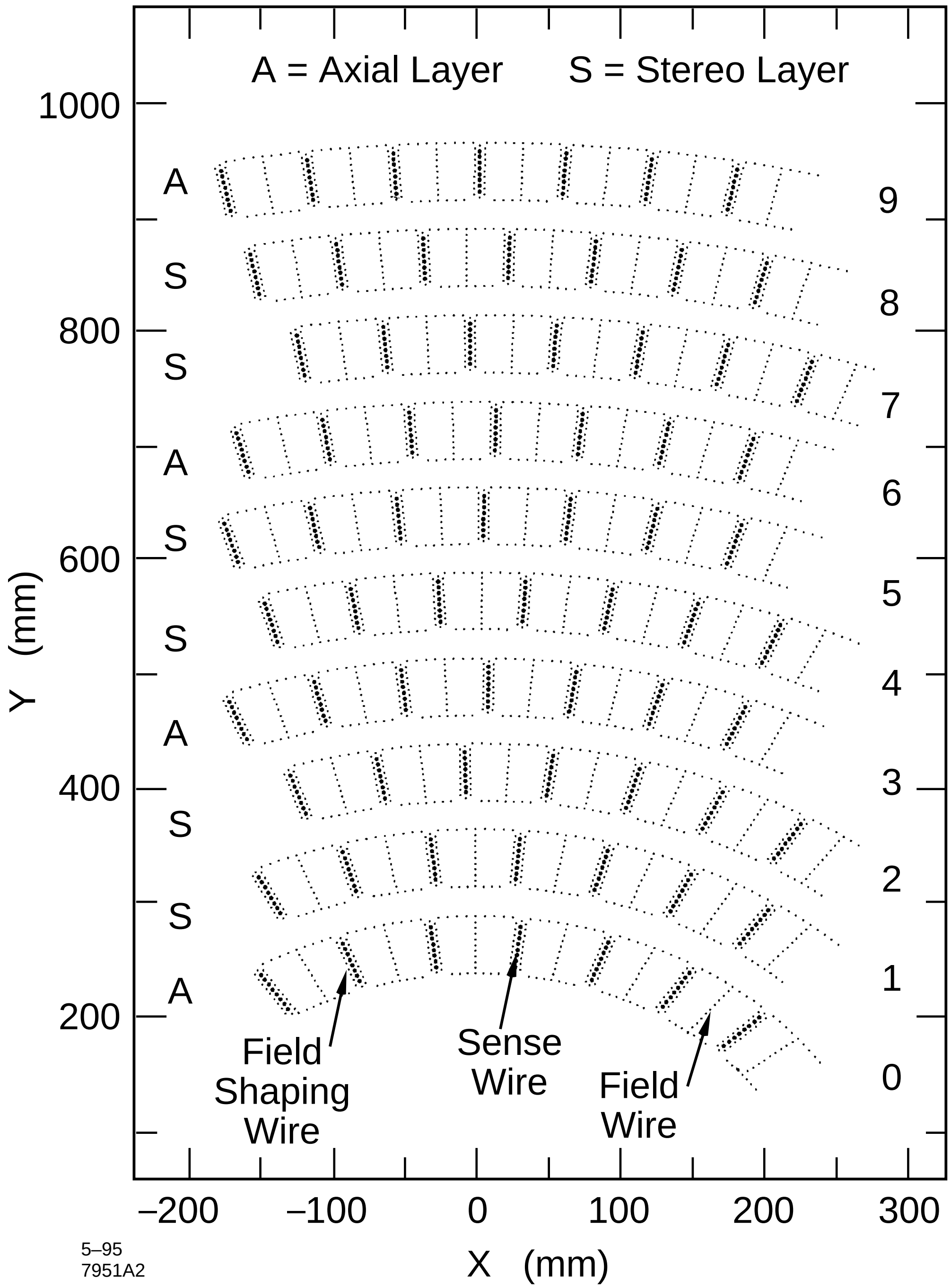

effects of wire aging. An average of 16 electrons per sense wire are produced by the passage of a minimum-ionizing particle through the CDC gas.

The waveforms of the pulses induced on the sense wires by the drifting electrons are digitized on both ends of the wire. The time of the leading edge of a pulse is used to estimate the distance of the particle trajectory from the wire in xy, using the known drift field configuration and correcting for the effects of the 0.6 T SLD magnetic field. The resolution attained for a single sense wire is $\sim$100 μm, although there are substaintial non-Gaussian tails. The position of the trajectory in z is obtained from the ratio of the pulse heights at the two ends of the wire, and is accurate to about 5 cm. Additional information in this view is provided by the stereo layers when the tracks are fitted.

The hits within each cell are combined into vectors, which are the basic elements of track finding. Vectors are also constructed in the VXD, where $\geq$3 hits line up. The algorithm starts by finding circular segments in xy consistent with at least two of the axial superlayer vectors. Adding the VXD and stereo vectors fixes the angle of the track candidate in rz. Once a candidate track has been identified, a detailed fit is performed using the Billoir algorithm [30] taking into account the effects of magnetic field variations and energy loss in the detector material. This fit is not restricted to the hits in the vectors used to identify the candidate and is free to drop or add VXD and CDC hits to obtain the best fit. The hits assigned to the track are removed and the algorithm is iterated until no more tracks are found. The momentum resolution for the fitted tracks is estimated to be $(\sigma_{p_\perp}/p_\perp^2)^2 = 0.0026^2 + (0.0095/p_\perp)^2$, where $p_\perp$ is the track momentum transverse to the beam axis measured in GeV/c. The first term comes from the track position measurement uncertainty and the second is the contribution from multiple scattering in the detector. For tracks with at least two VXD hits, the impact parameter resolutions in the $r\phi$ and rz views are given by:

$$\sigma_{r\phi}^2 = 7.7^2 + \left(\frac{33}{p\sin^{3/2}\theta}\right)^2 \mu\text{m} \tag{2.2}$$

$$\sigma_{r\phi}^2 = 9.6^2 + \left(\frac{33}{p\sin^{3/2}\theta}\right)^2 \mu\text{m} \quad (2.3)$$

where the first term is from the track position measurement uncertainty and the second term is the contribution from multiple scattering. Vectors of ≥3 VXD hits which are not associated with a CDC track are also retained, and can be used as tracks in certain situations as described in Chapter 4.

2.2.4 Cherenkov Ring-Imaging Detector

Cherenkov radiation is produced when a charged particle traverses a medium at a speed greater than the speed of light in that medium. The radiation is emitted at a characteristic angle to the particle trajectory. This Cherenkov angle is given by:

$$\cos\theta_C = \frac{1}{\beta n} \quad (2.4)$$

where $\beta = v/c$ is the normalized velocity of the particle and n is the index of refraction of the material. Measurement of θ_C therefore provides a measurement of the velocity of a particle, and if its momentum is also known its mass can be extracted. This allows the determination of the particle type.

Particle identification at the SLD using this technique is possible using the Cherenkov Ring-Imaging Detector (CRID) [31]. The CRID is composed of separate barrel and endcap sections, as shown in Figure 2.9. Because of the lack of charged particle tracking in that region the endcap CRID sections were not operated, and only the barrel CRID, covering the region $|\cos\theta| < 0.68$, will be described here.

In order to cover a wide range in momentum, the CRID employs two separate radiators, as shown in Figure 2.16. The liquid radiator consists of 1 cm thick trays of C_6F_{14}, with $n = 1.2176$. The gas radiator volume is filled with a mixture of 76% C_5F_{12} ($n = 1.0017$) and

Figure 2.16: Schematic diagram of the barrel CRID, in the rz and $r\phi$ views.

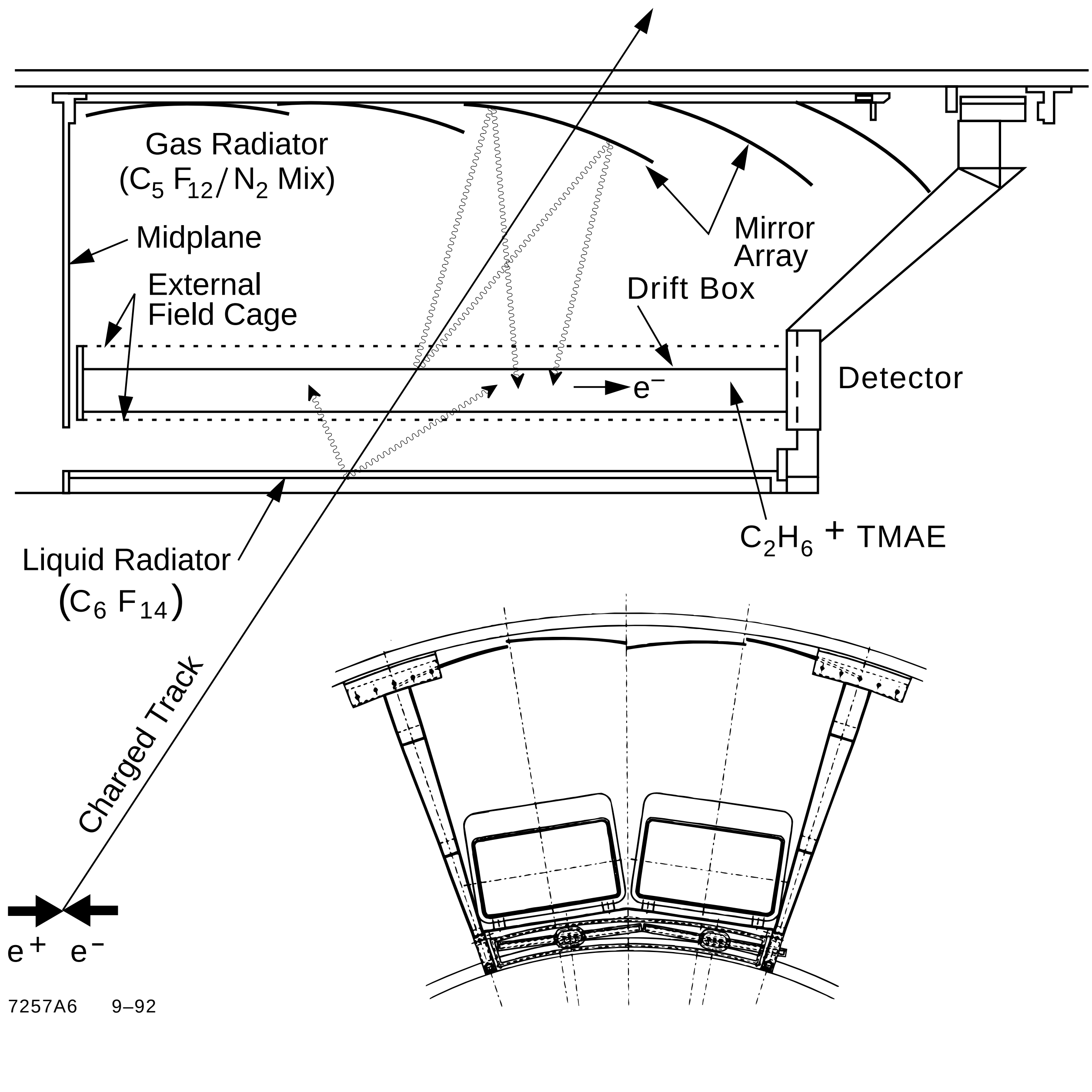

Figure 2.17: Cherenkov angles for $\pi/K/p$ in the liquid and gas radiators as a function of momentum. The thresholds for ring production for each radiator and particle type are visible.

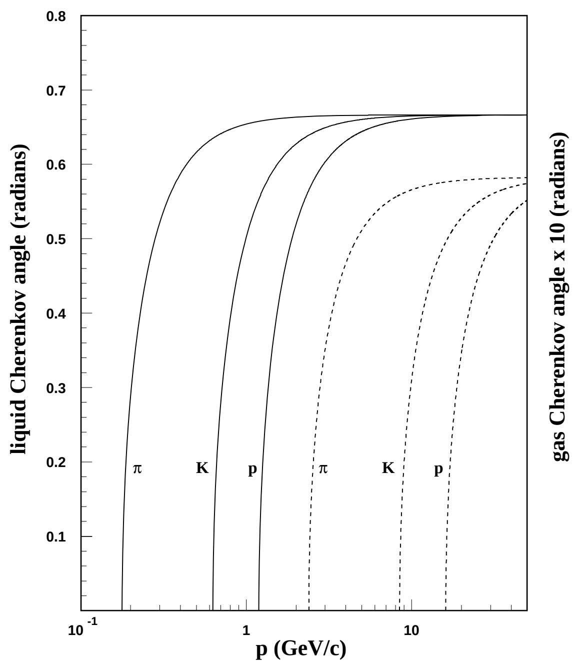

24% N_2 ($n = 1.00032$). The Cherekov angles for $\pi/K/p$ as a function of momentum for the two radiators is shown in Figure 2.17. The combination of the two radiators provides good $\pi/K/p$ separation for the momentum range 0.3 - 30 GeV/c.

The Cherenkov photons emitted by the radiators are detected using time projection chambers (TPCs). Each TPC consists of a photocathode/drift volume coupled to a multiwire proportional chamber (MWPC) as shown in Figure 2.18. Photons produced in the liquid radiator fall directly upon the TPC volume, while those produced in the gas radiator are reflected by an array of spherical mirrors back onto the TPC. The TPC volume contains a mixture of 85% C_2H_6, 15% CO_2 drift gas and 0.1% Tetrakis(diMethylAmino)Ethylene (TMAE) which acts as a photocathode. The Cherenkov photons ionize the TMAE (quantum efficiency $\sim$35%), producing photoelectrons which drift in the 400 V/cm field inside the TPC volume towards the MWPC. The MWPC consists of an array of 93 carbon wires of 7 μm diameter. The photon coordinates are found from the drift time (z), the address of the hit wire (x), and the charge division at the two ends of the wire (y), with resolutions of about 1×1×2 mm in (x, y, z). The average number of detected photons per ring produced by a charged track is 12.8(9.2) for the liquid(gas) radiator, leading to Cherenkov angular resolutions of 16(4.5) mrad.

2.2.5 Liquid Argon Calorimeter

The liquid argon calorimeter (LAC) is the last of the detectors inside the SLD magnet coil, as shown in Figure 2.9. It consists of separate barrel and endcap regions. The barrel LAC covers the polar angle range $|\cos\theta| < 0.84$ and the endcaps extend the coverage to $|\cos\theta| < 0.99$. The LAC is a sampling calorimeter, using lead sheets as both absorbers and electrodes immersed in liquid Ar which acts as the ionization medium. The lead plates are alternately grounded or held at -2 kV to produce a 2 kV potential between any adjacent pair of plates. Particles, both charged and neutral, which enter the LAC generate showers from interactions with the lead plates. The charged component of a shower ionizes the Ar, and the electrons and ions drifting in the field between the plates induce signals on the plates which are digitized. To reduce the channel count, the plates are ganged together into larger units.

The LAC is divided into four radial layers, denoted EM1, EM2, HAD1, and HAD2. The thicknesses of the EM1 and EM2 layers, 6 and 15 radiation lengths respectively, were chosen so that about half of an electromagnetic shower will be deposited in each, with minimal leakage into the HAD layers. The plates are configured as projective towers pointing towards the IP, with angular size ~33 mrad in both polar and azimuthal angle. In the EM layers, the lead plates are 2 mm thick, separated by 2.75 mm of Ar. The two HAD layers sit directly behind EM2, with sufficient thickness (one interaction length each) to contain ~95% of the

Figure 2.18: CRID time projection chamber.

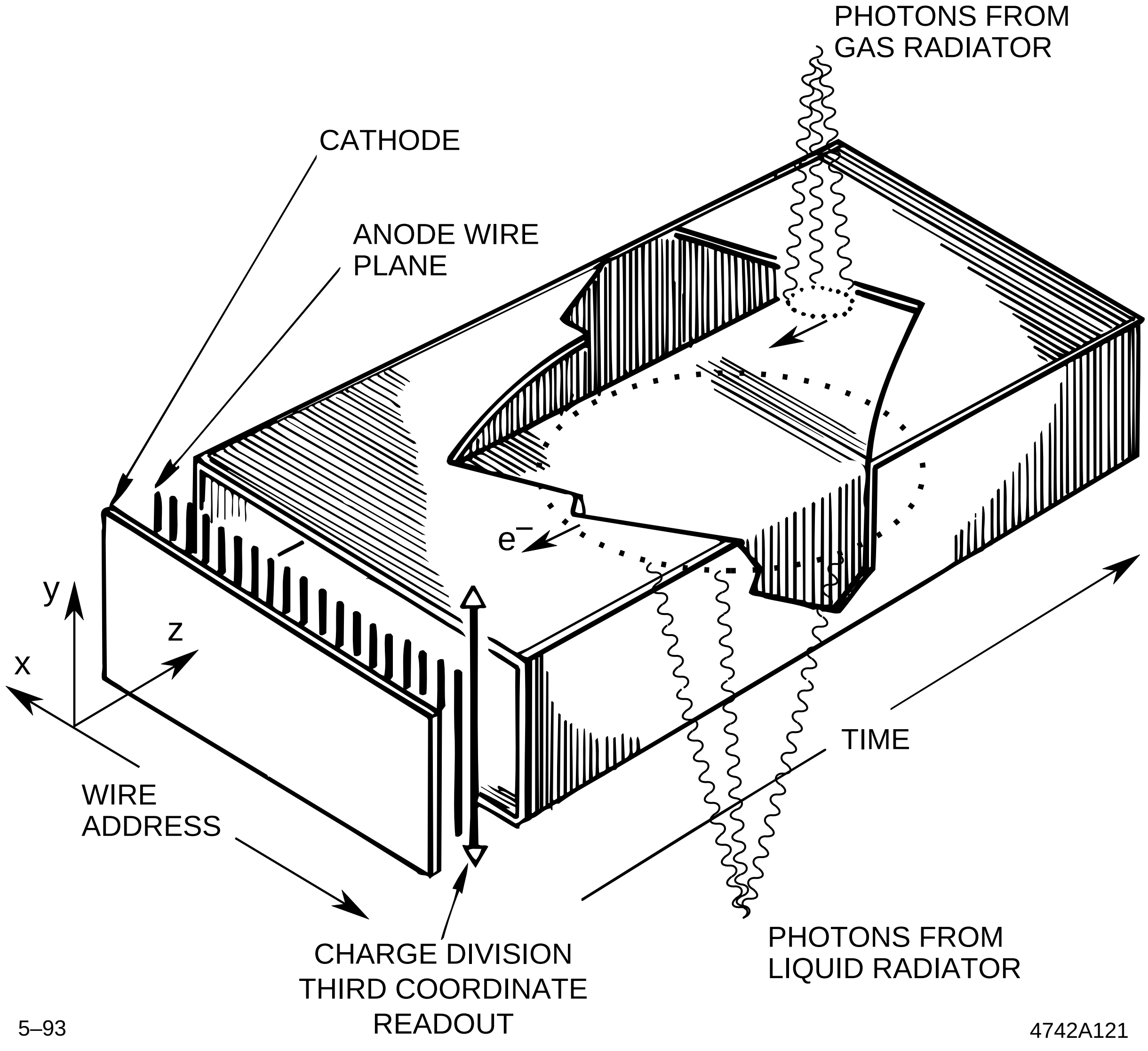

total energy of a Z decay. In the HAD layers, the lead plates are 6 mm thick, with the same 2.75 mm of Ar between. The HAD projective towers are more coarsely segmented than those in the EM layers, covering $\sim$66 mrad in polar and azimuthal angle. A section of the barrel LAC illustrating the layered projective tower geometry is shown in Figure 2.19. The energy resolution of the LAC is approximately $15\%/\sqrt{E}$ for electromagnetic showers and $60\%/\sqrt{E}$ for hadronic showers, with E measured in GeV.

2.2.6 Warm Iron Calorimeter

The SLD is built within a steel structure which provides mechanical support, returns the flux of the solenoidal magnet, and absorbs the residual energy which leaks through the LAC. This steel has also been instrumented to serve as a warm iron calorimeter (WIC). Seventeen layers of 9 mm square Iarocci streamer tubes are installed within the steel as shown in Figure 2.20. On either side of each layer of tubes lies a sheet of plastic, on which copper electrodes have been etched in pad and strip configurations. The pads are arranged in the same projective tower geometry as in the LAC, to augment the shower energy reconstruction. The resolution of this system is poor, however, and the WIC pads information is generally not used. The strip electrodes run both longitudinal and transverse to the beamline, and are used for muon identification.

Figure 2.19: A section of the barrel LAC.

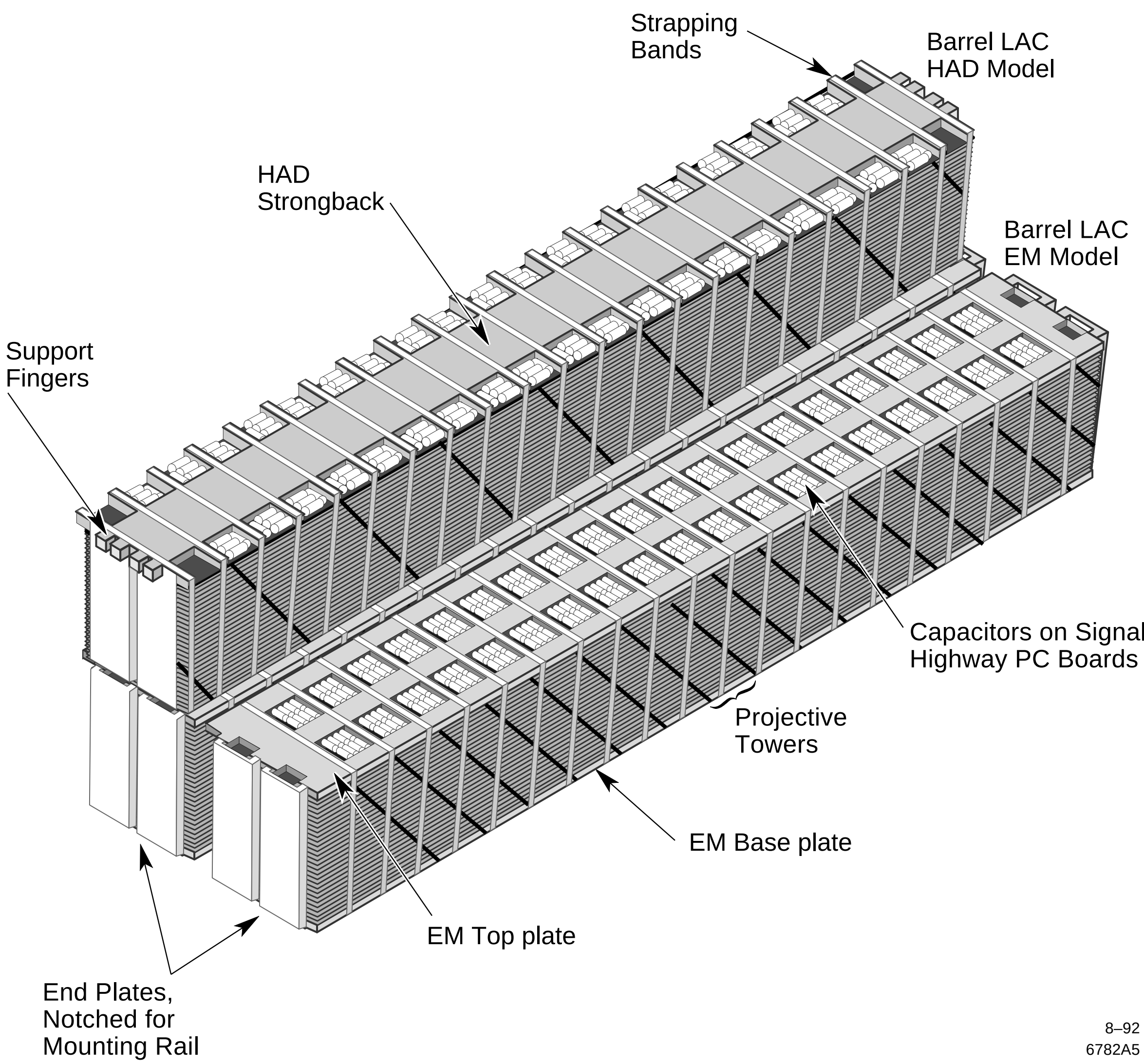

Figure 2.20: Layout of the WIC showing the streamer tubes and readout electrodes.

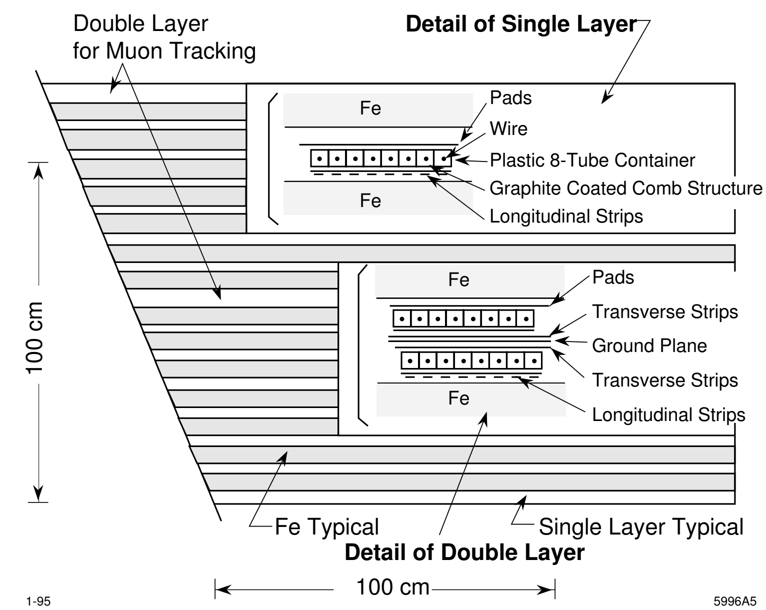

Chapter 3

Simulation Tools

Simulated data generated using Monte Carlo techniques is an essential component of modern particle physics experiments, allowing the estimation of acceptances, backgrounds, and biases that would otherwise be difficult or impossible to determine. A reliable simulation is also useful for optimization of analysis techniques. The simulated data is produced in two steps. The first is to simulate the production and decay of a Z boson, using fundamental physical theory and phenomenological models. The second step is to propagate the generated particles through the detector, simulating the response of each of the detector subsystems to their passage. These simulated detector hits can then be reconstructed and analyzed just like the real data, except with knowledge of the underlying physics.

3.1 Event Generation

The SLD Monte Carlo uses the JETSET 7.4 [32] program to generate physics events. The program parameters have been to tuned to accurately model distributions of inclusive event observables [33]. The generation proceeds in four steps, as shown in Figure 3.1. The first step is the simulation of the $e^+e^- \to \gamma/Z \to q\bar{q}$ process. The effects of initial-state photon

Figure 3.1: The stages of physics event generation: (i) hard scattering, (ii) parton shower, (iii) hadronization, (iv) unstable particle decay.

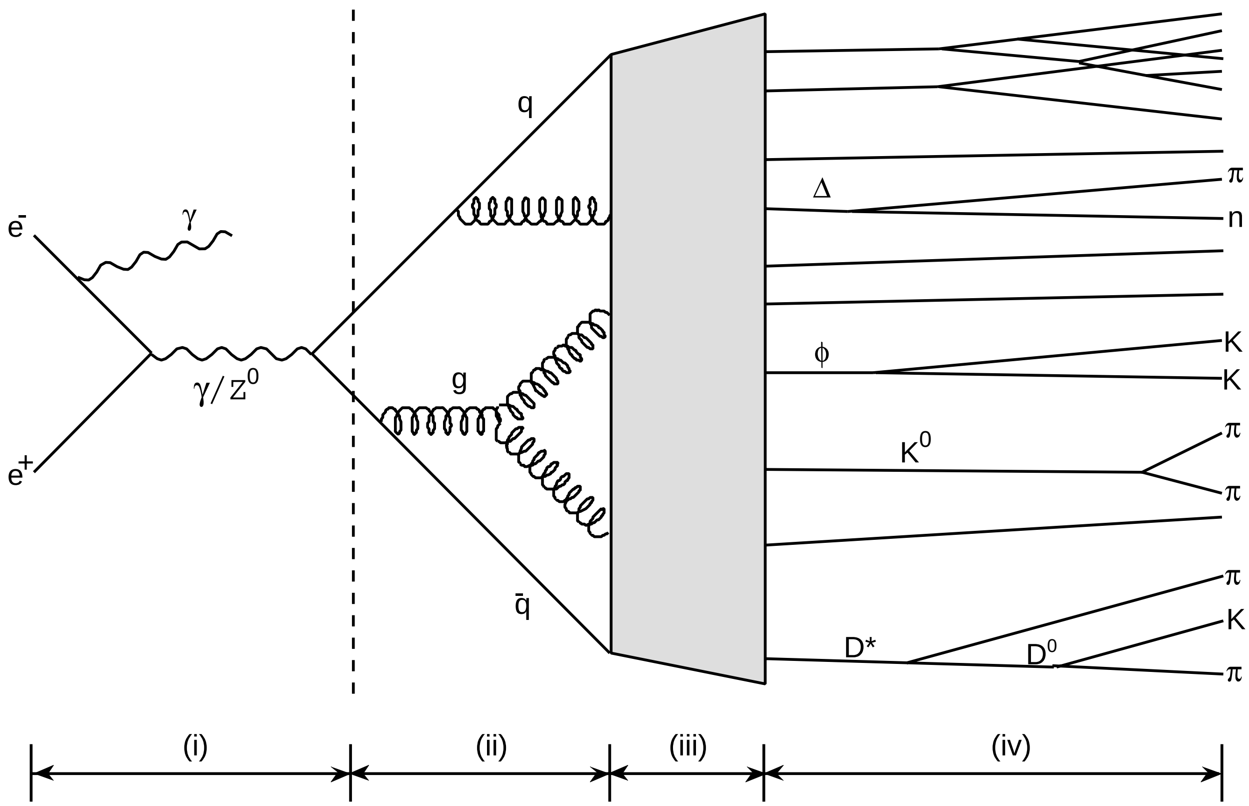

radiation are included, and the $q\bar{q}$ are generated according to the cross section given in Equation 1.20. The flavor of the $q\bar{q}$ pair is chosen randomly, weighted by the strength of the couplings.

The second step is the generation of a parton shower to model the effects of final-state radiation. Branchings of the type $q \rightarrow qg$, $q \rightarrow q\gamma$, $g \rightarrow gg$, and $g \rightarrow q\bar{q}$ are made, based on splitting functions $P_{a \rightarrow bc}(z)$. These splitting functions, which are calculated from simplified matrix elements, express the probability for a parton a to split into bc, where b carries a fraction z of a's energy and c carries the remaining $1-z$. At the end of the parton shower, the event consists of a collection of quarks and gluons. Although it is not shown in Figure 3.1, there can be more quarks than just the primary $q\bar{q}$ pair at this stage, produced via $g \rightarrow q\bar{q}$.

The third step involves converting the showered partons into hadrons. It is not possible to calculate this process perturbatively, because at the energy scales involved the QCD coupling is too large. Therefore, a phenomenological approach is used, the Lund string model. The color fields between the quarks and gluons are modeled as connecting strings, with uniform energy density ~ 1 GeV/fm. As the partons move apart, the energy stored in a string grows until there is enough to pop a $q\bar{q}$ pair out of the vacuum. The initial strings are broken end to end in this way into hadrons, with the energy of each hadron chosen according to a fragmentation function. The fragmentation functions are distributions of z, defined as:

$$z = \frac{(E + p_{\parallel})_{hadron}}{(E + p_{\parallel})_{quark}} \tag{3.1}$$

where the quark subscript refers to the quark currently at the end of the string and the hadron subscript refers to the hadron which will be created from that quark and the $\bar{q}$ pulled out of the vacuum by the string energy. The string is broken along its length into hadrons until all of the initial z is gone. For Z decays into light quarks the Lund symmetric function [34] is used, while for decays into c and b quarks the Peterson function [35] is used. These functions are shown in Figure 3.2. Because the Peterson functions are peaked at high z, the initial hadron created containing the heavy quark will carry a large fraction of the energy of the initial heavy quark. The parameters of the JETSET model related to parton showers and hadronization have been tuned to match inclusive event distributions in the SLD data [33].

The last step in physics event generation is the decay of unstable particles produced in the hadronization step. All short-lived hadrons which could only extremely rarely reach the beampipe are forced to decay at this stage, with the decay positions distributed according to the lifetimes of the particles. This includes all strong and electromagnetic decays, and weak deacys of hadrons containing c and b quarks. The particle decay procedure, using tables

Figure 3.2: Fragmentation functions for uds, c, and b events.

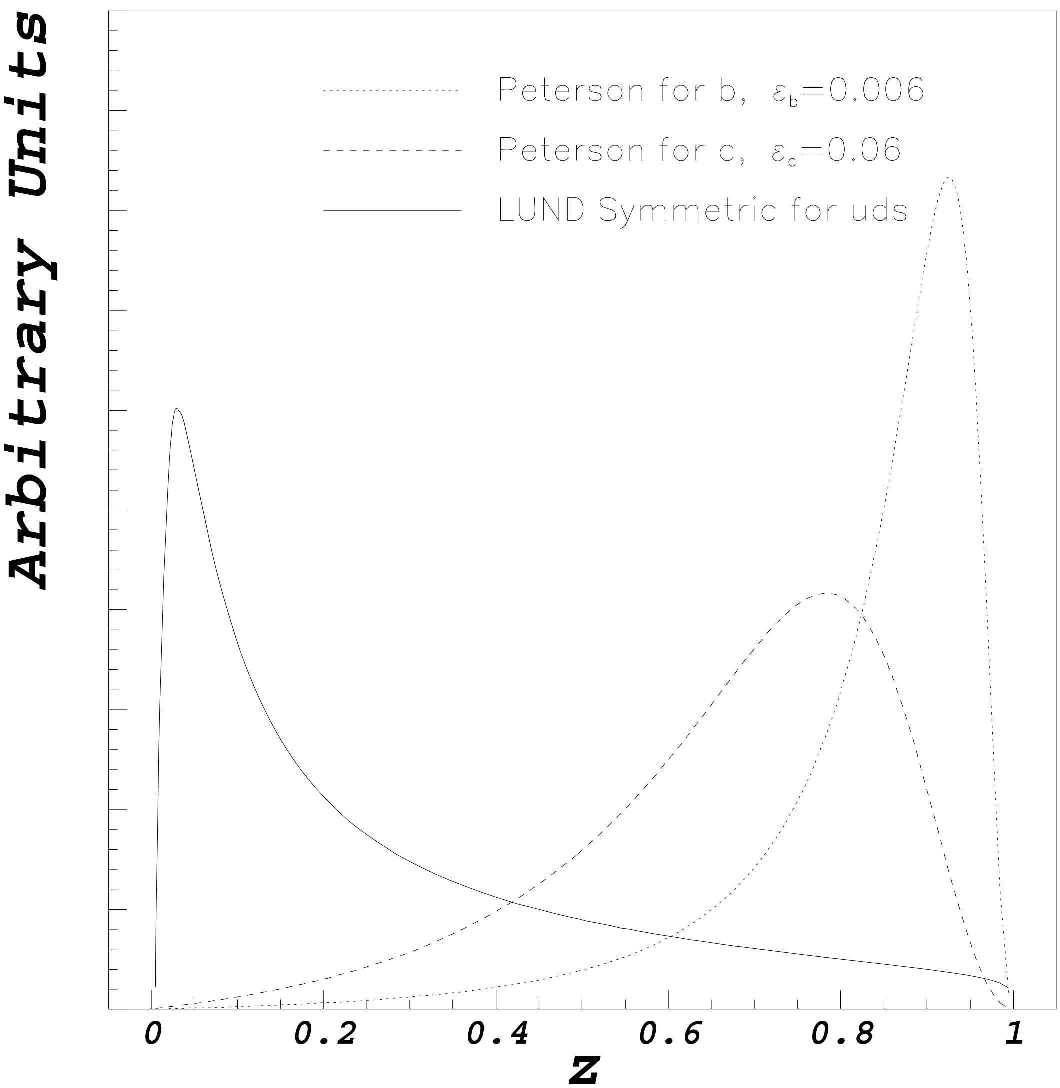

of masses, lifetimes, and branching ratios, is iterated until only long-lived hadrons remain. Unstable particles with long lifetimes such as K_s and Λ are not processed at this step, since they may reach the detector material. They are decayed according to their lifetimes during the detector simulation stage. Hadrons containing b quarks are processed using the CLEO B-decay model [36] tuned to reproduce the existing data on B decays, while other particles are handled by the internal JETSET decay machinery.

3.2 Detector Simulation

Once a physics event has been generated, the response of the detector to the resulting particles must be modeled so that the simulated data resembles the real data as closely as possible. The SLD Monte Carlo uses the GEANT [37] program for this detector modeling. The program uses a detailed description of the detector geometry as input, which specifies the position and composition of every detector component. As GEANT tracks each particle, it records the amount of energy deposited in each detector component by ionization, Cherenkov radiation, synchrotron radiation, and other processes. For each component, response functions are specified which convert the deposited energy into realistic detector signals.

These detector signals can then be processed using the same techinques used for the real data to find tracks, calorimeter clusters, etc. To simulate detector backgrounds and noise, the detector is read out at random intervals during data taking. The hits from these random events are overlaid onto the hits generated by GEANT before the event is processed.

The two aspects of detector modeling which are most important for the analysis presented in this Thesis are tracking efficiency and track position resolution.

3.2.1 Tracking Efficiency

Tracking efficiency is the fraction of charged particles which are reconstructed as tracks in the detector. For the analysis presented in this Thesis, only tracks which have associated VXD hits will be used and only the efficiency for finding these is considered. The total efficiency is then composed of three sources: CDC track-finding, VXD-vector finding, and CDC+VXD linking. A failure in any of these will cause the track to be lost for analysis purposes.

One way to check the simulation against the data is to simply compare the number of reconstructed tracks per event. However, this method suffers from significant uncertainties associated with the number of charged particles generated by the simulation, and so is not a test of the detector modeling alone. Two alternative methods with less dependence on the generation phase have been developed.

The first method uses the fraction of CDC tracks which have associated VXD hits. A loose requirement that the CDC track point towards the IP is imposed to reduce the level of K_S decay and detector interaction products, which because they do not pass through the VXD should not have any hits. Comparison of this fraction with the data indicates that the tracking efficiency in the simulation is 1.5% too high. An advantage of this method is that it can be performed in bins of $\cos\theta$ and phi to check for any local efficiency discrepancies. The track linked fractions are plotted versus $\cos\theta$ and ϕ in Figure 3.3 for the data, the standard Monte Carlo, and the corrected Monte Carlo. A disadvantage of this method is that it gives no information as to the source of the efficiency discrepancy. It is not possible to tell whether the problem lies with the VXD-vector reconstruction or the linking of the CDC and VXD segments.

The second method uses the net charge Q_{vtx} of b-hadron vertices selected using the procedure developed in Chapter 4. The width of the Q_{vtx} distribution is a good probe

Figure 3.3: Fractions of track which have associated VXD hits, in bins of $\cos\theta$ (left) and ϕ (right), for the data, the standard Monte Carlo, and the corrected Monte Carlo.

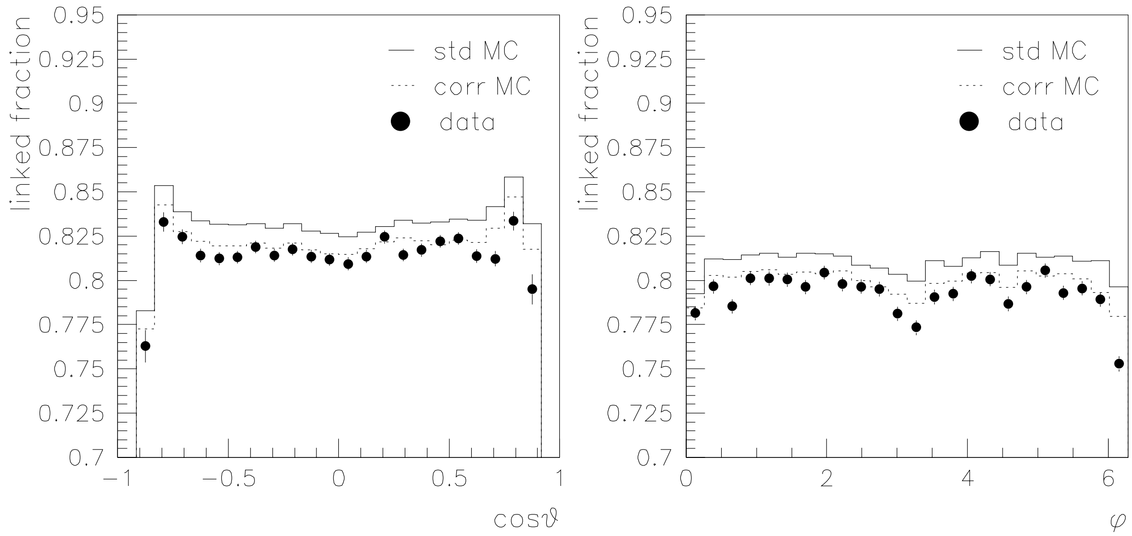

of the tracking efficiency and insensitive to the generated b-hadron decay charged particle multiplicity. Comparing the Q_{vtx} width using only the full CDC+VXD tracks contained in the vertex indicates that the simulated tracking efficiency is 1.5% too high, in excellent agreement with the first method. This method can also be used to check the VXD-vector reconstruction efficiency, by converting 1.5% of the tracks in the simulation into VXD-vectors by dropping the CDC component. Comparing the Q_{vtx} width using both CDC+VXD tracks and attached VXD-vectors indicates that 75% of the new VXD-vectors should be discarded. The tracking efficiency discrepancy is therefore mostly due to VXD-vector reconstruction, not to CDC-VXD linking. The Q_{vtx} distributions for the data, the standard Monte Carlo, and the corrected Monte Carlo are shown in Figure 3.4.

3.2.2 Track Position Resolution

The position and orientation of each of the CCD ladders in the VXD has been determined using the data, following an alignment procedure described in [28]. However, evidence of

Figure 3.4: Reconstructed vertex charge Q_{vtx} for the data, the standard Monte Carlo, and the corrected Monte Carlo.

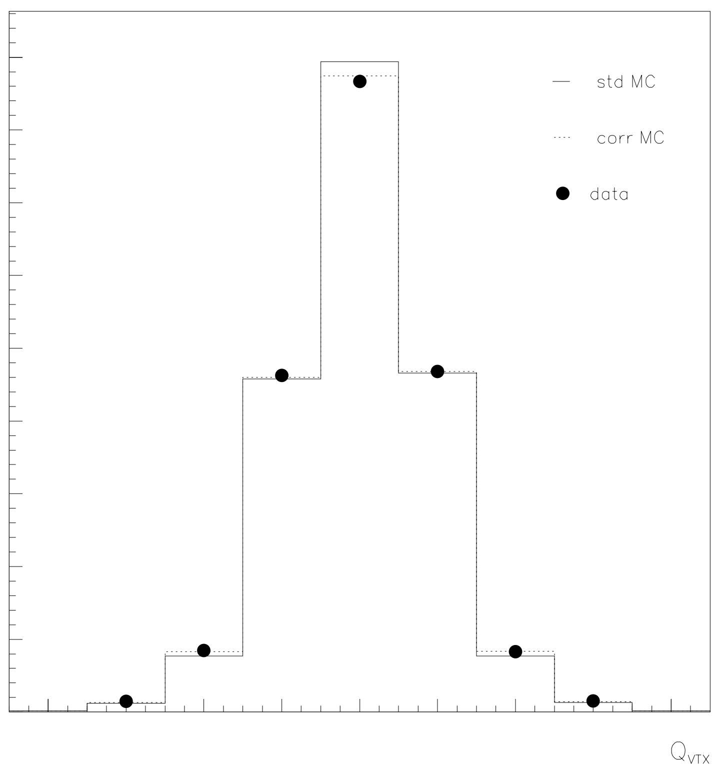

residual misalignment can be seen in the track impact parameter distributions. These effects are particularly noticeable in the rz projection for high momentum tracks at large $|\cos\theta|$, where differences in the average impact parameter between the Monte Carlo and data can be as high as 40 μm. The source of this problem is thought to be related to the shapes of the CCD ladders, which are flexible enough to curl at the edges. Due to low statistics this effect is difficult to constrain in the alignment procedure, which makes no physics assumptions and only uses the relative positions of VXD hits.

A set of corrections to the simulation has been constructed to mimic this misalignment. The positions of the tracks are shifted in space to reproduce the average impact parameters seen in the data, in bins of ϕ and $\cos\theta$. In contrast to the alignment procedure this method assumes the accuracy of the generated impact parameter distribution in the simulation. After moving the tracks, a second pass determined that no additional smearing of the VXD hit positions was required to adequately model the data distributions. The miss distance $\delta z_{IP} = z_{trk} - z_{IP}$ of tracks to the reconstructed event e^+e^- interaction point (IP) in z is plotted in Figure 3.5 for the data, the standard Monte Carlo, and the corrected Monte Carlo.

In the following chapters many comparisons between the data and Monte Carlo will be shown. After applying the corrections described above the simulation and data are generally found to be in excellent agreement.

Figure 3.5: Track miss distances δz_{IP} to the IP for the data, the standard Monte Carlo, and the corrected Monte Carlo.

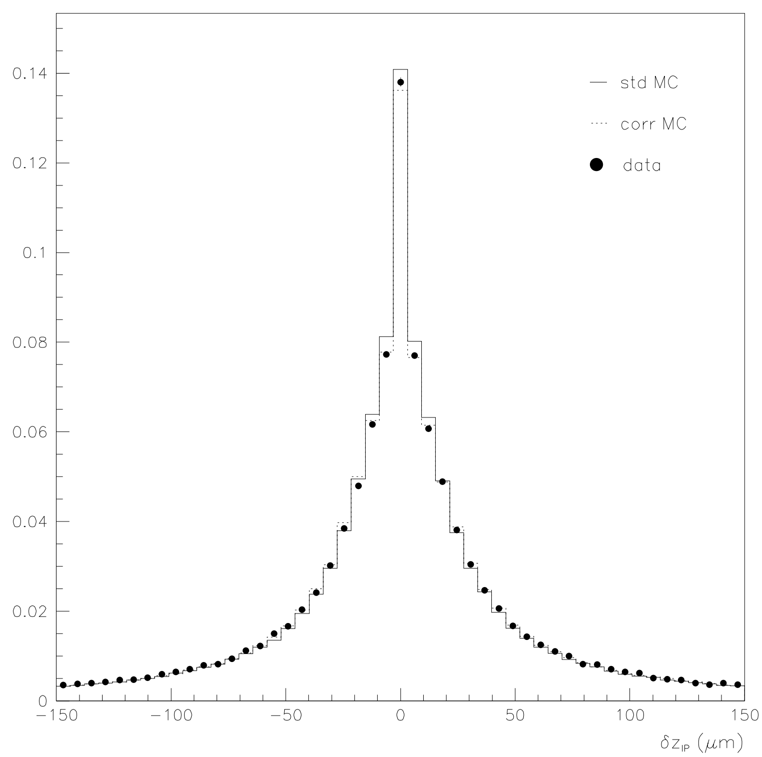

Chapter 4

Event Selection and Tagging

In order to make a measurement of $\tilde{A}^f_{FB}$, a sample of Z decays into the fermion of interest must be isolated. The selection of events for this analysis is done in two stages. The first is to separate hadronic decays of the Z from leptonic decays and machine-related backgrounds. From these hadronic events, samples of Z decays to c and b quarks are selected by searching for displaced vertices. Because the direction of the quark is also needed, a technique for identifying a tagged heavy hadron as containing a heavy quark or antiquark has been developed.

The heavy flavor tagging procedure developed for this analysis makes use of artificial neural networks. A short review of classification using neural networks is given in Section 4.2

4.1 Hadronic Event Selection

The events which were written to tape by the SLD trigger system are first passed through a filter to improve the background rejection. This filter requires either a >1 GeV/c track in the drift chamber or energy deposition in the LAC inconsistent with beam-gas or SLC muon background events. The combination of the trigger system and this filter is estimated to be 92% efficient for hadronic Z decays [38]. The remaining events are processed by the SLD offline reconstruction software and written to data summary tapes (DST). These tapes contain the tracks, calorimeter clusters, etc. which are used for physics analyses.

The DSTs contain all identified Z decays, including those into lepton pairs. Hadronic decays are isolated based on the visible energy and track multiplicity in the event. There must be at least seven CDC tracks with $p_\perp > 0.2$ GeV/c and $z_{IP} < 5$ cm. At least three of the CDC tracks must have associated hits in the vertex detector. The visible energy measured using CDC tracks must exceed 18 GeV. The event thrust vector $\hat{t}$, defined as the axis which maximizes the event thrust T:

$$T = \frac{\sum_i |\vec{p}_i \cdot \hat{t}|}{\sum_i |\vec{p}_i|} \tag{4.1}$$

where the sum is over the reconstructed calorimeter clusters in the event, must satisfy $|\cos\theta_{\hat{t}}| < 0.7$ and $T > 0.8$ to ensure that the event is contained within the acceptance of the tracking detector and can be separated into two well-defined hemispheres. Calorimeter clusters rather than CDC tracks are used to determine $\hat{t}$ to avoid biases caused by the limited CDC acceptance.

The quantities used in hadronic event selection are shown in Figure 4.1. A total of 228712 events from the SLD 1996-98 data pass this selection. Background, predominately due to τ pairs, is estimated at $< 0.1\%$.

4.2 Artificial Neural Networks

A common problem in the analysis of particle physics data is that of classification. From a sample of items, such as jets or tracks, which can be grouped into a set of categories a_i a subsample enriched in one of the categories must be selected. Typically this is done using

Figure 4.1: Distributions of event selection variables: (a) Number of CDC tracks, (b) visible energy, (c) thrust axis polar angle, (d) thrust magnitude. The points (histogram) denote the data (Monte Carlo). The arrows indicate the regions which pass the cuts, which are applied cumulatively for each successive plot. Only a subset of the 1998 data is shown.

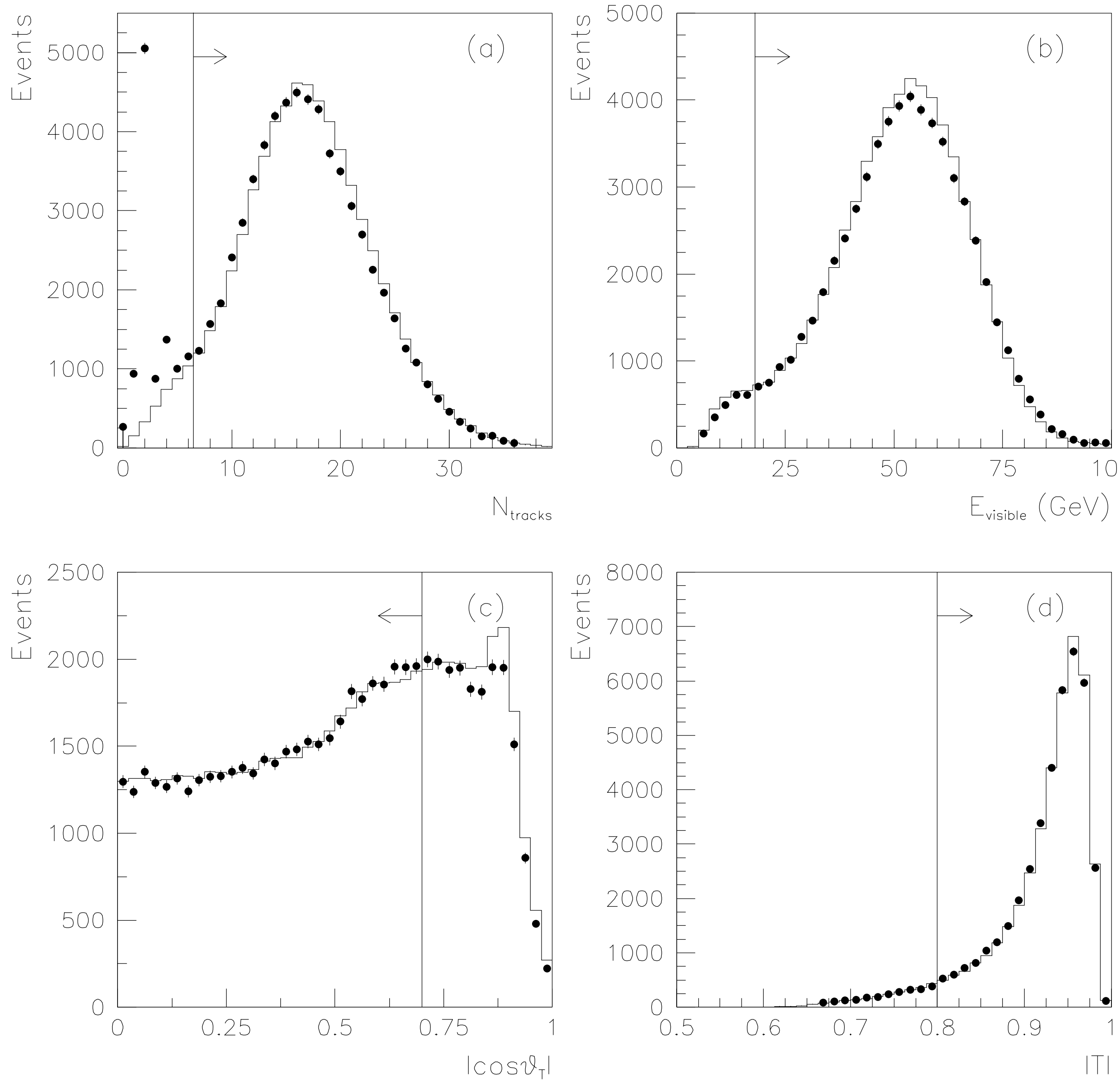

a set of one or more variables x_i, which are measureable properties of the items and which exhibit some separation between the "signal" category and the others. A region in the x_i space is chosen which includes the desired rate of signal relative to the other categories. In general the x_i are correlated, so simply cutting on each x_i ignores information which could otherwise improve the selection. For two x_i a scatter plot can be used to determine signal regions by eye, but for more than two x_i this approach becomes impractical. What is needed is a method to combine all of the information contained in the x_i into a smaller set of variables y_k, for which it is easier to find signal regions. One of the more popular of such methods is the use of artificial neural networks.

Artificial neural network systems have found many applications in particle physics [39], including classification, pattern recognition, and function approximation. Neural networks can be constructed using a wide variety of architectures and learning algorithms, but the most common for classification purposes are feed-forward networks trained using back-propagation. The discussion here will be restricted to this type.

A typical feed-forward network architecture is shown in Figure 4.2. The basic elements of a neural network are nodes and links. In a feed-forward network the nodes are arranged in layers as shown, with links only between nodes in adjacent layers. The first layer of nodes corresponds to the input variables x_i, with one node for each variable. Next come any number of hidden layers, with any number of nodes in each. In practice networks with more than two hidden layers are rarely used, and one hidden layer with one more node than in the input layer is sufficient for most classification problems. The last layer contains output nodes, which contain the reduced set of variables y_k discussed above. Often there will only be one output node, although more may be used if the network is to be used to sort the items into more categories than just signal/background.

As its name suggests, a feed-forward network is evaluated layer by layer, so that the input variables x_i are propagated step-by-step through the network to the output layer. The value

Figure 4.2: Schematic diagram of a typical feed-forward neural network.

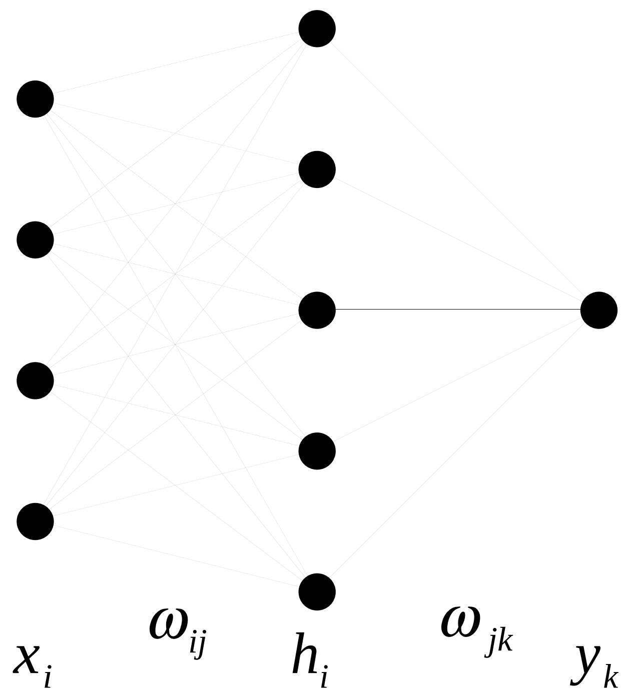

of a node h_j in the first hidden layer is given by the output of a function $g(z)$:

$$h_j = g(\sum_i \omega_{ij} x_i + \theta_j) \tag{4.2}$$

where ω_{ij} is the weight assigned to each link between the input and hidden layers, θ_j is the threshold for each hidden node h_j, and $g(z)$ is the node activation function. For classification problems, a sigmoid activation function:

$$g(z) = \frac{1}{2}(1 + \tanh z) = \frac{1}{1 + e^{-2z}} \tag{4.3}$$

is generally used, so that each node (other than the inputs) acts in an almost binary on/off fashion. If there are more hidden layers they are evaluated in turn, replacing the input node values x_i with the appropriate h_j values from the previous layer. The output layer values y_k

are given by:

$$y_k = g\left(\sum_j \omega_{jk} h_j + \theta_k\right) \tag{4.4}$$

where ω_{jk} is the weight for a link between the last hidden and output layer, and θ_k is an output node threshold. The ω's and θ's, collectively denoted as a vector $\vec{\omega}$, are free parameters of the network, which are determined by training against test samples.

The training samples are collections of items for which both the input patterns x_i and the desired network outputs t_k are specified. These samples are drawn from the Monte Carlo simulation, which provides good modeling of the data x_i distributions and knowledge of the true category for each item. The training procedure involves minimization of an error measure, usually a mean square error:

$$E = \frac{1}{2N_p} \sum_p \sum_k (y_k^{(p)} - t_k^{(p)})^2 \tag{4.5}$$

where N_p is the number of patterns (items) in the training set, and the (p) denotes the observed and target network outputs for a particular input pattern $x_i^{(p)}$. Training is therefore analogous to performing a χ^2 fit for the parameters $\vec{\omega}$.

Many specialized techniques have been developed to minimize $E(\vec{\omega})$, but the simplest and most commonly used is gradient descent. This method involves updating $\vec{\omega}$ by:

$$\Delta\vec{\omega} = -\eta \nabla E \tag{4.6}$$

where η is the learning rate, typically ~ 0.1. The derivatives of E are computed starting with the links between the last hidden layer and the output layer and proceeding back to the input layer. The intermediate layer derivatives make use of those calculated for the later layers, allowing computation of the full ∇E in one traversal of the network. The differences between y_k and t_k are thus said to be "back-propagated" through the network to update the weights and thresholds. The weights may be updated after any number of patterns, but the fastest convergence is obtained by updating after each individual pattern has been presented to the network.

Starting from an initial $\vec{\omega}$ with elements randomly distributed in $[-1, 1]$, the training sample is iterated though the network and the weights updated until E is minimized. Usually this will require many passes through the training sample, called cycles. For each cycle the patterns are shuffled randomly to minimize the effects of false minima. Starting with a high learning rate will allow a quick approach to the neighborhood of minimum E, where η should be reduced to prevent oscillations about the minimum. Also recommended is to transform and scale the x_i so that they are approximately the same size and shape, so that no one variable dominates at first. As the network is trained, the error measure E is periodically evaulated for a separate validation sample. Comparison of this with the training sample error allows confirmation that the network is being trained on the general characteristics of the patterns and is not simply learning to recognize statistically insignificant features of the training sample. Once the network has been trained and validated, the network using the final $\vec{\omega}$ values is ready to be used for classifying real data.

To train and evaluate the networks used in this Thesis, the Stuttgart Neural Network Simulator [40] software package was used. All of the networks used in this Thesis are configured in the $N : (N + 1) : 1$ topology for N variables, so that there is one hidden layer containing one more node than in the input layer, and one output node. The networks were trained on a subsample of the SLD Monte Carlo from the 1998 run period.

4.3 Heavy Flavor Tagging

Decays of a Z boson into charm and bottom quarks can be distinguished from those into light flavors by searching for heavy hadrons. Because they are produced with high energy and have long lifetimes, heavy hadrons generally travel distances of millimeters before decaying.

The method used for these results is to search for vertices of tracks displaced from the event interaction point (IP). Figure 4.3 illustrates the typical configuration of particle jets produced by light-flavor (*uds*), charm, and bottom quarks. In a *uds* jet all of the tracks will appear to come from one point in space, the event interaction point (IP). In a charm jet some of the tracks may not point back to the IP, and if the c hadron decays into more than one charged particle there will be a secondary vertex (SV) in addition to the IP. Bottom jets will also exhibit secondary vertices, and if there are sufficient particles produced at the b and c decay points it is possible to find more than one displaced vertex.

An important case for tagging b jets is when there is only one stable charged particle produced at the b decay point. If the tracks from the c decay point form a vertex which is successfully reconstructed, the single track from the b decay will not point to that vertex and may be lost. The tagging algorithm described in this chapter therefore includes an extra step beyond vertex reconstruction to recover these tracks.

4.3.1 IP Reconstruction

To search for displaced vertices the position of the IP must be precisely known. The position of the IP in the plane transverse to the beam axis is determined by fitting all of the tracks in an event to a common vertex. Because the SLC luminous region is small and stable in the xy plane, sets of 30 time sequential hadronic events are averaged to obtain a more precise determination of the xy IP position. This averaging removes any dependence of the resolution on the $\cos\theta_{\hat{t}}$ of the event, because $\hat{t}$ is isotropic in ϕ. This also reduces biases due to tracks from heavy hadron decays, which in general do not point back to the IP. The resolution of this method can be checked in the data using decays of the Z into muon pairs. The impact parameters of the two tracks in the xy plane to the estimated IP position are

Figure 4.3: Schematic illustration of the track patterns in uds, c, and b quark jets.

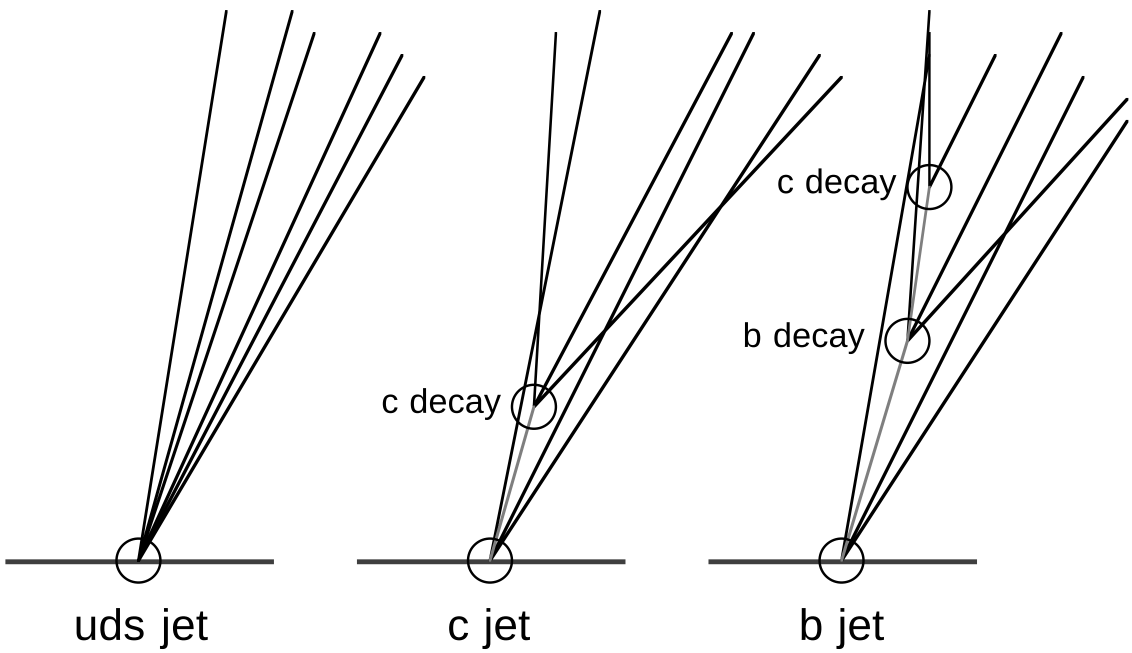

plotted in Figure 4.4. From the width of this distribution (8.2 μm) and the tracking $r\phi$ resolution (7.55 μm), the xy IP resolution is found to be $\sqrt{(8.20)^2 - (7.55)^2} = 3.2$ μm.

Because the SLC luminous region is larger in z (700 μm), the z position of the IP must be found event-by-event. Tracks with VXD hits are extrapolated to their point of closest approach (POCA) in xy to the precisely determined transverse IP position. Tracks with impact parameters >500 μm or $> 3\sigma$ from the IP are excluded, and the z position of the IP is taken from the median z at POCA of the remaining tracks. The resolution of this method is found from the simulation to be 10/11/17 μm for light/charm/bottom events.

4.3.2 Secondary Vertex Reconstruction

Secondary vertices are found using a topological algorithm [41]. This method searches for space points in 3D of large track density. Each track is parameterized by a Gaussian probability density tube $f(\vec{r})$ with a width equal to the uncertainty in the track position at its

Figure 4.4: Muon-pair xy impact parameter to IP.

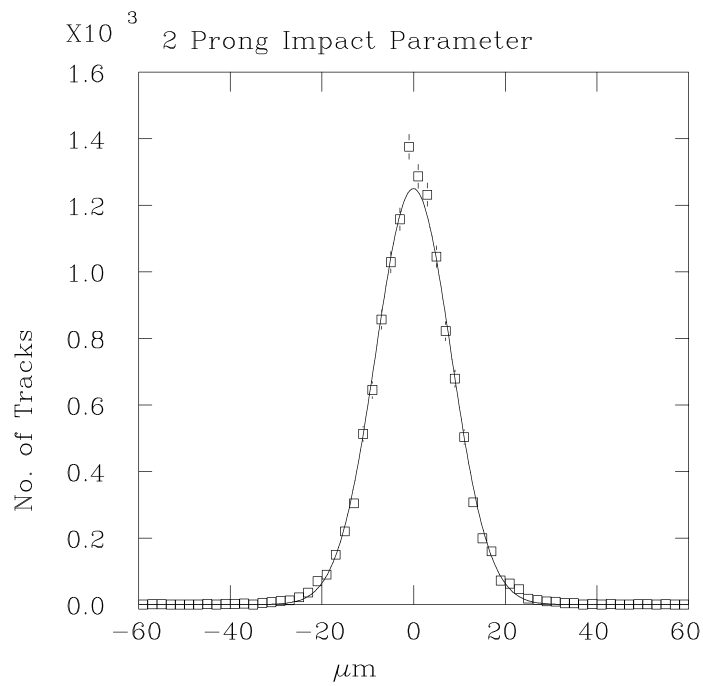

POCA to the IP, $\vec{r}_0$:

$$f(\vec{r}) = \exp\left\{-\frac{1}{2}\left[\left(\frac{x-(x_0+y^2\kappa)}{\sigma_1}\right)^2 + \left(\frac{z-(z_0+y\tan\lambda)}{\sigma_2}\right)^2\right]\right\}. \tag{4.7}$$

The first term is a parabolic approximation to the track's circular trajectory in the xy plane, where κ is a function of the track's charge and transverse momentum and of the SLD magnetic field. The second term represents the linear trajectory of the track in the rz plane, where λ is the track dip angle from the vertical. The σ parameters are the uncertainties in the track positions after extrapolation to $\vec{r}_0$ for the two projections.

The function $f_i(\vec{r})$ is formed for each track under consideration and used to construct the vertex probability function $V(\vec{r})$. Also included is $f_0(\vec{r})$, a $7 \times 7 \times 20$ μm $(x \times y \times z)$

Figure 4.5: Projections onto the xy-plane of (a) track and (b) vertex functions.

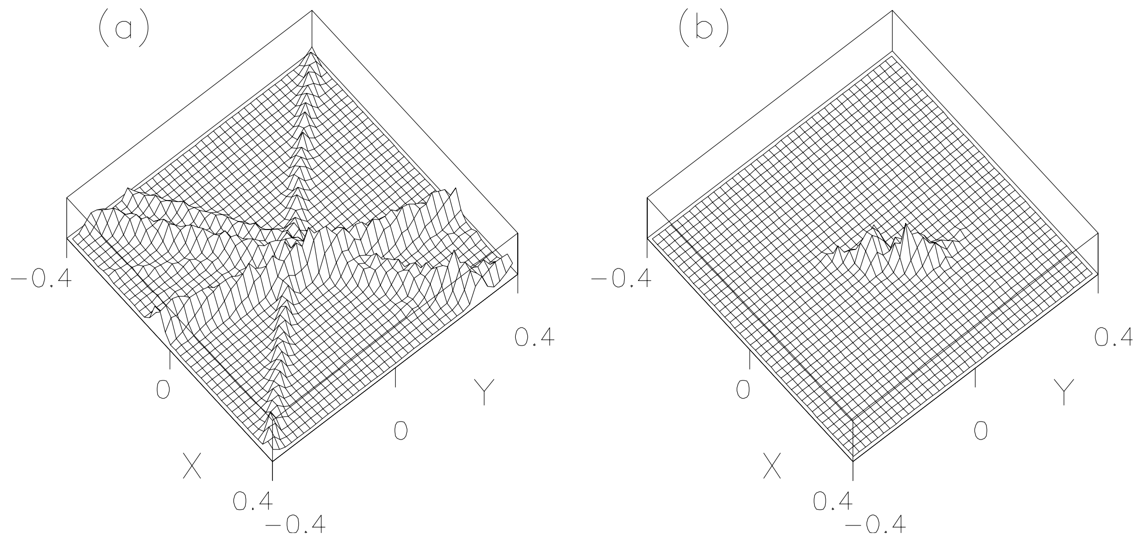

Gaussian ellipsoid centered at the IP position.

$$V(\vec{r}) = \sum_i f_i(\vec{r}) - \frac{\sum_i f_i^2(\vec{r})}{\sum_i f_i(\vec{r})} \tag{4.8}$$

The track and vertex functions are shown in Figure 4.5 for a simple Monte Carlo event. Secondary vertices are found by searching for local maxima in $V(\vec{r})$ that are well-separated from the peak at the IP position. The tracks whose density functions contribute to a local maximum are then identified as originating from a secondary vertex (SV).

A loose set of cuts are applied to tracks used for secondary vertex reconstruction. Tracks are required to have ≥ 3 VXD hits and $p_\perp > 250$ MeV. Tracks with 3D impact parameter > 3 mm or consistent with originating from a γ, K^0, or Λ^0 decay are also removed. The event is divided into two hemispheres using the thrust axis, and the vertexing procedure is performed in each using only the tracks in that hemisphere.

The identified vertices are required to be within 2.3 cm of the center of the beam pipe to remove false vertices from interactions with the detector material. A cut on the secondary vertex invariant mass M of $|M - M_{K_S^0}| < 0.015$ removes any K_S^0 decays that survived the track cuts. The remaining vertices are then passed through a neural network to further improve the background rejection. The input variables are the flight distance from the vertex to the IP (D), that distance normalized by its error (D/σ_D), and the angle between the flight direction $\vec{D}$ and the total momentum vector of the vertex $\vec{P}$ (ϕ_{PD}). These quantities are shown in Figure 4.6, along with the output value of the neural network (y_{vtx}). A good vertex is defined as one which contains only tracks from heavy hadron decays, with no tracks originating from the IP, strange particle decays, or other sources. Vertices with $y_{vtx} > 0.7$ are retained. At least one secondary vertex passing this cut is found in 72.7% of bottom, 28.2% of charm, and 0.41% of light quark event hemispheres in the Monte Carlo. Around 16% of the hemispheres in b events have more than one selected secondary vertex.

4.3.3 Track Attachment

Due to the cascade nature of b hadron decays, tracks from the heavy hadron may not all originate from the same space point. Therefore, a process of attaching tracks to the secondary vertex has been developed to recover this information using a second neural network. The first four inputs are defined at the point of closest approach of the track to the axis joining the secondary vertex to the IP. They are the transverse distance from the track to that axis (T), the distance from the IP along that axis to the POCA (L), that distance divided by the flight distance of the SV from the IP (L/D), and the angle of the track to the IP-SV axis (α). The last input is the 3D impact parameter of the track to the IP normalized by its error (b/σ_b). These quantities are shown schematically in Figure 4.7. The distributions are shown in Figure 4.8, along with the neural network output value (y_{trk}). The network is trained to accept only tracks which come from a b or c hadron decay, and to reject tracks from the IP or from strange particle decays. To optimize the charge reconstruction, any

Figure 4.6: Distributions of seed vertex selection variables: (a) distance from IP D, (b) normalized distance from IP D/σ_D, (c) angle between flight direction and vertex momentum ϕ_{PD}, (d) neural network output y_{vtx}. A good vertex contains only heavy hadron decay tracks. The arrow indicates the accepted region.

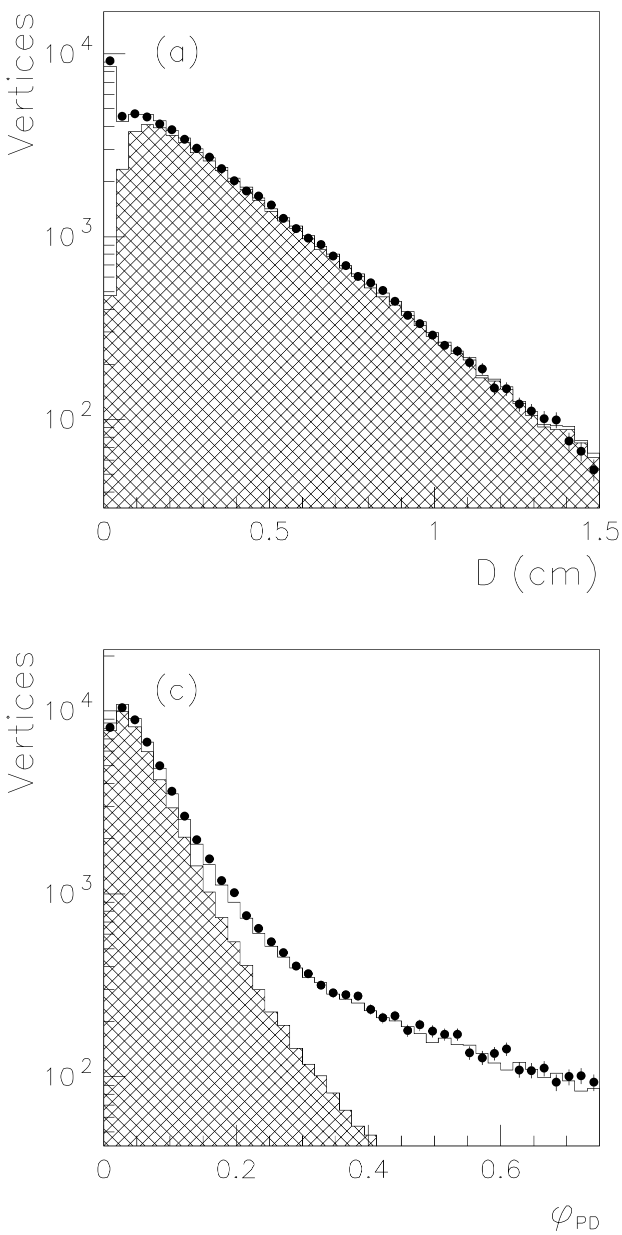

Figure 4.7: Schematic illustration of the quantities used in the track-attachment procedure described in the text (not to scale).

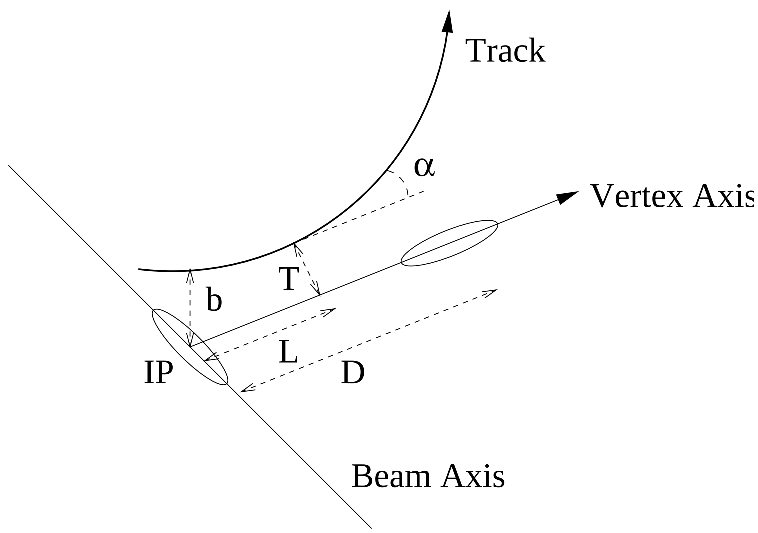

track not already part of a good SV and with ≥ 2 VXD hits is tried, including those which were removed from the SV-finding procedure. If more than one secondary vertex was found in the hemisphere the attachment procedure is tried for each track-SV combination. Tracks with $y_{trk} > 0.6$ are added to the list of secondary vertex tracks.

4.3.4 VXD-alone tracking

Because the SLD tracking system is not 100% efficient, not all of the heavy hadron decay products will be found even for perfect secondary vertex reconstruction. The Monte Carlo indicates that ∼90% of the charged decay products of a heavy hadron produce a VXD-linked track. Part of the inefficiency can be recovered by using tracks reconstructed in the vertex detector alone. Vectors of VXD hits not associated with a CDC track are used, where there is a least one hit on each of the three VXD layers. Including these vectors raises the tracking efficiency to ∼97% for heavy hadron decay products. Using the VXD hits in the vector a parabolic trial track is constructed. In the same way as for the cascade tracks, a third neural

Figure 4.8: Distributions of cascade track selection variables: (a) T, (b) L, (c) L/D, (d) α, (e) b/σ_b, (f) neural network output y_{trk}. A good track is one which originates from a heavy hadron decay. The arrow indicates the accepted region.

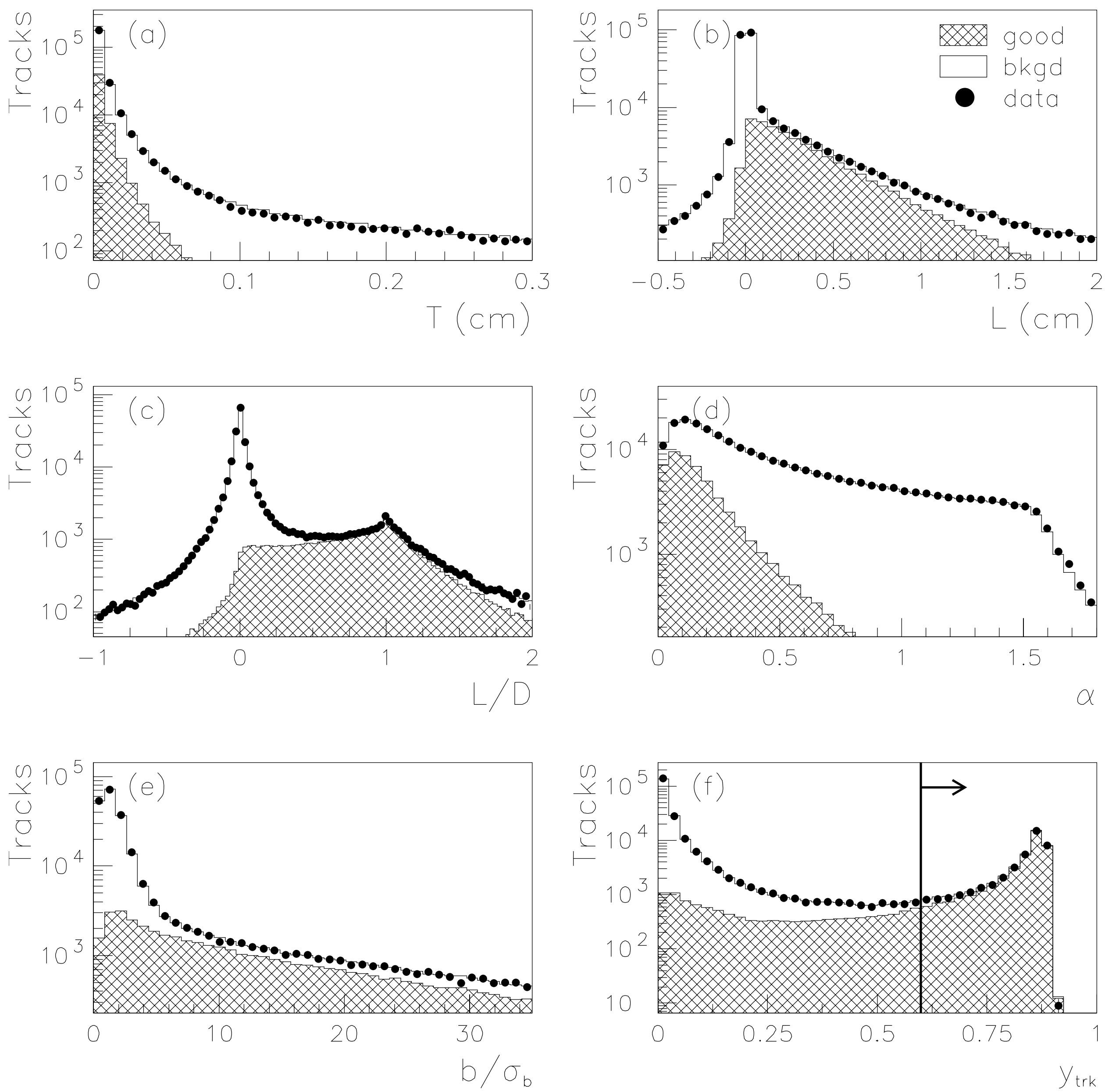

network is then used to select the trial tracks consistent with the heavy hadron decay chain, using as inputs the first four variables used for the track attachment neural network (T, L, L/D, α). These quantities are shown in Figure 4.9, along with the neural net output value (y_{vec}). The normalized impact parameter is not used because the track position error can't be reliably calculated for the trial tracks due to the poor momentum resolution. Vectors with $y_{vec} > 0.5$ are added to the secondary vertex track list.

Once a vector has been attached to a secondary vertex, the parabolic fit is repeated with the vertex as an additional space point to improve the curvature determination. The charge of the underlying particle is correctly found from this fit for $\sim 85\%$ of the attached vectors. Figure 4.9f shows the correct-sign probability for attached vectors as a function of the true momentum of the underlying Monte Carlo particle, both with and without the secondary vertex constraint. The added lever arm provided by the secondary vertex is essential for reliably reconstructing the charge when the particle's momentum exceeds 2 GeV/c.

4.3.5 Flavor Discrimination

At this point, for each hemisphere there is a list of selected tracks. For hemispheres with no selected secondary vertices the list is empty, otherwise it includes the tracks in the secondary vertices, any cascade tracks which have been attached, and any VXD-alone tracks which have been attached. From this list several signatures can be computed to discriminate between bottom/charm/light event hemispheres. These are the corrected invariant mass of the selected tracks (M_{hem}), the total momentum sum of the selected tracks (P_{hem}), the distance from the IP to the vertex obtained by fitting all of the selected tracks (D_{hem}), and the total number of selected tracks (N_{hem}). Only the last of these uses the VXD-alone tracks.

To calculate M_{hem}, each track is assigned the mass of a charged pion and the invariant mass M_{ch} of the selected tracks is calculated. This mass can be partially corrected for the

Figure 4.9: Distributions of VXD-vector selection variables: (a) T, (b) L, (c) L/D, (d) α, (e) neural network output y_{vec}. A good vector is one which originates from a heavy hadron decay. The arrow indicates the accepted region. The probability to assign the correct charge to a vector based on its fitted curvature is shown in (f), both with and without the secondary vertex as a constraint.

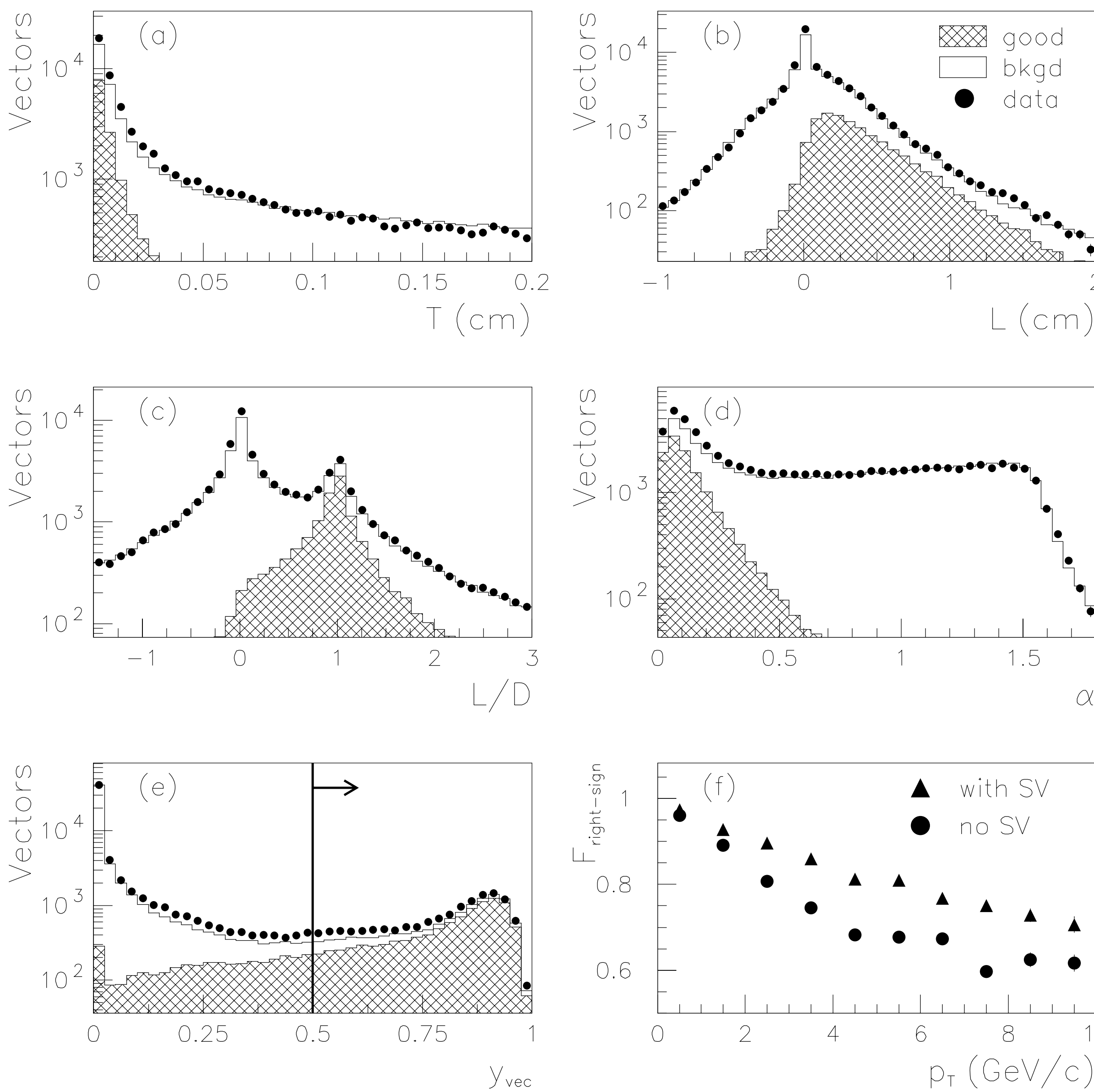

Figure 4.10: Schematic illustration of the missing P_t determination.

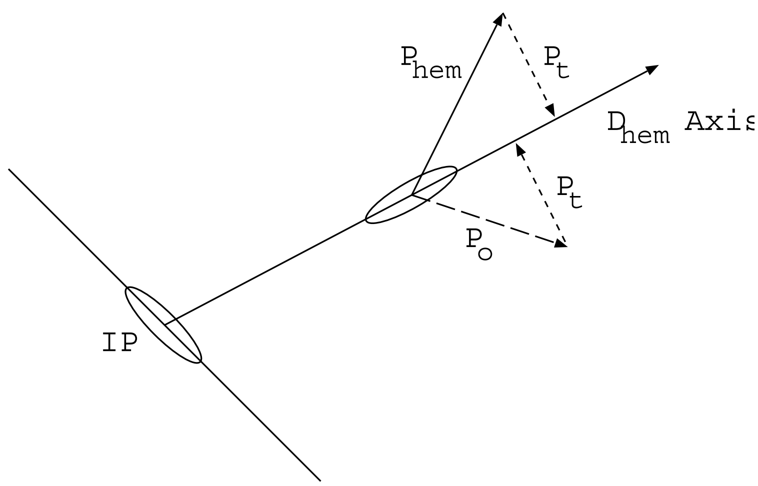

unknown contribution from neutral decay products using the vertex transverse momentum. The minimum amount of momentum P_t required to align the momentum $\vec{P}_{hem}$ with the flight direction $\vec{D}_{hem}$ to within errors is found, as shown in Figure 4.10. The charged mass is then corrected to obtain the P_t-corrected mass M_{hem}:

$$M_{hem} = \sqrt{M_{ch}^2 + P_t^2} + |P_t|. \tag{4.9}$$

The magnitude of P_t is constrained to be $\leq M_{ch}$ to prevent fake vertices from gaining large masses through this correction.

The four signatures given above are used as inputs for a neural network trained to distinguish hemispheres in bottom/charm/light events. The four inputs and the neural network output y_{hem} are shown in Figure 4.11. Also shown in Figure 4.11 is the correlation between P_{hem} and M_{hem} for bottom and charm. This correlation in the low M_{hem} region allows the selection of purer samples of charm than would be possible using M_{hem} alone.

The flavor selection neural network was trained to put charm event hemispheres near $y_{hem} = 0$, bottom event hemispheres near $y_{hem} = 1$, and light-flavor background near $y_{hem} =$

Figure 4.11: Distributions of flavor discrimination variables: (a) M_{hem}, (b) P_{hem}, (c) D_{hem}, (d) N_{hem}, (e) neural network output y_{hem}, (f) P_{hem} vs. M_{hem} correlation.

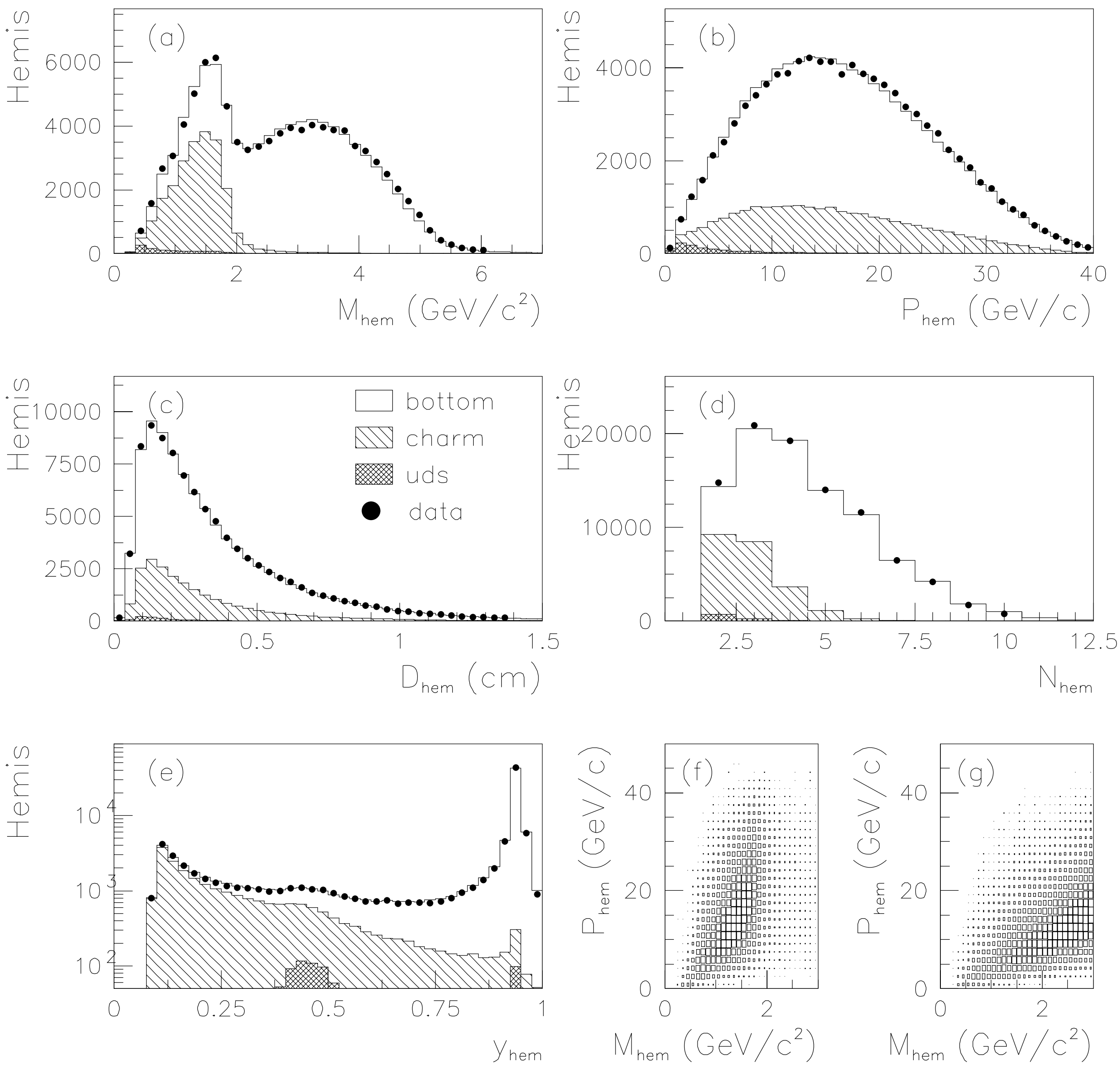

Figure 4.12: Purity vs. efficiency for hemispheres in (a) charm and (b) bottom events, as the selection neural network cut is varied.

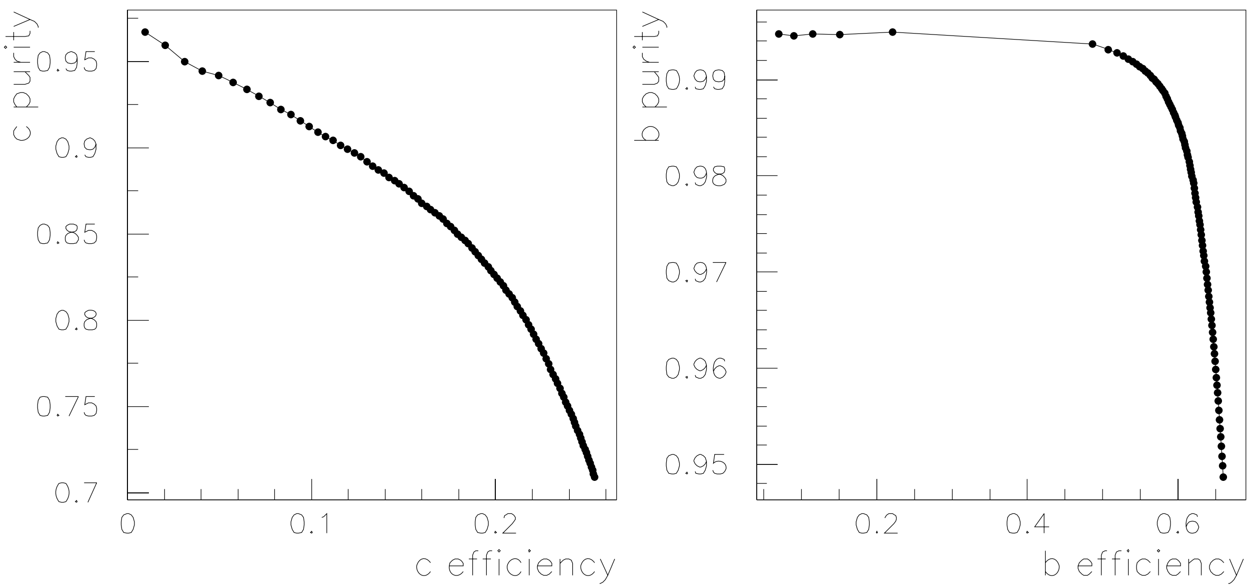

0.5. This allows a simple selection of charm (bottom) event hemispheres by specifying an upper (lower) limit for the output value y_{hem}. Figure 4.12 shows the ranges of purity vs. efficiency which can be obtained for charm and bottom event hemisphere tagging by adjusting only this one cut.

4.4 Quark/Antiquark Discrimination

In order to measure the polar-angle asymmetry of heavy quarks in Z decays, it is necessary not only to select heavy flavor events but also to find the direction of the quark (as opposed to the antiquark). The thrust axis $\pm\hat{t}$ will be used for this purpose, oriented to point into the nominal quark hemisphere. The two methods used to orient $\hat{t}$ for these results are vertex charge and identified kaons.

4.4.1 Vertex Charge

The net charge of the selected tracks in the hemisphere Q_{vtx} (including the attached cascade and VXD-alone tracks) is a good estimate of the charge of the underlying heavy hadron. For charged hadrons a non-zero vertex charge generally reflects the charge of the heavy quark/antiquark, and can be used to orient the thrust axis. For neutral hadrons a non-zero charge results from one or more missing or extra tracks and provides no information, diluting the analyzing power. It is therefore important that neutral hadrons be reconstructed with zero vertex charge to keep them out of the charged sample.

4.4.2 Identified Kaons

A second method used is to identify charged kaons from the heavy hadron decay. These should result from the $c \to s$ and $b \to c \to s$ decays of the heavy hadron and so reflect the charge of the initial heavy quark/antiquark. It is also possible to get charged kaons from fragmentation or from an initial s quark in D_s or B_s mesons, so this method will be subject to physics backgrounds in addition to misidentification. The current knowledge of heavy hadron decays to $K^{\pm}$ according to the Particle Data Group (PDG) [21] is summarized in Table 4.1. The kaons are seen to be an especially good tag for D^0 mesons, where the branching ratio for the $c \to s$ kaons is large and the wrong-sign kaon rate is small. The kaons therefore provide a good complement to Q_{vtx} for c hadrons. For b hadrons the wrong-sign kaon rates are larger, which will decrease the power of the tag as it is not possible to distiguish these from the $b \to c \to s$ kaons. In addition, in the sample with $Q_{vtx} = 0$ where the identified kaons would supplement the vertex charge method the correlation of the kaon charge with the heavy quark charge at production will be substantially diluted by $B^0 - \bar{B}^0$ mixing. For these reasons the charged kaons do not provide significant improvement over Q_{vtx} alone for b hadrons and so will not be used.

Table 4.1: Branching ratios to $K^{\pm}$ from the PDG.

Species	$BR(\rightarrow K^-)$ (%)	$BR(\rightarrow K^+)$ (%)
D^+	24.2±2.8	5.8±1.4
D^0	53±4	3.4±0.6
D_s	13±14	20±18
$B^-/\bar{B}^0$	66±5	13±4

Kaons are identified track-by-track with the CRID using a standard SLD routine [42]. Tracks are first subjected to a set of cuts to ensure that they are well-reconstructed with good CDC hits near the CRID inner wall, and that they are within the CRID acceptance. The appropriate sector of the CRID is checked to verify that the radiators and TPC are operational. An ionization signal in the TPC or a ring in the liquid radiator is required to ensure that the particle passed through the CRID without scattering.

For each of the selected tracks in the hemisphere that pass these cuts, a likelihood is calculated for each of five particle hypotheses: electron, muon, pion, kaon, and proton. These likelihoods are constrained to sum to one. The likelihood function consists of a signal term describing the expected number and radial distribution of Cherenkov photons for a particular hypothesis and a uniform background term, and combines information from both the liquid and gas radiators. To discriminate between the hypotheses the difference in the logarithms of the likelihoods is used. Figure 4.13 shows this difference for $K-\pi$ and K-proton. To select kaons in the data a requirement of $\ln\mathcal{L}_K - \ln\mathcal{L}_\pi > 3$ and $\ln\mathcal{L}_K - \ln\mathcal{L}_p > -1$ is used. For the Monte Carlo the $\ln\mathcal{L}_K - \ln\mathcal{L}_\pi$ cut is varied as a function of momentum to match the pion mis-ID rate in the data, which is measured using a sample of pions from K^0_S and three-prong τ decays [42]. Also shown in Figure 4.13 are the momentum distribution of the selected tracks and the efficiency for a kaon/non-kaon to pass these cuts. The kaon efficiency is lower between 2 and 8 GeV/c because these tracks are above the resolution limit for the liquid radiator and below the kaon Cherenkov threshold for the gas radiator.

Therefore only pion rejection can be done in this region.

To assign a charge to a tagged hemisphere, a kaon charge Q_K is used. This Q_K is calculated as the charge sum of the selected tracks in the hemisphere which pass the likelihood cuts described above.

Distributions of the hemisphere charges Q_{vtx} and Q_K are shown in Figure 4.14, for $y_{hem} < 0.4$ (mostly c), and for $y_{hem} > 0.85$ (mostly b). In the Q_{vtx} plots the Monte Carlo distributions shown are for positive, negative, and neutral heavy hadrons, and for the wrong-flavor background. For the Q_K plots the Monte Carlo distributions are for heavy hadron decays into K^+, K^-, no charged kaons, and wrong-flavor background. Comparing Figures 4.14c and 4.14d, the improvement in Q_{vtx} from the VXD-alone tracks can clearly be seen.

Figure 4.13: Differences in log-likelihood for (a) kaon vs. pion and (b) kaon vs. proton. The arrows indicate the accepted region. The $K-p$ cut has been applied in (b). In (c) is shown the momentum distribution of the accepted tracks, and (d) shows the fraction of K and non-K tracks which are accepted as a function of the track momentum. The points are data and the hatched regions show the Monte Carlo distributions for each particle type.

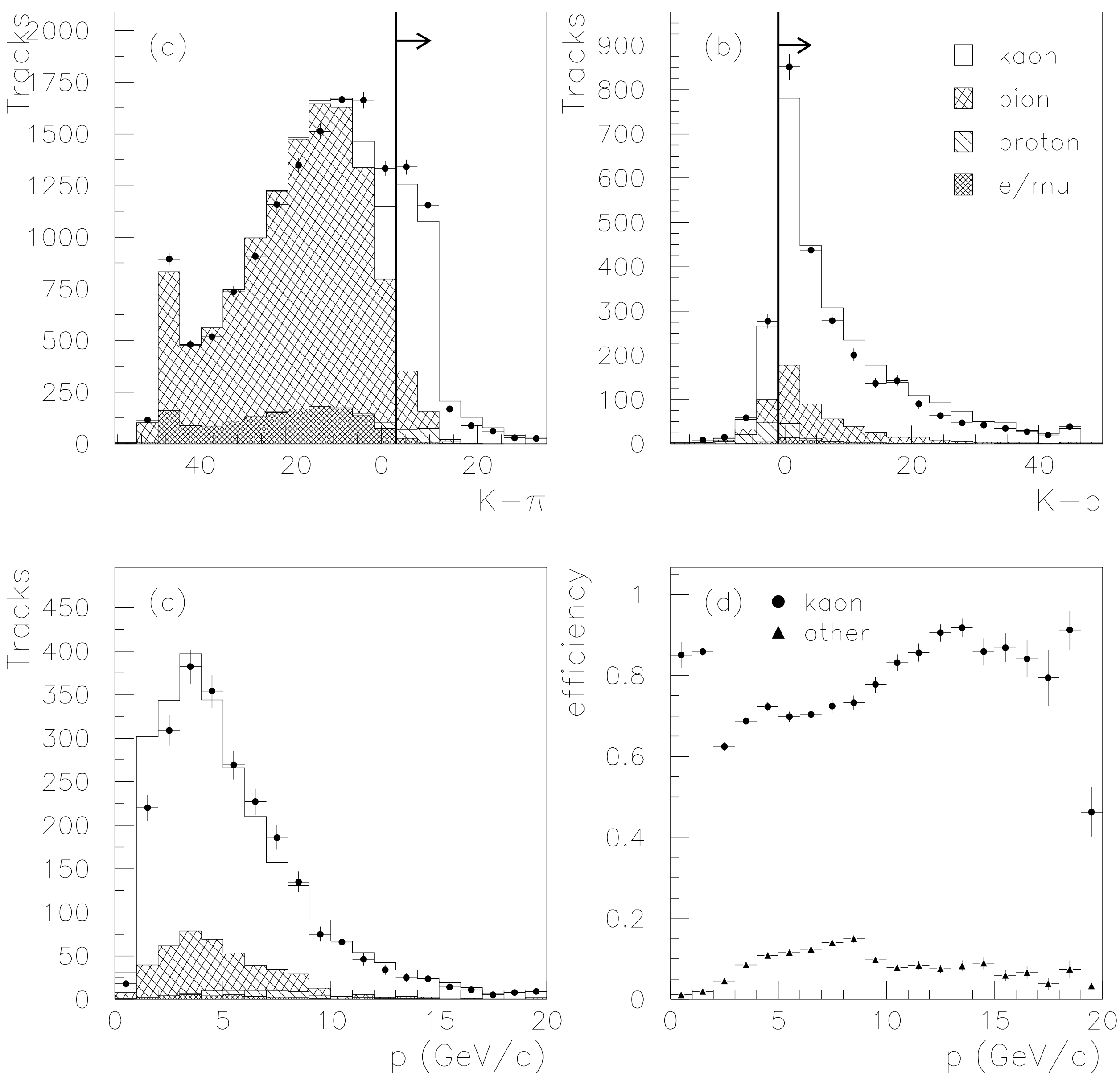

Figure 4.14: Distributions of hemisphere charge: (a) Q_{vtx}, $y_{hem} < 0.4$, (b) Q_K, $y_{hem} < 0.4$, (c) Q_{vtx}, $y_{hem} > 0.85$, without VXD-alone tracks, (d) Q_{vtx}, $y_{hem} > 0.85$, including VXD-alone tracks. Points are data, hatched regions are the indicated components from the Monte Carlo.

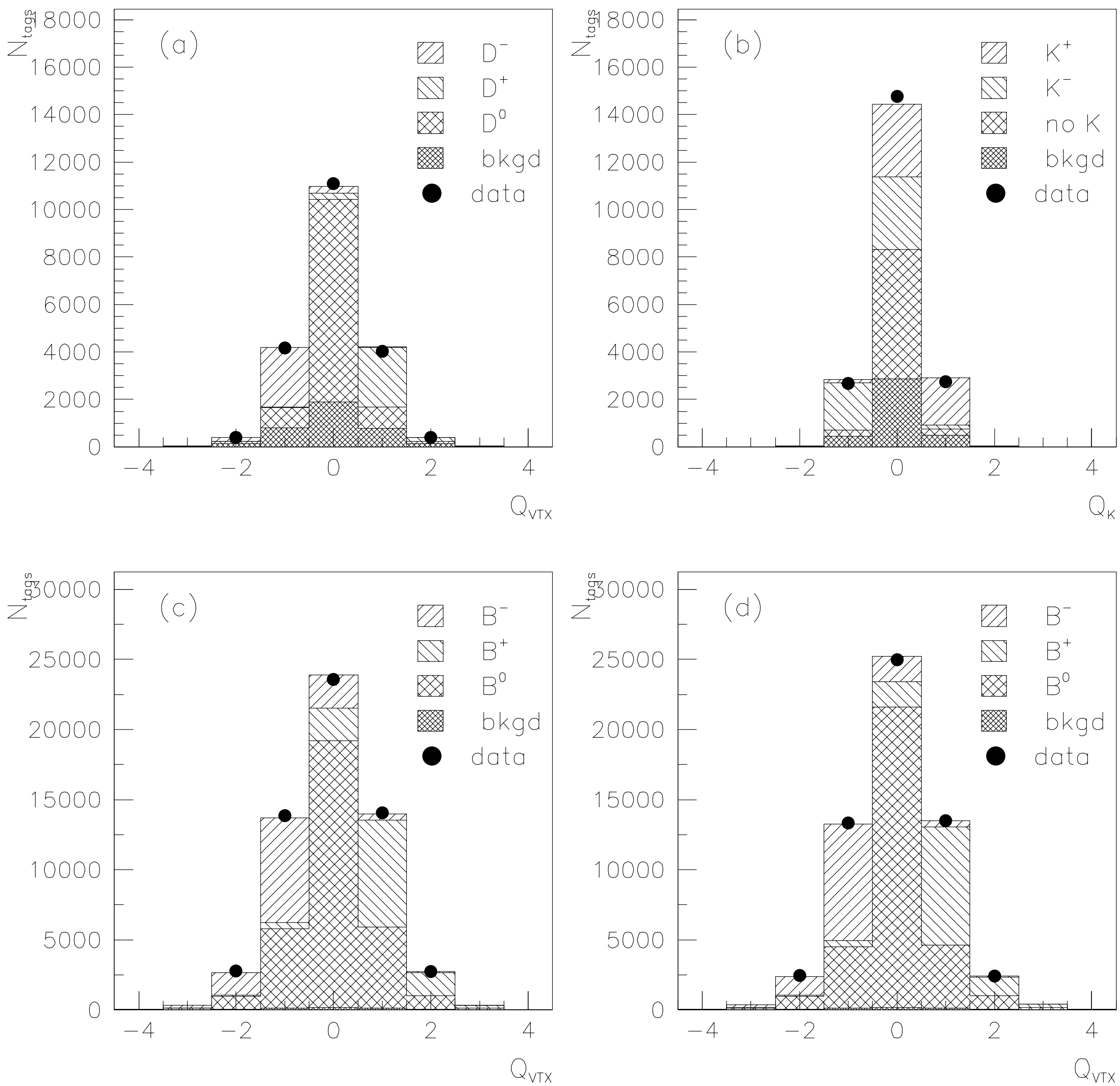

Chapter 5

Asymmetry Analysis

In the previous chapter the techniques for selecting event hemispheres containing heavy hadrons and determining their quark/antiquark nature were described. These techniques will now be applied to measure A_c and A_b using $\tilde{A}^f_{FB}$.

The flavor discrimination neural network output value y_{hem} will be used to define tags which isolate pure samples of charm and bottom event hemispheres. The performance of these tags will be examined, with the expectations from the Monte Carlo simulation compared to an estimation of the tag quality determined from the data.

Beyond selecting a sample of the desired quark flavor, the second necessary ingredient for measuring $\tilde{A}^f_{FB}$ is to construct an estimate for the quark direction. For this analysis the signed thrust axis $\hat{t}_s = \pm\hat{t}$ will be used. The sign is chosen to make $\hat{t}_s$ point into the hemisphere of the event thought to contain the heavy quark, using the information from Q_{vtx} and Q_K. The fraction of hemispheres for which this assignment is correctly made can also be constrained directly from data.

Once the tags have been understood, maximum-likelihood fits are performed to extract A_c and A_b from the samples of selected events.

5.1 Tag Definitions

Using the flavor discrimination neural network output variable y_{hem} described in the previous chapter two tags are defined, one to select charm event hemispheres (the L tag, for "Low-mass"), and the other for bottom event hemispheres (the H tag, for "High-mass"). In addition to flavor selection, these tags must indicate whether a hemisphere contains a heavy quark or antiquark. This is done using a tag charge Q_{tag}, defined below for the two tags, which combines the Q_{vtx} and Q_K information. For convenience Q_{tag} is defined so that a correctly-tagged quark hemisphere will result in $Q_{tag} > 0$. Only the sign of Q_{tag} will be used, not its magnitude.

The L tag, optimized to select charm event hemispheres, uses a cut of $y_{hem} < 0.4$. An additional requirement of $P_{hem} > 5$ GeV/c is imposed to improve the light-flavor rejection. The tag charge Q_{tag} for the L tag is defined as $Q_{tag} = Q_{vtx} - Q_K$. The kaon charge Q_K is subtracted rather than added because the K from a $c \to s$ decay will be negative, opposite to the charge of the c quark. If both Q_{vtx} and Q_K are zero, or if they are in disagreement ($Q_{vtx} \times Q_K > 0$), the hemisphere is not used.

The H tag, optimized to select bottom event hemispheres, uses a cut of $y_{hem} > 0.85$. Tags with $M_{hem} > 7$ GeV/c^2 are rejected due to poor charge reconstruction. The tag charge is defined as $Q_{tag} = -Q_{vtx}$, with the minus sign accounting for the negative charge of b quarks to make Q_{tag} correspond to the convention defined above. Hemispheres with $Q_{vtx} = 0$ are not used.

The cuts and Q_{tag} assignments for the L and H tags are summarized in Table 5.1.

Table 5.1: Cuts for the L and H tags. Both tags also require $Q_{tag} \neq 0$.

tag	cuts	Q_{tag}
L	$y_{hem} < 0.4$	$Q_{vtx} - Q_K$
	$P_{hem} > 5$ GeV/c	
	$Q_{vtx} \times Q_K \leq 0$	
H	$y_{hem} > 0.85$	$-Q_{vtx}$
	$M_{hem} < 7$ GeV/c^2	

5.2 Tag Performance

The efficiency for a tag to select a hemisphere in an event of flavor f, represented by ϵ^t_f, is defined as:

$$\epsilon^t_f = \frac{N^t_f}{2N_f} \tag{5.1}$$

where t is the tag type (either L or H), N^t_f is the number of hemispheres in events of flavor f tagged as type t, and N_f is the total number of events of flavor f (two hemispheres per event). The N_f are related to the hadronic partial widths R_f by $N_f = R_f N_{tot}$, where N_{tot} is the total number of selected hadronic decays. For this analysis the Standard Model values (0.6120, 0.1722, 0.2158) will be used for (R_{uds}, R_c, R_b). The tag efficiency ϵ^t_f is therefore the probability for a hemisphere in an event of flavor f to be tagged as t.

The flavor purity of a tag, defined as:

$$\pi^t_f = \frac{\epsilon^t_f R_f}{\sum_g \epsilon^t_g R_g} \tag{5.2}$$

expresses how well a tag t isolates the flavor f. The hadronic partial widths must be included to reflect the differing initial populations of the various flavors.

The last measure of the tag quality is the correct-sign probability p^t_f, which expresses how often the quark/antiquark assignment is correctly made. Because QCD radiation can cause

Table 5.2: Total efficiency, flavor purity, and correct-charge probability for the L and H tags.

tag	flavor	ϵ_f^t	π_f^t	p_f^t
L	uds	0.001	0.023	0.414
L	c	0.121	0.809	0.926
L	b	0.020	0.168	0.545
H	uds	0,001	0.005	0.515
H	c	0.005	0.011	0.303
H	b	0.323	0.984	0.805

both the quark and the antiquark to lie in the same hemisphere, defining p_f^t by comparing the observed Q_{tag} to the heavy quark charge in that hemisphere is subject to ambiguity. A method which considers the entire event configuration is used to avoid this problem.

To determine if a tag is correct-sign, first the event thrust vector $\hat{t}$ found from calorimeter clusters is oriented using the tag charge so that it points into the nominal quark hemisphere. If $Q_{tag} > 0$ for the hemisphere $\hat{t}$ is signed so that it points into that hemisphere, while if $Q_{tag} < 0$ that hemisphere is thought to contain the antiquark, so $\hat{t}$ is made to point out of that hemisphere into the other. This signed thrust vector $\hat{t}_s$ is now compared with the thrust vector $\hat{t}_{parton}$ found from the Monte Carlo partons, signed so that it points along the direction of the primary quark after parton showering. A correct-sign tag is then defined as one where $\hat{t}_s \cdot \hat{t}_{parton} > 0$. The parton thrust vector is used because it is the quantity for which QCD corrections have been calculated [43] which most closely approximates the observable $\hat{t}$.

The tag quality parameters ϵ_f^t, π_f^t, and p_f^t for both tags are summarized in Table 5.2.

5.3 Asymmetry Fits

The asymmetry parameters A_c and A_b are found using a maximum-likelihood fit to the signed thrust-axis distributions. This is equivalent to constructing $\tilde{A}_{FB}^f(\cos\theta)$ and fitting for A_f, but has the advantage of not requiring any binning of the events. For a likelihood function the polarized cross section formula given in Equation 1.20 is used:

$$\mathcal{L} \sim (1 - A_e P_e)(1 + \cos^2\theta) + 2(A_e - P_e)A_{eff}\cos\theta \tag{5.3}$$

where A_e is the intial-state Ze^+e^- asymmetry, P_e is the electron beam polarization (signed so that $P_e > 0$ for right-handed electrons), $\cos\theta$ is the polar angle of the signed thrust axis, and A_{eff} is the effective asymmetry. The effective asymmetry can be written as a sum of contributions from each event flavor present in the sample:

$$A_{eff} = \sum_f \Pi_f(2P_f - 1)(1 - C_f^{QCD})(A_f - \delta_f^{QED}) \tag{5.4}$$

where A_f is the Born-level asymmetry for flavor f, Π_f is the fraction of that flavor in the sample, P_f is the correct-sign probability for an event of flavor f, C_f^{QCD} is a correction for QCD radiation, and δ_f^{QED} is a correction for QED effects. The event correct-sign probability enters as $(2P_f - 1)$ to convert this probability into an asymmetry, which accounts for the dilution of the observed effective asymmetry caused by events with the thrust axis signed incorrectly.

Because the tagged event sample splits naturally into subsamples which are predominantly c or b, separate fits are performed on these two subsamples for A_c and A_b respectively. Events with only a single L tag or with two L tags will be used to determine A_c, while events with only a single H tag, one L and one H tag, or two H tags will be used in the A_b fit. In the case of the double-L-tagged and double-H-tagged events those with same-sign Q_{tag} values will not be used, as there is no way to orient the thrust axis. For the mixed-LH-tag events the Q_{tag} value for the L-tagged hemisphere is ignored, and only the sign of the H-tagged hemisphere is used.

While it is a simple matter to determine Π_f and P_f from the Monte Carlo, there are significant uncertainties involved. In addition to dependences on the details of heavy hadron production and decay, these parameters are also sensitive to detector effects such as tracking efficiency and resolution. Therefore, it is highly desirable to constrain these parameters from the data as much as possible using a calibration procedure to minimize the systematic errors. This calibration procedure will also fix the central values of Π_f and P_f, which could otherwise be manipulated to produce a favored result. In this way the tag calibration procedure serves a similar purpose as doing a blind analysis. The results of the calibration needed for the A_c and A_b likelihood fits will be presented below. Full details of the procedure are given in Appendix A.

It is statistically advantageous to calculate separate values of Π_f and P_f for single-tagged and double-tagged events, to add more information to the likelihood function. In the A_b sample, the mixed-LH-tagged events are considered to be single-tagged for this purpose, since the L-tag doesn't contribute any useful information about the event. A superscripted s or d will be used to indicate whether a given Π_f or P_f refers to single-tagged or double-tagged events. In the maximum likelihood fit the appropriate values will be used on an event-by-event basis depending on the combination of tags in each event.

Because the antisymmetric term is a function of $\cos\theta$, all of the events do not have equal weight in the fit. Events at larger $\cos\theta$ have a larger raw asymmetry, and therefore contribute more statistical power than the more central events. For this reason Π_f and P_f must be parameterized as functions of $\cos\theta$. The tagging quality is generally worse at large polar angle, so the average values of Π_f and P_f will be too high for the large-$\cos\theta$ events. If the events had equal weights this effect would be exactly compensated by correspondingly low values for the central events, but because of the unequal weighting this is not the case.

A shape factor derived from the Monte Carlo is applied to each:

$$\Pi_f(\cos\theta) = \left(\frac{\Pi_f^{MC}(\cos\theta)}{\Pi_f^{MC}}\right)\Pi_f \tag{5.5}$$

$$P_f(\cos\theta) = \left(\frac{P_f^{MC}(\cos\theta)}{P_f^{MC}}\right)P_f \tag{5.6}$$

where $\Pi_f^{MC}(\cos\theta)$ and $P_f^{MC}(\cos\theta)$ refer to the Monte Carlo purity and correct-sign probability for a particular value of $\cos\theta$. These are found by binning the Monte Carlo in $\cos\theta$ and calculating the quantity in each bin. Dividing by the average values over all $\cos\theta$ Π_f^{MC} and P_f^{MC}, the resulting scale functions are used to correct the calibrated average values Π_f and P_f. These scale functions for each type of tagged event will be shown later in this chapter for each fit.

The asymmetries caused by parity violation in Z decay are diluted by QCD radiation. The event tagging and fitting procedure tends to be biased against events with hard gluon radiation, however, and these biases are in general different for the different analysis techniques. In order for the measurements to be comparable, therefore, either the QCD effects must be removed or a correction must be made for the bias. The convention is to remove the QCD effects and report the Born-level asymmetry A_f.

The procedure used is that described in [44]. The theoretical $\mathcal{O}(\alpha_s^2)$ calculations are used for the total corrections, while the analysis-related biases are determined from the full JETSET parton-shower Monte Carlo. The theoretical corrections C_f^{theory} for the hadron-level thrust axis are evaulated in [45] as 4.13% (3.54%) for c (b) events, using the calculation in [43]. These include corrections of -0.35% (-0.23%) for hadronization effects, determined from the JETSET Monte Carlo. The results presented here use the parton-level thrust axis, so these are removed to obtain corrections of 4.48% (3.77%).

The biased correction C_f^{QCD} is constructed by scaling the full correction by a factor s_f, so that $C_f^{QCD} = s_f C_f^{theory}$. The factor s_f is found from:

$$s_f = \frac{A_f - A_f^{fit}}{A_f - A_f^{PS}} \tag{5.7}$$

where A_f is the Born-level asymmetry in the Monte Carlo, A_f^{PS} is the parton-level thrust axis asymmetry generated by JETSET, and A_f^{fit} is the asymmetry obtained by fitting the Monte Carlo using the full analysis procedure. Values of $s_c = 0.27 \pm 0.13$ and $s_b = 0.53 \pm 0.08$ were found, where the errors are due only to Monte Carlo statistics. A large part of the bias comes from the event thrust $T > 0.8$ cut, with the rest due to tagging and thrust-axis signing. Another effect included in s_f is the $\cos\theta$ dependence of the corrections C_f^{theory}. Because the effect is small and there are limited Monte Carlo statistics this dependence is absorbed into the overall s_f rather than parameterizing s_f and C_f^{theory} as functions of $\cos\theta$.

The QCD corrections are determined only for the signal flavors, c for A_c and b for A_b. No QCD corrections are applied to the background asymmetries in either fit, since the effects are expected to be very small.

The δ_f^{QED} terms contain corrections to the heavy quark asymmetries for initial-state QED radiation and γ/Z interference. These effects are removed by convention so that Born-level results are reported. The values of δ_f^{QED}, obtained from calculations using ZFITTER [46], are $\delta_c^{QED} = 0.0012$ and $\delta_b^{QED} = -0.0021$. These corrections are also only applied to the signal flavors.

5.3.1 A_c Fit

For the A_c fit, the single-L-tagged events and double-L-tagged events are used, discarding the same-sign Q_{tag} double-tagged events. The signed thrust axis distributions, for left- and right-handed electron beams, are shown for these events in Figure 5.1. In both cases clear forward-backward asymmetries are visible. There are more events for the left-handed

Figure 5.1: Signed thrust-axis distributions of the events in the A_c fit, for (a) $P_e < 0$ and (b) $P_e > 0$. The histograms show the Monte Carlo expectation for $A_c = 0.667$.

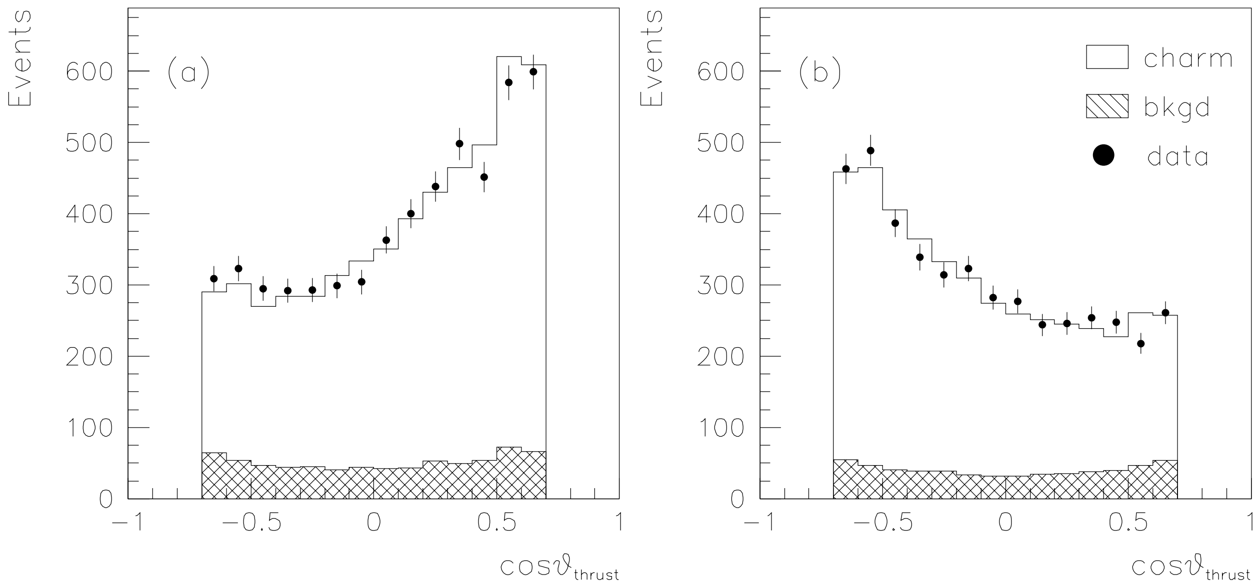

electron beam because of the initial-state coupling asymmetry A_e.

The likelihood function used is:

$$\begin{aligned}\mathcal{L} \;\sim\;& (1 - A_e P_e)(1 + \cos^2\theta) + 2(A_e - P_e)\cos\theta\{ \\ & \Pi_c(2P_c - 1)(1 - C_c^{QCD})(A_c - \delta_c^{QED}) \\ & \Pi_b(2P_b - 1)A_b + \Pi_{uds}A_{uds}^{raw}\} \end{aligned} \tag{5.8}$$

where the QCD and QED corrections are applied only to the signal flavor c. The Standard Model value of 0.935 is used for A_b, and the raw asymmetry of the uds background A_{uds}^{raw} is set to zero for the fit but will be varied to estimate a systematic error.

The calibrated values of Π_f^s and Π_f^d are shown in Table 5.3, and of P_f^s and P_f^d in Table 5.4. Also shown in both cases are the Monte Carlo expectations. The calibrated values will be used in the likelihood fit, with either the single-tag or double-tag values chosen event-by-event.

Table 5.3: Single-tag and double-tag purities Π_f^s and Π_f^d used in the A_c fit. The quoted errors are due only to the statistical uncertainties of the calibrated quantities. Also shown are the Monte Carlo expectations.

flavor	MC Π_f^s	calibrated Π_f^s	MC Π_f^d	calibrated Π_f^d
c	0.8519	0.8355±0.0058	0.9810	0.9751±0.0025
b	0.1312	0.1470±0.0058	0.0190	0.0249±0.0025
uds	0.0169	0.0175	0	0

Table 5.4: Single-tag and double-tag correct-sign probabilities P_f^s and P_f^d used in the A_c fit. The quoted errors are due only to the statistical uncertainties of the calibrated quantities. Also shown are the Monte Carlo expectations.

flavor	MC P_f^s	calibrated P_f^s	MC P_f^d	calibrated P_f^d
c	0.9251	0.9117±0.0097	0.9946	0.9921±0.0021
b	0.548	0.543±0.032	0.610	0.586±0.063

The polar-angle shape corrections to Π_f and P_f discussed above are shown in Figure 5.2. As expected, both the purity and the correct-sign probability for c events decrease at large polar angles. Not including these shapes would incorrectly lower the measured value of A_c by 0.9%

The sample selected for the A_c fit consists of a total of 9970 events. The likelihood fit to the signed $\cos\theta$ distributions yields:

$$A_c = 0.673 \pm 0.029 \tag{5.9}$$

where the error is statistical only.

5.3.2 A_b Fit

For the A_b fit the single-H-tagged events, the mixed-LH-tagged events, and the double-H-tagged events are used, discarding the same-sign Q_{tag} double-H-tagged events and the L-tag information in the mixed-tagged events. The signed thrust axis distributions, for left- and

Figure 5.2: Polar angle shape corrections to the average (a) Π_f^s, (b) Π_f^d, (c) P_f^s, and (d) P_f^d for the A_c fit. The widths of the bands reflect the uncertainties due to Monte Carlo statistics.

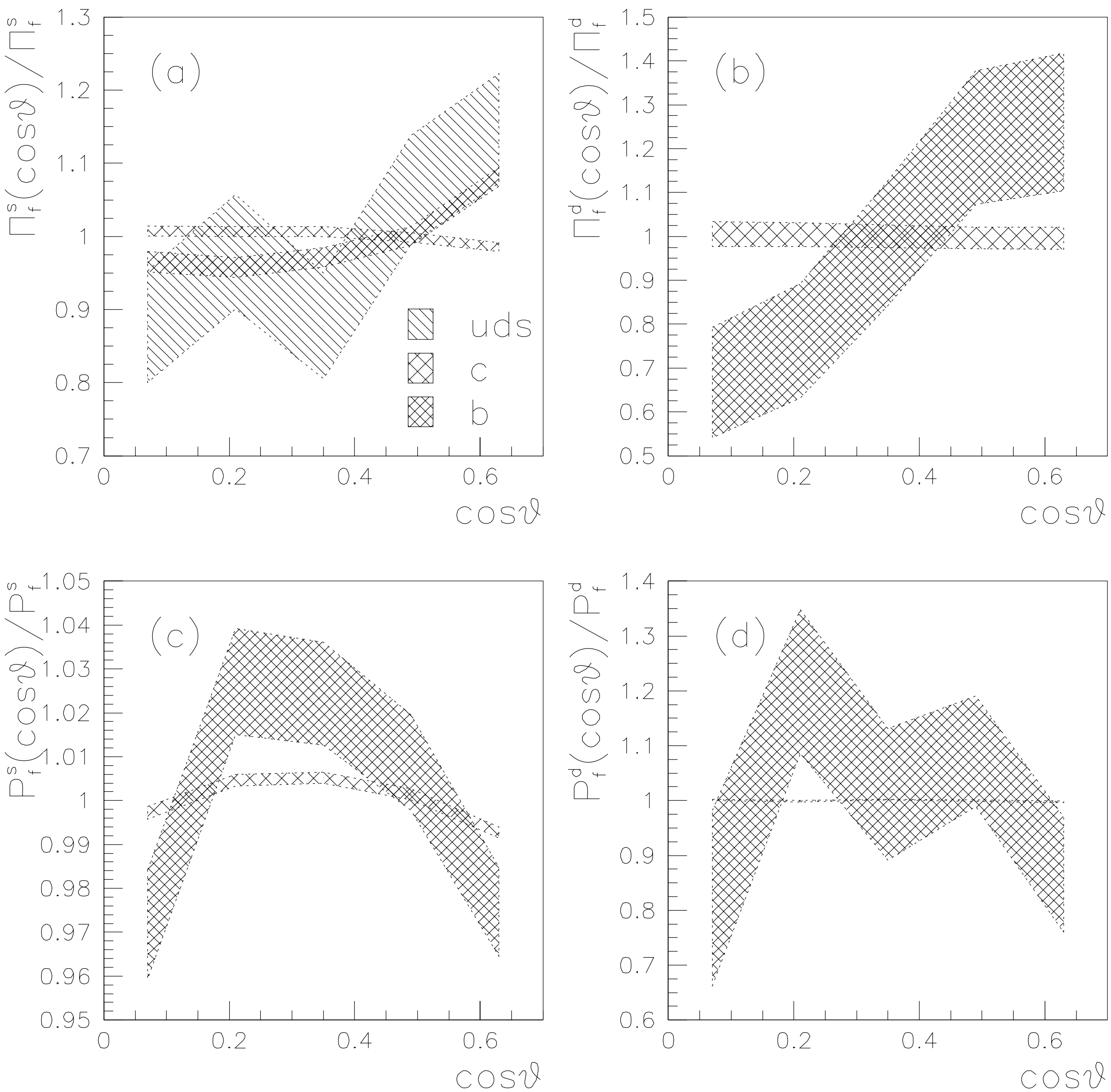

Figure 5.3: Signed thrust-axis distributions of the events in the A_b fit, for (a) $P_e < 0$ and (b) $P_e > 0$. The histograms show the Monte Carlo expectation for $A_b = 0.935$.

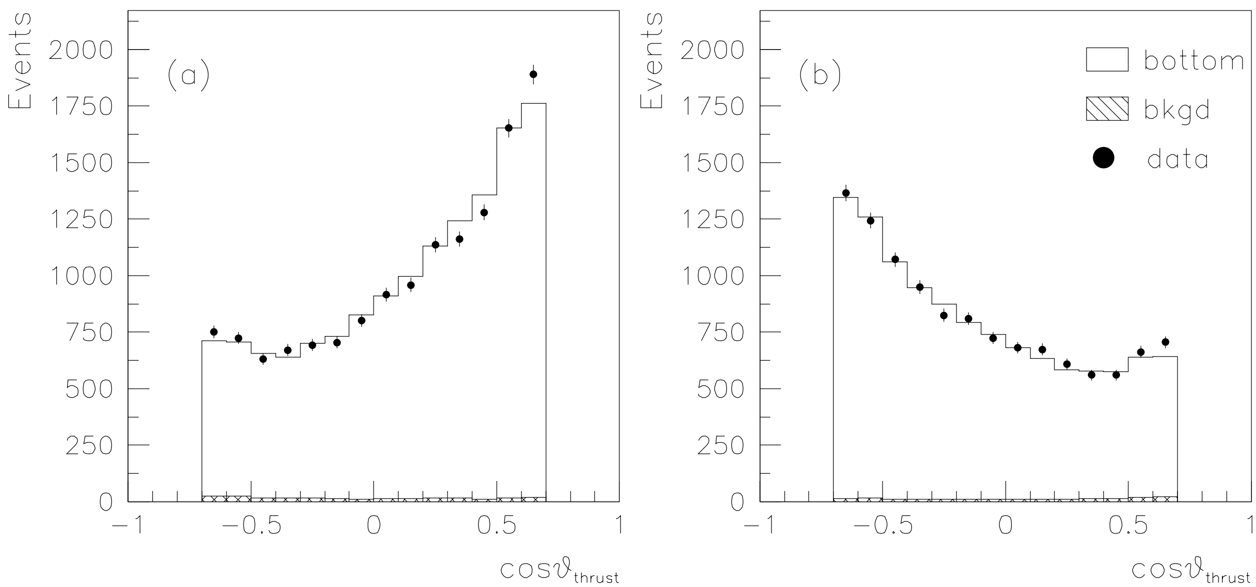

right-handed electron beams, are shown for these events in Figure 5.3.

The likelihood function used is:

$$\begin{aligned}\mathcal{L} \sim\ & (1 - A_e P_e)(1 + \cos^2\theta) + 2(A_e - P_e)\cos\theta\{ \\ & \Pi_b(2P_b - 1)(1 - C_b^{QCD})(A_b - \delta_b^{QED}) \\ & \Pi_c(2P_c - 1)A_c + \Pi_{uds}A_{uds}^{raw}\}\end{aligned} \tag{5.10}$$

where the QCD and QED corrections are applied only to the signal flavor b. The Standard Model value of 0.667 is used for A_c, and the raw asymmetry of the uds background A_{uds}^{raw} is set to zero for the fit but will be varied to estimate a systematic error.

The calibrated values of Π_f^s and Π_f^d are shown in Table 5.5, and of P_f^s and P_f^d in Table 5.6. Also shown in both cases are the Monte Carlo expectations. The values of P_c are a special case, in that they are not calibrated from the data but rather constrained through other means as described in Appendix A. The calibrated values will be used in the likelihood fit,

Table 5.5: Single-tag and double-tag purities Π_f^s and Π_f^d used in the A_b fit. The quoted errors are due only to the statistical uncertainty of the calibrated efficiencies. Also shown are the Monte Carlo expectations.

flavor	MC Π_f^s	calibrated Π_f^s	MC Π_f^d	calibrated Π_f^d
b	0.9764	0.9724±0.0071	0.9999	0.9998±0.0002
c	0.0169	0.0210±0.0071	0.0001	0.0002±0.0002
uds	0.0067	0.0066	0	0

Table 5.6: Single-tag and double-tag correct-sign probabilities P_f^s and P_f^d used in the A_b fit. The quoted errors are due only to the statistical uncertainty of the calibrated probabilities. Also shown are the Monte Carlo expectations.

flavor	MC P_f^s	calibrated P_f^s	MC P_f^d	calibrated P_f^d
b	0.8033	0.8168±0.0049	0.9459	0.9545±0.0029
c	0.303	0.25	0.086	0.10

with either the single-tag or double-tag values chosen event-by-event.

The polar-angle shape corrections to Π_f and P_f are shown in Figure 5.4. For the double-tagged events the Monte Carlo statistics are insufficient to determine shapes for the c background, so the average values of Π_c^d and P_c^d are used for all $\cos\theta$. Not including these shapes would incorrectly lower the measured value of A_b by 1.6%

The sample selected for the A_b fit consists of a total of 25917 events. The likelihood fit to the signed $\cos\theta$ distributions yields:

$$A_b = 0.919 \pm 0.018 \tag{5.11}$$

where the error is statistical only.

Figure 5.4: Polar angle shape corrections to the average (a) Π_f^s, (b) Π_f^d, (c) P_f^s, and (d) P_f^d for the A_b fit. The widths of the bands reflect the uncertainties due to Monte Carlo statistics.

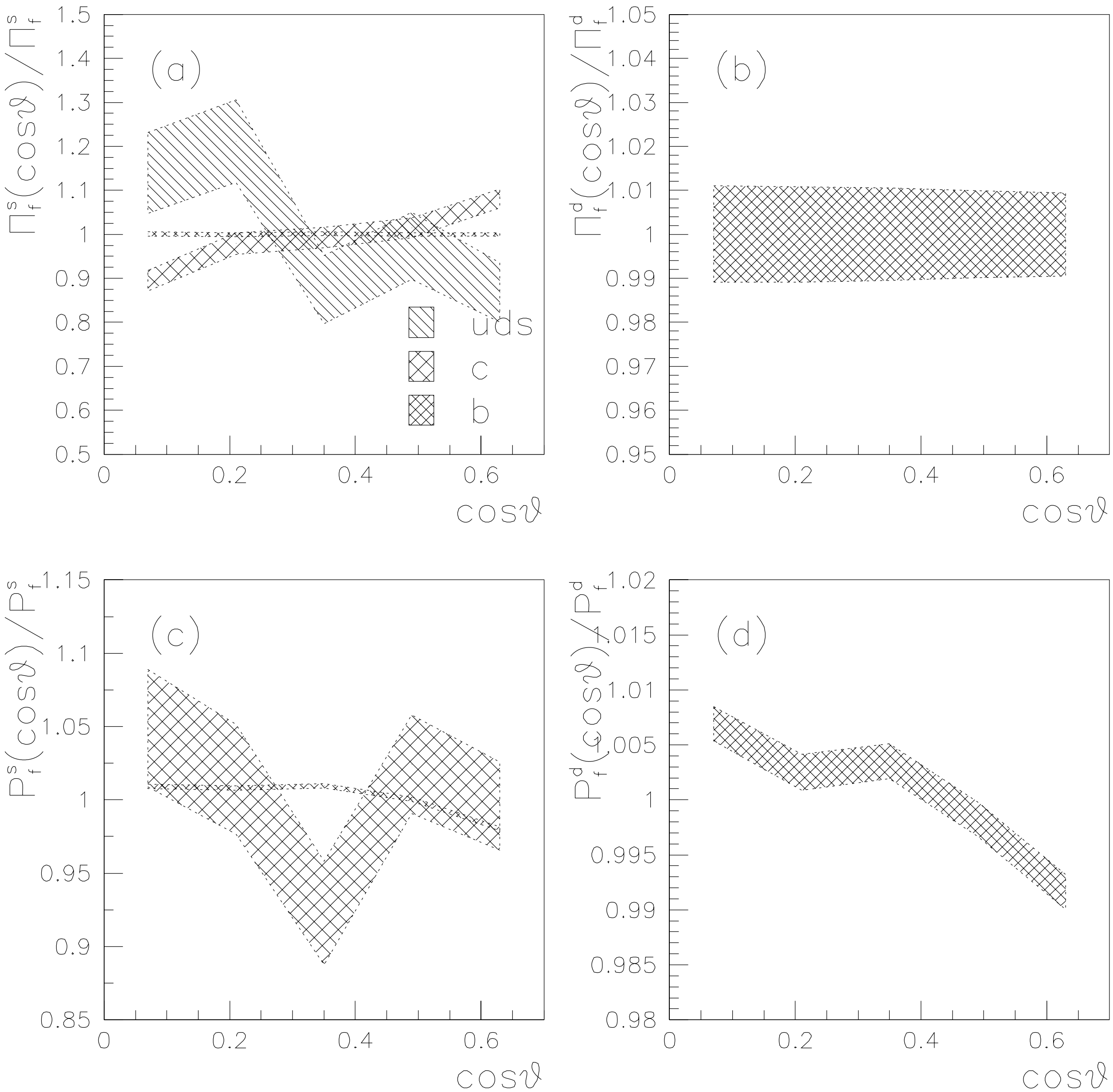

5.4 Systematic Errors

A variety of sources of systematic error have been considered. The sources along with the resulting variations in A_c and A_b are summarized in Table 5.7. Although multiple sources have been investigated, the total systematic uncertainty is dominated by the uncertainty on P_f obtained from the calibration procedure. A brief description of each source follows.

5.4.1 Calibration Statistics

The calibration statistics category includes the uncertainties due to the statistical errors on P_f and Π_f obtained from the calibration procedure. These uncertainties are essentially uncorrelated between A_c and A_b.

5.4.2 Electroweak Parameters

These results depend upon other parameters of the electroweak Standard Model, namely R_c and R_b. In addition values of A_c and A_b are needed for the A_b and A_c fits, respectively. The values and variations used are shown in Table 5.7, along with the changes in A_c and A_b. The Standard Model values were used with variations determined by the precision of the combined LEP results, to avoid correlations with other SLD measurements which are made using essentially the same tagged hemispheres as these results.

For the initial-state asymmetry A_e where there is no Standard Model prediction a variation consistent with the SLD and LEP leptonic measurements was applied and found to have no effect, as expected for $\tilde{A}^f_{FB}$.

Table 5.7: Systematic errors for the A_c and A_b measurements.

source	variation	$\delta A_c/A_c$ (%)	$\delta A_b/A_b$ (%)
Calibration statistics			
P_f	data statistics	2.96	1.41
Π_f	data statistics	0.68	0.63
Electroweak parameters			
R_c	0.1722±0.0048	0.28	0.11
R_b	0.2158±0.0008	0.30	0.29
A_c	0.667±0.035	0.00	0.05
A_b	0.935±0.035	0.10	0.00
Detector modeling			
tracking efficiency	remove correction	0.36	0.34
tracking resolution	remove correction	0.49	0.04
CRID π mid-ID	data $\pm 1\sigma$	0.12	0.00
QCD correction			
C_f^{theory}	±0.0063	0.18	0.35
s_f	±0.13, ±0.08	0.59	0.31
Backgrounds			
p_c^H	0.25±0.14	0.83	0.56
$g \rightarrow c\bar{c}$	2.96±0.38%	0.22	0.01
$g \rightarrow b\bar{b}$	0.254±0.051%	0.06	0.02
non-$g \rightarrow Q\bar{Q}$ ϵ_{uds}	±25%	0.13	0.01
non-$g \rightarrow Q\bar{Q}$ A_{uds}^{raw}	±0.6	0.43	0.09
Tagging correlations			
same-hemisphere $c\bar{c}$	2.82±1.13%	0.33	0.01
same-hemisphere $b\bar{b}$	2.45±0.74%	0.04	0.21
c energy correlation	1.4±2.6%	0.48	0.14
b energy correlation	1.4±0.3%	0.07	0.10
Other			
Beam polarization	±0.5%	0.50	0.50
MC statistics	$\pm 1\sigma$	0.64	0.34
Total		3.48	1.89

5.4.3 Detector Modeling

The uncertainties due to tracking efficiency and tracking resolution were determined by removing the corrections described in Chapter 3. The full difference was taken as the systematic error in each case. The small error for tracking efficiency demonstates the benefit of calibration, for if P_f were taken from the simulation the tracking efficiency correction would be a 3% effect for A_b.

A described in Section 4.4.2, the kaon identification cuts used for the Monte Carlo are different than those used for the data. These differences are tuned to reproduce the rate of pion misidentification observed in pion samples selected in the data using K_S^0 and three-prong τ decays. To estimate the uncertainty the Monte Carlo cut adjustments were varied through a range consistent with the statistical errors on the data pion samples.

5.4.4 QCD correction

The systematic error for the QCD correction has two components. The first is the uncertainty on the theoretical correction itself. This has been estimated in [45], taking into account uncertainties in α_s, quark masses, and missing higher-order terms. An uncertainty of ± 0.0063 is used for both C_c^{theory} and C_b^{theory}. The second component comes from the scale factors s_f. This uncertainty is due solely to Monte Carlo statistics.

5.4.5 Backgrounds

The most significant background-related systematic error is due to the correct-sign probability p_c^H of the charm background under the H tag. As discussed in Appendix A p_c^H can be constrained uniformly in $[0, 0.5]$, equivalent to 0.25 ± 0.14 which is the variation used to estimate the systematic errors.

The *uds* background has two components. The most important is gluons which are far enough off-shell to decay into $c\bar{c}$ or $b\bar{b}$ pairs. The rates suggested by the LEWWG in [47] are used, which indicate a $g \to c\bar{c}(b\bar{b})$ pair in 2.96±0.38%(0.254±0.051%) of hadronic events. The SLD Monte Carlo was reweighted to these central values, and the variations used to set the systematic errors. The simulation indicates that the $g \to Q\bar{Q}$ $(Q = c, b)$ process accounts for 81%(88%) of the uds background under the $L(H)$ tag.

The other component is fake secondary vertices, containing misrecontructed and/or strange particle decay tracks. To check the simulation a sample of hemispheres enriched in uds fakes was selected in both the Monte Carlo and the data. The cuts are $M_{hem} < 2$ GeV/c^2, $P_{hem} < 4$ GeV/c, and no secondary vertex in the opposite hemisphere. The Monte Carlo M_{hem} distributions for true heavy flavor and fakes were normalized to the same number of hadronic events as the data. A fit was then performed to the data M_{hem} distribution for a scale factor for the Monte Carlo fake vertex contribution. The fitted Monte Carlo and data distributions are shown in Figure 5.5. The best-fit scale factor for the Monte Carlo fake level is 1.14±0.08. Based upon this, the Monte Carlo level was used, and a conservative variation of ±25% was applied to cover extrapolation of this constraint to regions of higher M_{hem} and P_{hem}.

The asymmetry of the uds background from $g \to Q\bar{Q}$ was assumed to be zero, since the directions of the resulting hadrons are uncorrelated with the polarization of the Z. No such argument can be made for the fake-vertex background. High-momentum tracks are needed to pass the L or H tag cuts, so leading-particle effects could produce an asymmetry. For the L tag, charged kaons attached to the fake vertex could also exhibit an asymmetry. No such effects are seen in the SLD Monte Carlo, but since the level of this background is low a simple argument can be used to set a conservative variation. The raw asymmetry A_{uds}^{raw} for the fake-vertex part of the uds background was assumed to be uniformly distributed in the interval $[-1, +1]$. The variance was then computed as $[(+1) - (-1)]/\sqrt{12}$, or equivalently $A_{uds}^{raw} = 0.0 \pm 0.6$. The effective asymmetry for the fake-vertex background contribution was

Figure 5.5: Distribution of M_{hem} in the uds-enriched sample.

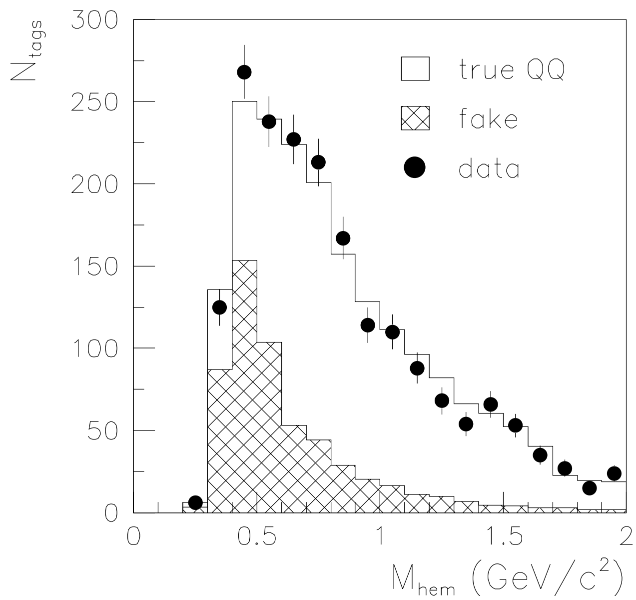

varied through this range to set systematic errors for A_c and A_b.

5.4.6 Tagging Correlations

These uncertainties are related to the sources of the tagging correlations and single/double correct-sign probability corrections used in Appendix A. The variations are constrained by the data as described in Appendix B.

5.4.7 Heavy Hadron Physics

A variety of simulation parameters related to the physics of heavy hadrons were varied and found to have negligible effect, due to the calibration of the tags from the data. These included the hadron lifetimes, energy spectra, production fractions of the different hadron species, and hadron decay charged particle multiplicities according to the prescriptions given in [48]. Also varied were the branching rates of the hadron species into charged kaons according to the values listed in [21], again with negligible effect on A_c and A_b.

5.5 Full Results

The full results, including both statistical and systematic errors, are:

$$A_c = 0.673 \pm 0.029_{stat} \pm 0.023_{syst} \quad (5.12)$$

$$A_b = 0.919 \pm 0.018_{stat} \pm 0.017_{syst} \quad (5.13)$$

with a total uncertainty on $A_c(A_b)$ of 5.5%(2.7%).

Chapter 6

Conclusion

Besides the work presented in this Thesis, the SLD experiment has made measurements of A_c and A_b using other techniques which are discussed briefly below. The current status of A_c measurements is shown in Figure 6.1 and of A_b measurements in Figure 6.2. The results presented in this Thesis represent the most precise single determinations of each parameter. The SLD combined values for both asymmetries are also shown and seen to be in good agreement with the Standard Model. Correlations in the statistical and systematic errors between the measurements are accounted for in these combinations, with the most significant being a 35% correlation in the statistical error between the results in this Thesis and the "JetC" A_b measurements. Also plotted for comparison purposes are values of A_c and A_b which have been extracted from the LEP measurements of A^c_{FB} and A^b_{FB}. These use the relation $A^f_{FB} = \frac{3}{4}A_e A_f$, with the value of $A_\ell = 0.1501 \pm 0.0016$ coming from the combination of the SLD A_{LR} and $\tilde{A}^\ell_{FB}$ measurements and the LEP A^ℓ_{FB} and τ-polarization measurements. In this chapter lepton universality will always be assumed, so that $A_e = A_\mu = A_\tau = A_\ell$. The value of the SLC polarized electron beam for electroweak asymmetry measurements is apparent, as SLD obtains comparable precision with a factor of ~ 30 fewer events.

Figure 6.1: Summary of A_c measurements at SLD and LEP. The vertical line indicates the Standard Model value. The LEP A^c_{FB} measurements have been converted to A_c values for comparison.

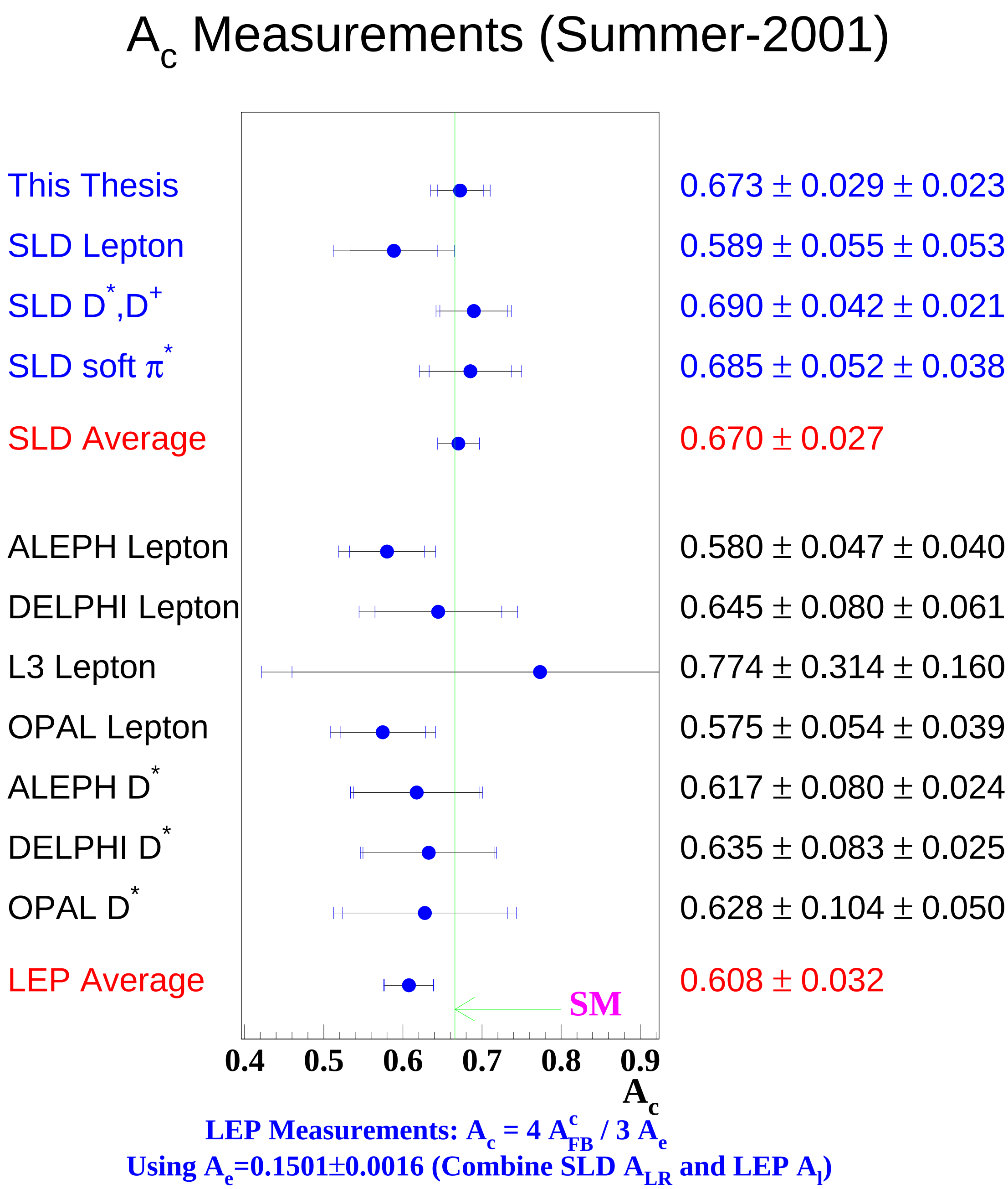

Figure 6.2: Summary of A_b measurements at SLD and LEP. The vertical line indicates the Standard Model value. The LEP A^b_{FB} measurements have been converted to A_b values for comparison.

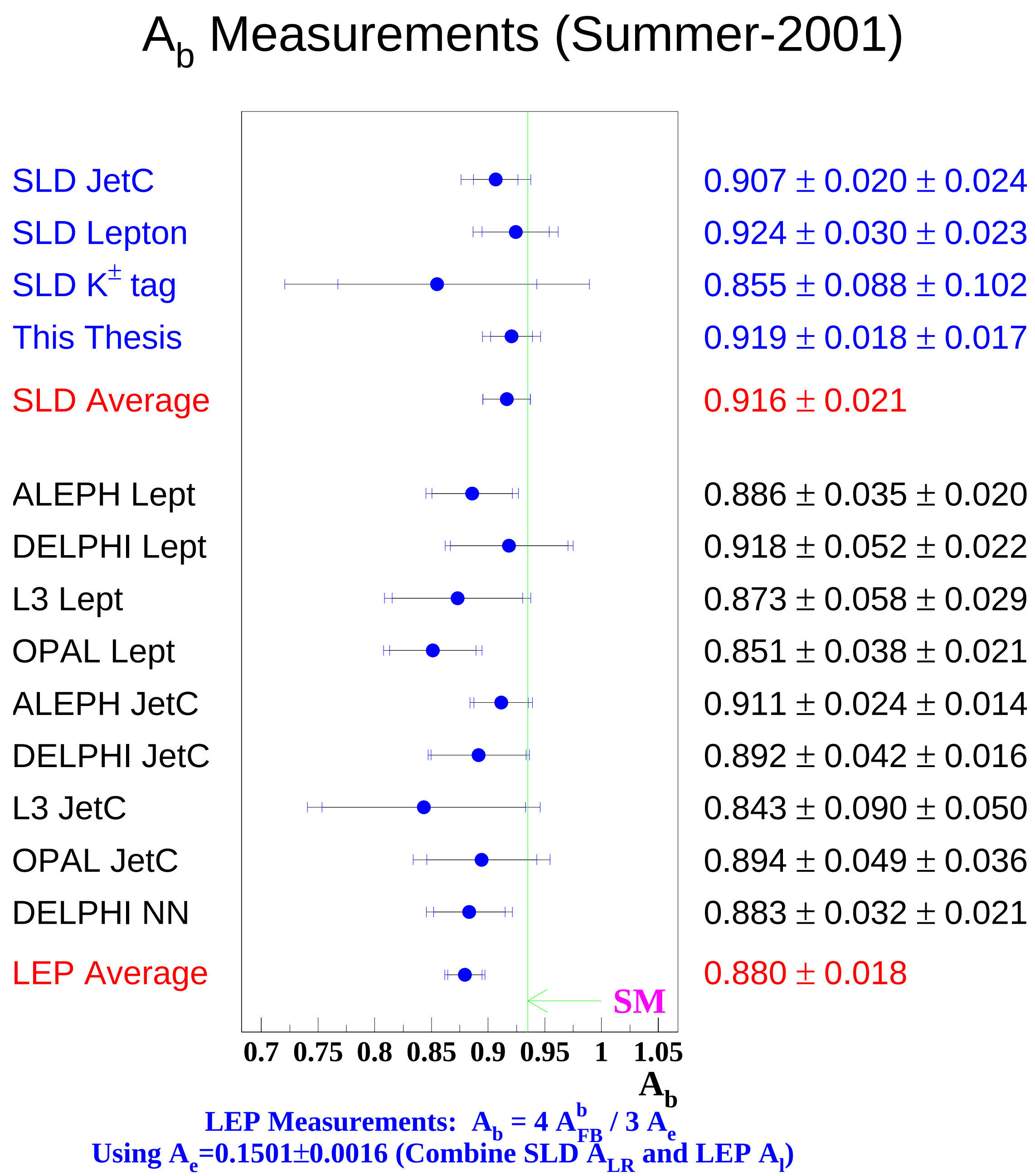

6.1 Other SLD Measurements

Measurements of both A_c and A_b have been made using identified leptons [49]. This method tags heavy flavor using high-momentum electrons and muons, with the charge of the lepton providing the quark/antiquark separation. Multivariate techniques are used to sort the selected leptons into categories such as $b \to \ell$, $b \to c \to \ell$, $c \to \ell$, and misidentifications, from which fits for A_c and A_b are performed.

A method which has been used to measure A_c is to fully reconstruct charmed mesons [50]. For charged mesons the net charge provides quark/antiquark discrimination, while for neutral mesons the charge of the track thought to be a kaon is used. A semi-inclusive sample of charmed mesons selected using the slow pion from D^* decays has also been used to measure A_c [50].

The jet charge method of measuring A_b uses the difference in a momentum-weighted track charge between the two hemispheres to find the quark direction [51]. This measurement uses a mass tagging technique similar to that described in this Thesis to select pure samples of b events. The analyzing power of the quark/antiquark separation is calibrated from the data to minimize the systematic errors, although the uncertainties associated with the hemisphere correlations are somewhat larger than for the method presented in the Thesis.

Also shown in the table is a measurement of A_b using charged kaons which used only the 1993-95 SLD data [52]. The large systematic error is related to the uncertainties associated with $K^{\pm}$ production in B decays, since this method is not efficient enough to permit calibration of the analyzing power from the data.

6.2 Global Analysis

The LEP Electroweak Working Group (LEWWG) has performed a global analysis of all of the precision electroweak data from LEP, SLD, and other experiments. Details of the fitting procedure and the experimental inputs can be found in [47]. This fit tests the consistency of the Standard Model, and also yields a prediction for the mass of the Standard Model Higgs boson. The first step in the fit is the combination of all results for each observable, taking into account all systematic errors which are correlated between separate experiments, and including the interdependences of the parameters (*i.e.* the measured value of A_b depends upon the value of R_b that is assumed). The combined parameter values are shown in Table 6.1. The value of A_b obtained by the LEWWG combination is slightly different from that shown in Figure 6.2. This difference is caused by the SLD measurement of A_c using identified leptons. Because it has a much stronger dependence on A_b than the other A_c determinations the combination procedure prefers to push A_b higher to bring the A_c value for this method closer to the others, an effect which is not included in the SLD combination.

The best-fit Standard Model predictions for each of these observables were calculated using ZFITTER [46] and are also shown in Table 6.1. The ZFITTER program calculates all of the Standard Model parameters at one-loop order using six inputs: The Fermi constant $G_F = (1.16637 \pm 0.00001) \times 10^{-5}$ GeV^{-2}, the Z mass m_Z, the top quark mass m_t, the Higgs mass m_H, the strong coupling $\alpha_s = 0.118 \pm 0.003$, and the light-quark contribution to the photon vacuum polarization $\Delta\alpha^{(5)}_{had}(m_Z^2)$. The top quark contribution to the vacuum polarization can be calculated, but for the lighter quarks ($udscb$) a dispersion relation is used to derive $\Delta\alpha^{(5)}_{had}(m_Z^2)$ from measurements of $R = \frac{e^+e^- \to \text{hadrons}}{e^+e^- \to \mu^+\mu-}$ at lower energies. The value derived in [53] is used for the fit.

The fit pulls, shown in the last column of Table 6.1, result in a total fit χ^2 of 22.9 for 15 degrees of freedom (8.6% probability). Overall, the Standard Model successfully explains all

Table 6.1: Measured electroweak parameters and Standard Model predictions.

	measured	SM prediction	pull
m_Z	91.1875 ± 0.0021	91.1874	0.03
Γ_Z	2.4952 ± 0.0023	2.4963	-0.48
σ_h^0	41.540 ± 0.037	41.481	1.60
R_ℓ	20.767 ± 0.025	20.739	1.11
A_{FB}^{ℓ}	0.01714 ± 0.00095	0.01649	0.69
A_ℓ (from P_τ)	0.1465 ± 0.0033	0.1483	-0.54
R_b	0.21646 ± 0.00065	0.21573	1.12
R_c	0.1719 ± 0.0031	0.1723	-0.12
A_{FB}^{b}	0.0990 ± 0.0017	0.1039	-2.90
A_{FB}^{c}	0.0685 ± 0.0034	0.0743	-1.71
A_b	0.922 ± 0.020	0.935	-0.64
A_c	0.670 ± 0.026	0.668	0.06
A_ℓ	0.1513 ± 0.0021	0.1483	1.47
$\Delta\alpha_{\rm had}^{(5)}(m_Z^2)$	0.02761 ± 0.00036	0.02774	-0.35
$\sin^2\theta_{eff}$ (from $\langle Q_{FB}\rangle$)	0.2324 ± 0.0012	0.2314	0.86
m_t	174.3 ± 5.1	175.8	-0.30
m_W (LEP-II)	80.450 ± 0.039	80.398	1.32
m_W ($p\bar{p}$)	80.454 ± 0.060	80.398	0.93
$\sin^2\theta_W$ (from νN)	0.2255 ± 0.0021	0.2226	1.22
Q_W (from Cs)	-72.50 ± 0.70	-72.89	0.56

of the precision electroweak data.

6.2.1 Heavy Quark Couplings

Using the combined measurements tests of the $Zc\bar{c}$ and $Zb\bar{b}$ vertices were performed. The two observables of interest are R_f and A_f, which are proportional to $g_{Lf}^2 + g_{Rf}^2$ and $g_{Lf}^2 - g_{Rf}^2$, respectively. In order to include the LEP A_{FB}^f measurements, the A_e measurements must also be included as described above to isolate A_f. The relationship between A_ℓ, A_f, and A_{FB}^f for $f = c, b$ is shown in Figure 6.3. In both cases the measurements are consistent with each other, however for $f = b$ the measurements appear to be inconsistent with the Standard Model. Alternatively, if the Standard Model values for A_c and A_b are assumed the

Figure 6.3: Relationship between SLD+LEP A_ℓ measurements (vertical band), SLD A_f measurements (horizontal band), and LEP A_{FB}^f measurements (diagonal band) for c (left) and b (right). The line segments indicate the Standard Model predictions for $m_H = 300^{+700}_{-205}$ GeV/c^2 (longer segment) and $m_t = 174.3 \pm 5.1$ GeV/c^2 (short segment). Lower m_H is on the right.

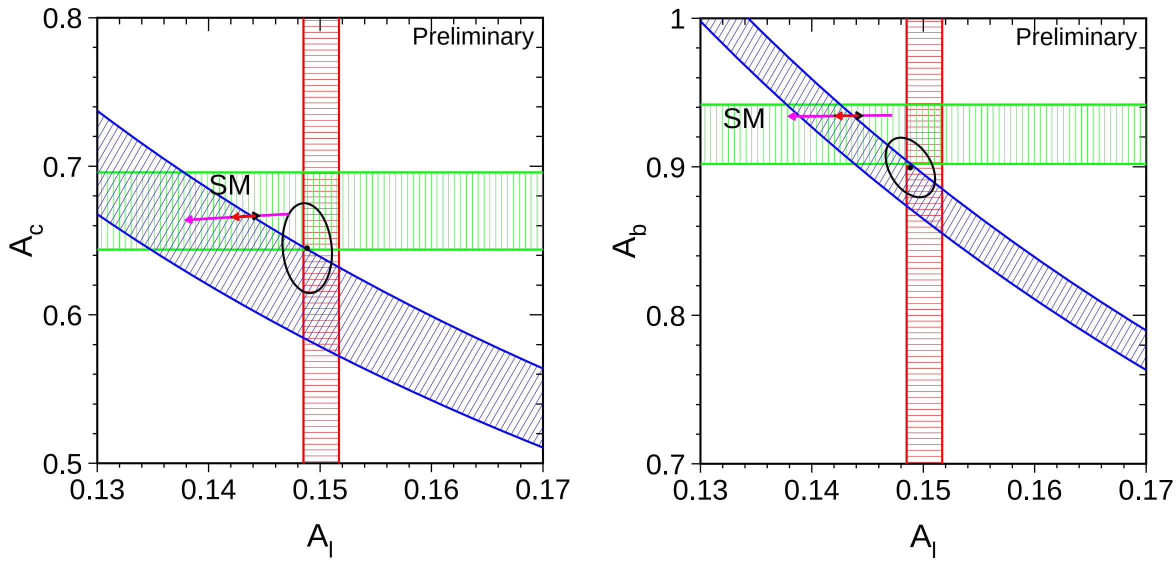

measurements of A_ℓ and A_{FB}^f appear to prefer disparate ranges of m_H.

From the measurements of R_f, A_f, A_{FB}^f, and A_ℓ fits were performed for the left-handed couplings g_{Lf} and the right-handed couplings g_{Rf}. The results are plotted in Figure 6.4 and compared to the Standard Model expectations in Table 6.2. The $Zc\bar{c}$ couplings are in good agreement with the Standard Model predictions, but there is a 3σ discrepancy in g_Rb. This effect is driven entirely by the value of A_b extracted from A_{FB}^b and A_ℓ, as the R_b and direct A_b measurements are in good agreement with the Standard Model. Because of the tight constraint imposed upon the sum of the couplings by the R_b measurements, attempts to interpret this discrepancy as possible evidence of new physics in g_{Rb} involve unnatural fine-tuning of g_{Lf} to maintain this sum at its Standard Model value. For this reason, it seems more likely that the effect is a statistical fluctuation rather than evidence of new physics. For the remainder of this chapter these couplings will be assumed to have their Standard

Figure 6.4: Results of the fit for the left- and right-handed couplings g_{Lf} and g_{Rf} for $f = c$ (left) and $f = b$ (right).

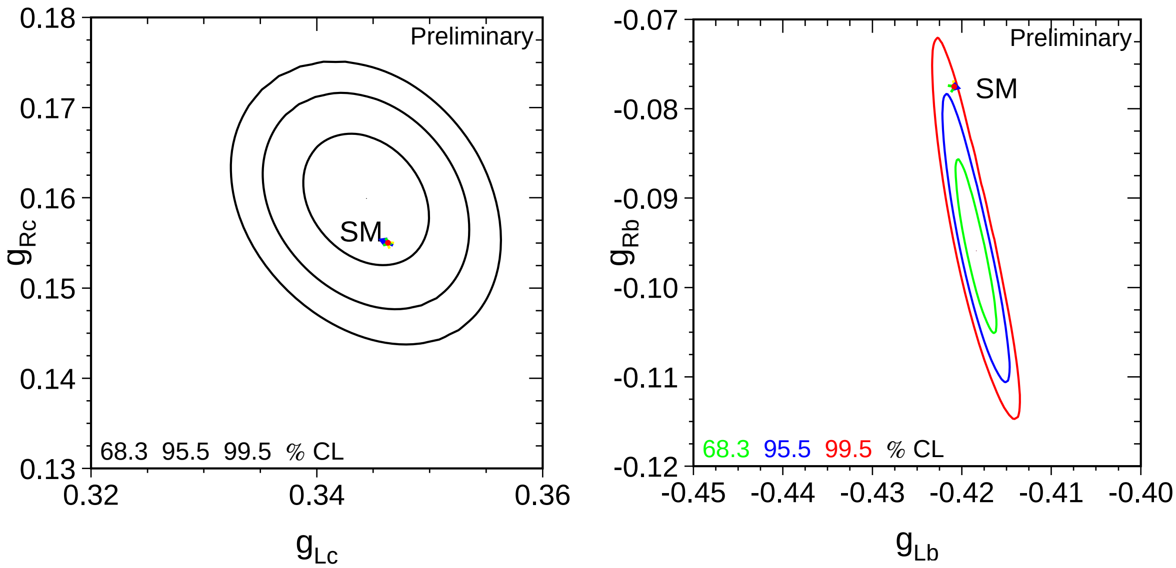

Table 6.2: Results of the fit for left- and right-handed couplings g_{Lf} and g_{Rf} for $f = c, b$, along with their Standard Model predictions.

	Standard Model	Fit Result
g_{Lc}	0.3464	0.3443±0.0037
g_{Rc}	0.1550	0.1600±0.0048
g_{Lb}	-0.4207	-0.4183±0.0015
g_{Rb}	-0.0776	-0.0962±0.0064

Model values, so that A_{FB}^f can be treated as a measurement of $\sin^2\theta_{eff}$.

6.2.2 Prediction of m_W and m_t

An important test of the Standard Model is the prediction of the W and top quark masses from the precision electroweak data. This is done by performing the fit without the m_W and m_t measurement constraints. The preferred range of m_W versus m_t is shown in Figure 6.5, along with the values measured at LEP-II and the TeVatron. The fitted values of $m_W = 80.363 \pm 0.032$ GeV/c^2 and $m_t = 169.0 \pm 9.9$ GeV/c^2 are in excellent agreement with the

Figure 6.5: Results of the fit for m_W and m_t from the electroweak precison data, compared to the direct measurements from LEP-II and TeVatron experiments. The diagonal band shows the dependence of the Higgs mass m_H on m_W and m_t.

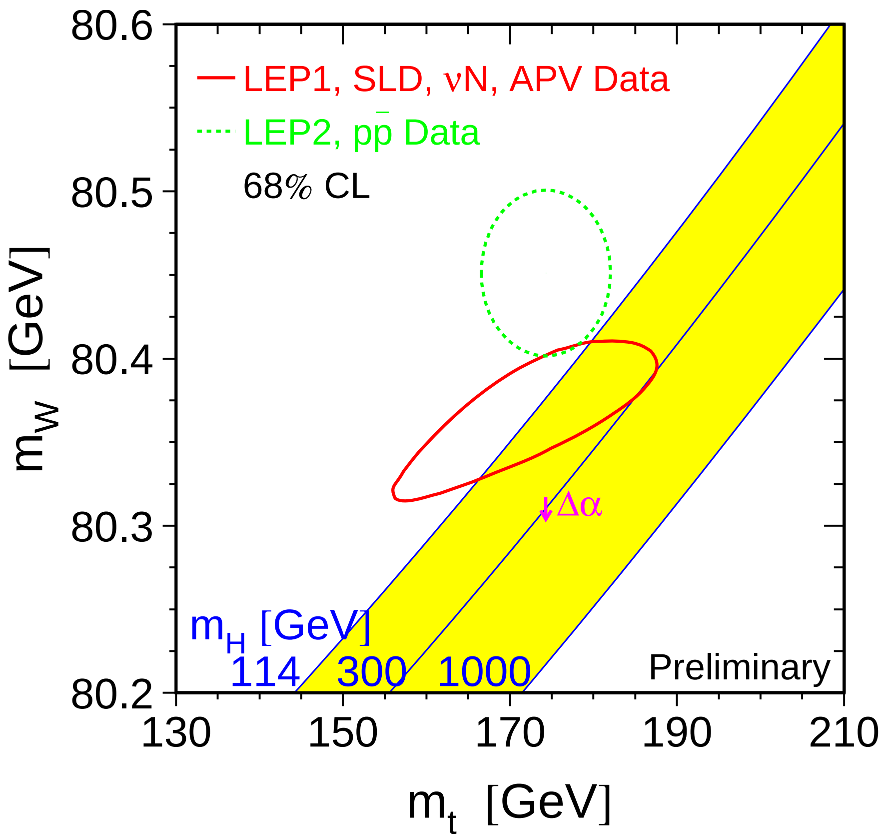

measured values of $m_W = 80.451 \pm 0.033$ GeV/c^2 and $m_t = 174.3 \pm 5.1$ GeV/c^2, demonstrating the success of the Standard Model in explaining the precision electroweak data.

6.2.3 Higgs Mass Fit

Including the measured values of m_W and m_t, the electroweak precision data can be used to constrain the mass of the Higgs boson. The sensitivity to m_H for the most significant parameters measured at LEP and SLD is shown in Figures 6.6 and 6.7. All of the measurements prefer a Higgs mass lower than 200 GeV/c^2 except for the heavy quark forward-backward asymmetries A^c_{FB} and A^b_{FB}. This is the same effect mentioned in connection with Figure 6.3.

Figure 6.6: Sensitivity of selected electroweak parameters to m_H.

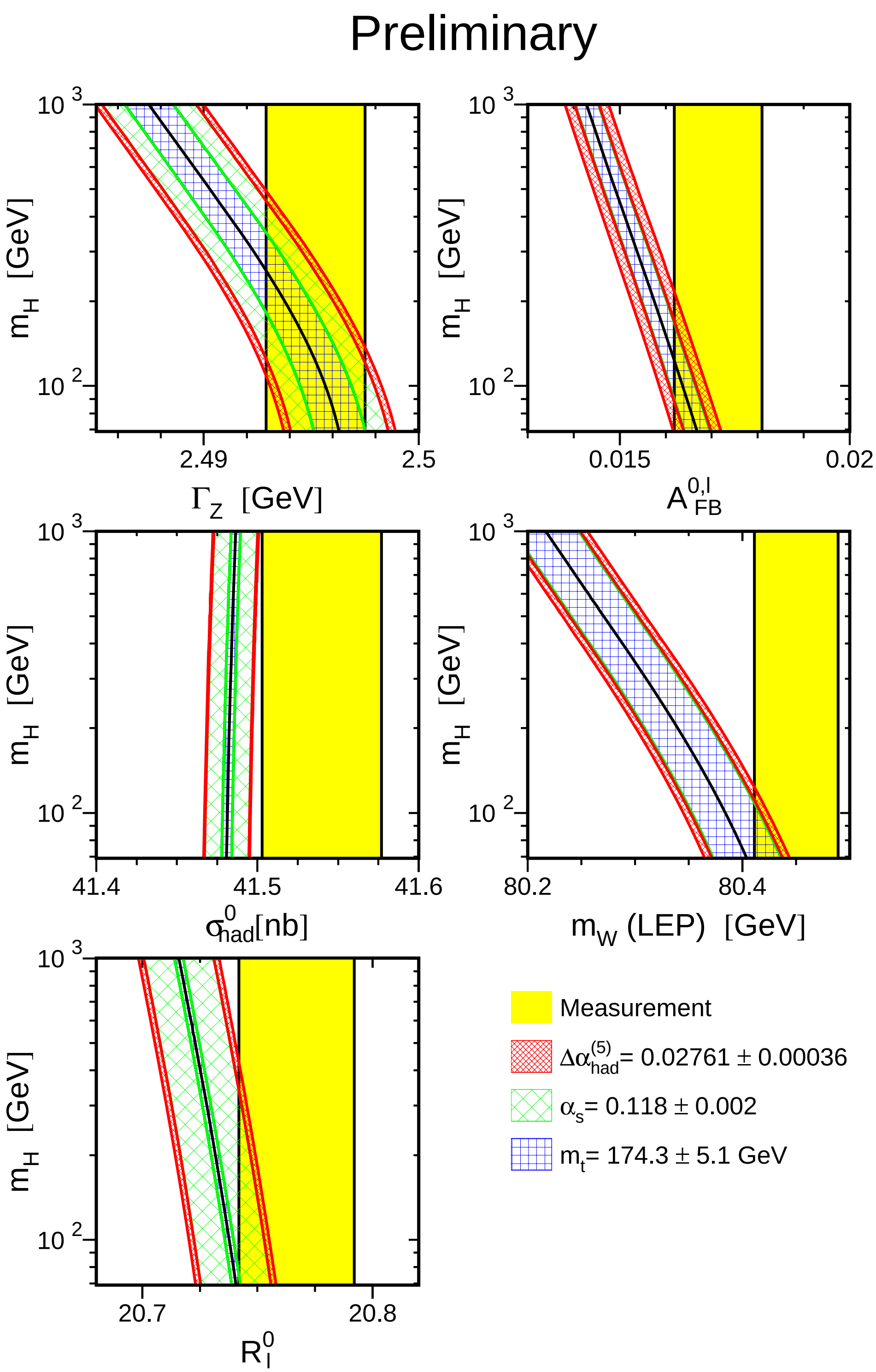

Figure 6.7: Sensitivity of selected electroweak parameters to m_H.

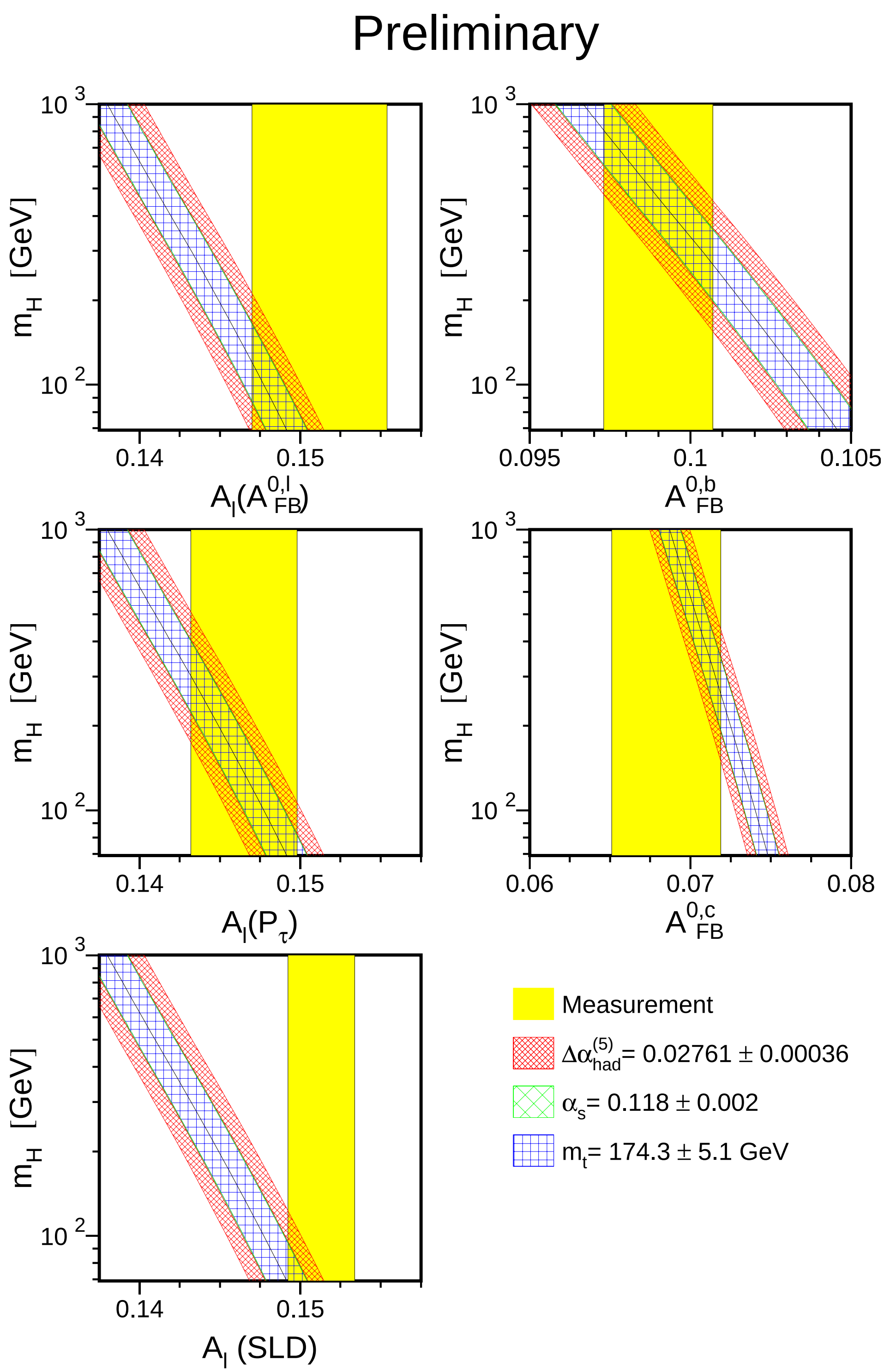

Figure 6.8: Results of the Standard Model fit for m_h.

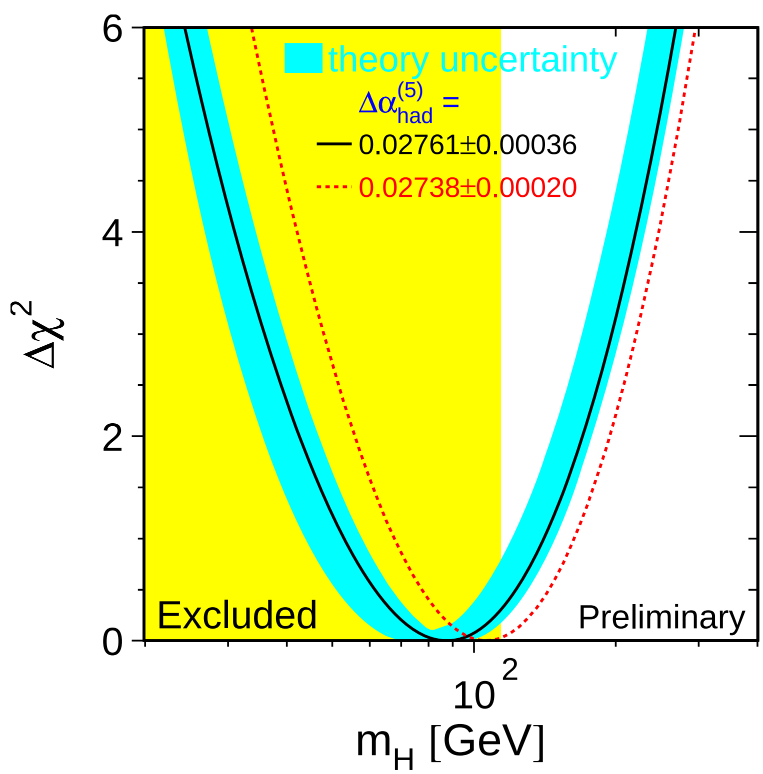

The mass of the Standard Model Higgs extracted from the fit is $m_H = 88^{+53}_{-35}$ GeV/c, with the asymmetric error resulting from the logarithmic dependence of $\sin^2\theta_{eff}$ on m_H. The χ^2 of the fit versus m_H is shown in Figure 6.8. From the χ^2 surface an upper limit of $m_H < 196$ GeV/c^2 at 95% CL can be derived. The dotted curve results from using an alternate determination of $\Delta\alpha^{(5)}_{\text{had}}$ [54], in which case the 95% CL limit is $m_H < 222$ GeV/c^2.

The shaded region on Figure 6.8 indicates the region which has been excluded by direct searches at LEP-II [55], $m_H < 114.1$ GeV/c^2 at 95% CL. These searches prefer a Higgs mass of 115.6 GeV/c^2, although the signal significance is low with a 3.4% chance of consistency with background.

Whether or not the LEP-II results represent a real signal, the indirect constraints from the precision electroweak data indicate a relatively light Higgs mass which may be accessible to the Run-II program at the TeVatron. This sets up interesting possibilities. If the TeVatron searches were to make a 3σ observation of the Higgs in the same mass region as LEP-II, the combination of the direct results with the indirect constraints would provide strong evidence of the existence of a low -mass Higgs. On the other hand, if the TeVatron searches do not see any such evidence and instead exclude more of the range favored by the indirect constraints, this would indicate a problem with the Standard Model picture of a single Higgs boson. In either case, the information provided by the precision electroweak measurements constitute an indispensible part of the effort to understand electroweak spontaneous symmetry breaking.

Appendix A

Tag Calibration

The tag calibration procedure is performed in two steps. The first calibrates the tag efficiences ϵ_b^H, ϵ_c^H, ϵ_c^L, and ϵ_b^L. In the second step, the correct-sign probabilities p_b^H, p_c^L, and p_b^L are found.

From the calibrated hemisphere efficiencies and correct-sign probabilities, the event purities and correct-sign probabilities needed for the likelihood fits can be calculated. As noted in the text, separate values for single-tagged and double-tagged events are determined.

A.1 Efficiency Calibration

From the two tags L and H, five event types of interest can be constructed. They are: single-H-tagged (XH), double-H-tagged (HH), mixed-tagged (LH), single-L-tagged (XL), and double-L-tagged (LL). The symbols in parentheses denote the combination of the tags in the two hemispheres for each, with X representing a hemisphere which passes neither the L nor the H tag. The fractions $F_{t_1 t_2}$ of all hadronic events constituted by each of these event types, shown in Table A.1, are the observable inputs to the efficiency tagging procedure.

The efficiency ϵ_f^t is the probability to tag a hemisphere in an event of flavor f with the

Table A.1: Number observed $N_{t_1t_2}$ and fraction of the $N_{tot} = 228712$ selected hadronic events $F_{t_1t_2}$ in the data for each of the five event types.

t_1t_2	$N_{t_1t_2}$	$F_{t_1t_2}$
XH	21473	0.0939
HH	5236	0.0229
LH	748	0.0033
XL	9504	0.0416
LL	558	0.0024

tag t, so the probability to tag an event with tag combination t_1t_2 should be proportional to the product of the individual probabilities $\epsilon_f^{t_1}\epsilon_f^{t_2}$. For example, the double-H-tagged fraction would be proportional to $(\epsilon_b^H)^2$, neglecting the small c background. The single-H-tagged fraction would be proportional to $\epsilon_b^H(1 - \epsilon_b^L - \epsilon_b^H)$, where the term in parentheses is the probability to *not* tag a hemisphere as L or H, and again the c background is omitted. In this way it is a simple matter to write expressions for each of the event fractions in terms of the efficiencies ϵ_f^t and also the hadronic partial widths R_f which express the initial flavor probabilities.

In writing the event fractions as products of the hemisphere tagging efficiencies, the implicit assumption is that the hemispheres are independent. This means that the tagging outcome in one hemisphere is unaffected by the outcome in the other. The simulation was used to check this assumption, by comparing the tagging efficiencies for all hemispheres to the efficiencies for hemispheres opposite an L or H tag. Two moderate discrepancies were found, for ϵ_b^H opposite another H-tagged b event hemisphere and for ϵ_c^L opposite another L-tagged c event hemisphere. These effects are parameterized by factors ξ_f^t, which express the enhancement in the tagging efficiency ϵ_f^t when it is opposite another t-tagged hemispere. By this is meant that in a b event, for example, if one hemisphere has been H-tagged the efficiency for the other hemisphere to also be H-tagged is $\xi_b^H\epsilon_b^H$ rather than just ϵ_b^H. Quantitatively, $\xi_b^H = 1.005 \pm 0.002$ and $\xi_c^L = 1.029 \pm 0.007$ respectively, where the errors are from Monte Carlo statistics only. The predictions for the event fractions must be corrected for these enhancements, so that the examples given above would now be written as $F_{HH} \propto \xi_b^H(\epsilon_b^H)^2$ and $F_{XH} \propto \epsilon_b^H(1-\epsilon_b^L-\xi_b^H\epsilon_b^H)$. A full accounting of the causes of these hemisphere tagging correlations is given in Appendix B. Omitting these corrections would incorrectly lower the measured values of A_c and A_b by 0.4%.

The calibration procedure starts with the fractions of single-H-tagged and double-H-tagged events F_{XH} and F_{HH} observed in the data. Using the ideas discussed above, these can be written as:

$$F_{XH} = 2\left[\epsilon_b^H(1-\epsilon_b^L-\xi_b^H\epsilon_b^H)R_b+\epsilon_c^H(1-\epsilon_c^L-\epsilon_c^H)R_c+\epsilon_{uds}^H(1-R_b-R_c)\right] \quad \text{(A.1)}$$

$$F_{HH} = \xi_b^H(\epsilon_b^H)^2R_b+(\epsilon_c^H)^2R_c \quad \text{(A.2)}$$

where the factor of two in F_{XH} accounts for the possibility to have the H tag in either hemisphere. Terms quadratic in ϵ_{uds}^t have been omitted from the analysis for simplicity, since their contribution is always negligible. The parameter ξ_b^H is inserted to account for the slightly higher probability to tag a b event hemisphere as H when the opposite hemisphere has also been tagged as H as discussed above. In the sum over flavors the hadronic partial widths R_f are inserted to reflect the differing initial populations in the sample. Because the double-H-tagged events are overwhelmingly b, F_{HH} can be used to extract ϵ_b^H with very little background. Once ϵ_b^H is known, its contribution can be subtracted from F_{XH} to yield ϵ_c^H, although the statistical power is limited. In this way, both the signal efficiency ϵ_b^H and the main background level ϵ_c^H can be constrained from the data.

The next step uses the fraction of all events in the data in which one hemisphere is tagged as L and the other is tagged as H. Denoted F_{LH}, it can be written as:

$$F_{LH} = 2\left(\epsilon_b^L\epsilon_b^H R_b+\epsilon_c^L\epsilon_c^H R_c\right) \quad \text{(A.3)}$$

Table A.2: Results of the efficiency calibration procedure. Shown for comparison are the expectations from the Monte Carlo simulation.

efficiency	MC	calibrated
ϵ_b^H	0.323	0.325±0.002
ϵ_c^H	0.005	0.006±0.002
ϵ_c^L	0.121	0.115±0.002
ϵ_b^L	0.020	0.022±0.001

with the factor of two accounting for the two ways in which the L and H tags can be distributed over the two hemispheres. Because the H tag has higher efficiency and purity than the L tag these events are ~90% b. Inserting the calibrated value of ϵ_b^H allows extraction of ϵ_b^L, the level of b background under the L tag.

The last step uses the fractions of single-L-tagged and double-L-tagged events F_{XL} and F_{LL} observed in the data. These can be written as:

$$F_{XL} = \epsilon_c^L(1 - \xi_c^L\epsilon_c^L - \epsilon_c^H)R_c + \epsilon_b^L(1 - \epsilon_b^L - \epsilon_b^H)R_b + \epsilon_{uds}^L(1 - R_c - R_b) \quad \text{(A.4)}$$

$$F_{LL} = \xi_c^L(\epsilon_c^L)^2 R_c + (\epsilon_b^L)^2 R_b \quad \text{(A.5)}$$

where the order of the flavors has been reversed to reflect the predominantly c composition of these samples. The parameter ξ_c^{LL} is inserted to account for the double-L-tag enhancement discussed above. Because ϵ_c^L is not large, the efficiency cannot be calibrated from F_{LL} alone as was done for ϵ_b^H. However, since the background level ϵ_b^L is already known from F_{LH}, the single-L-tag fraction F_{XL} can be used to extract ϵ_c^L with good statistics.

In practice a fit is used to simultaneously extract all four efficiencies from the observed rates. It is useful to consider the procedure in this sequential manner, however, as it better illustrates the sensitivity of each tagging rate to the efficiencies. The resulting calibrated efficiencies are shown in Table A.2. Also shown are the expectations from the simulation, which are in very good agreement.

Table A.3: Number observed $N_{t_1t_2}$ and fraction with opposite-sign Q_{tag} values $r_{t_1t_2}$ in the data for each of the the double-tag event types.

t_1t_2	$N_{t_1t_2}$	$r_{t_1t_2}$
HH	5236	0.706
LH	748	0.511
LL	558	0.835

A.2 Correct-Sign Probability Calibration

The calibration of the tag correct-sign probabilities is done by comparing the signs of the Q_{tag} values in double-tagged events. Because of the way Q_{tag} and p_f^t have been defined, in an event with both hemispheres tagged correctly the Q_{tag} values will always have opposite signs regardless of the event flavor or tag combination. However, events with both hemispheres tagged incorrectly will also have opposite-sign Q_{tag} values, so this possibility must be taken into account. Using a joint probability principle analogous to that used in the efficiency calibration, the fraction of t_1t_2-tagged events which have opposite-sign Q_{tag} values, denoted as $r_{t_1t_2}$, should be proportional to $p_f^{t_1}p_f^{t_2}+(1-p_f^{t_1})(1-p_f^{t_2})$. The numbers of events and values of $r_{t_1t_2}$ for the three double-tagged event types HH, LH, and LL are given in Table A.3.

It should be noted that this method automatically accounts for the effects of neutral-meson mixing. An event in which one meson mixes may have both hemispheres tagged with the correct charge sign for the quark/antiquark content at the time of the heavy meson decay, producing a same-sign event in apparent contradiction to what was stated above. However, what is needed for these measurements is the quark/antiquark nature of the hemisphere at the time of the Z decay. Therefore, the mixed hemisphere with a correctly charged final state is in fact incorrect by this standard, and is properly treated as such by this method.

An important caveat is that this procedure calibrates the correct-sign probabilities in double-tagged event hemispheres. It is natural to ask if these values are representative of all hemispheres. The simulation was used to compare the value of p_f^t for all hemispheres to that found in hemispheres opposite the various tags. As in the efficiency calibration, the double-L-tagged and double-H-tagged events were found to differ from the single-tagged and mixed-tagged events. In this case, rather than the difference between a hemisphere in a double-tagged event compared to any hemisphere, it is simpler to use the difference between a t-tagged hemisphere in a double-t-tagged event and a t-hemisphere in a single-t-tagged or mixed-tagged event. These differences are represented by the parameters ζ_b^H and ζ_c^L, so that $p_b^{HX+HL} = \zeta_b^H p_b^{HH}$ and $p_c^{LX+LH} = \zeta_c^L \epsilon_c^{LL}$. The notation $p_f^{t_1 t_2}$ expresses the correct-sign probability for a tag of type t_1 when the opposite hemisphere has been tagged as t_2. The simulation indicates that $\zeta_b^H = 0.995 \pm 0.001$ and $\zeta_c^L = 0.993 \pm 0.002$, where the errors are due only to Monte Carlo statistics. The main effect causing these differences is having both heavy hadrons in the same hemisphere of an event, due to hard QCD radiation. A full account of this and other sources is given in Appendix B. Omitting this correction would incorrectly lower the measured values of A_c and A_b by 1.1%.

For the background correct-sign probabilities p_c^H and p_b^L, no significant effects were seen in the simulation and no corrections are made. The notation $p_f^{t_1 t_2}$ will therefore not be used for these, since they are always assumed to equal $p_f^{t_1}$.

The procedure starts with the events in the data in which both hemispheres are tagged as H. The fraction of these events in which the Q_{tag} values are opposite-sign, denoted r_{HH}, can be written as:

$$r_{HH} = \Pi_b^{HH} \left[(p_b^{HH})^2 + (1 - p_b^{HH})^2 \right] + \Pi_c^{HH} \left[(p_c^H)^2 + (1 - p_c^H)^2 \right] \qquad (A.6)$$

where Π_b^{HH} and Π_c^{HH} are the fractions of the double-H-tagged sample composed of b and c, respectively. These can be computed from:

$$\Pi_b^{HH} = \frac{\xi_b^H (\epsilon_b^H)^2 \; R_b}{\xi_b^H (\epsilon_b^H)^2 R_b + (\epsilon_c^H)^2 R_c} \qquad (A.7)$$

$$\Pi_c^{HH} = \frac{(\epsilon_c^H)^2 \; R_c}{\xi_b^H(\epsilon_b^H)^2 R_b + (\epsilon_c^H)^2 R_c} \tag{A.8}$$

using the calibrated efficiencies. The correlation parameter ξ_b^H is used here to obtain the correct double-tag efficiency for b events. Once these are known, p_b^{HH} can be extracted with only a small correction from p_c^H.

The next step uses the events in the data in which both hemispheres are tagged as L. The fraction of these events in which the Q_{tag} values are opposite-sign, denoted r_{LL}, can be written as:

$$r_{LL} = \Pi_c^{LL}\left[(p_c^{LL})^2 + (1-p_c^{LL})^2\right] + \Pi_b^{LL}\left[(p_b^L)^2 + (1-p_b^L)^2\right] \tag{A.9}$$

where Π_c^{LL} and Π_b^{LL} are the fractions of this sample composed of c and b, respectively. They can be computed from:

$$\Pi_c^{LL} = \frac{\xi_c^L(\epsilon_c^L)^2 \; R_c}{\xi_c^L(\epsilon_c^L)^2 R_c + (\epsilon_b^L)^2 R_b} \tag{A.10}$$

$$\Pi_b^{LL} = \frac{(\epsilon_b^L)^2 \; R_b}{\xi_c^L(\epsilon_c^L)^2 R_c + (\epsilon_b^L)^2 R_b} \tag{A.11}$$

using the calibrated efficiencies and the correlation parameter ξ_c^L. Although the statistics available are much smaller than for r_{HH}, the very high value of p_c^{LL} allows its calibration with an uncertainty comparable to that for p_b^{HH}.

The last step uses the events in the data in which one hemisphere is tagged as L and the other is tagged as H. The fraction of these events in which the Q_{tag} values are opposite-sign, denoted r_{LH}, can be written as:

$$r_{LH} = \Pi_b^{LH}\left[p_b^L\zeta_b^H p_b^{HH} + (1-p_b^L)(1-\zeta_b^H p_b^{HH}\right] + \Pi_c^{LH}\left[\zeta_c^L p_c^{LL} p_c^H + (1-\zeta_c^L p_c^{LL})(1-p_c^H\right] \tag{A.12}$$

where the parameters ζ_b^H and ζ_c^L defined above has been used to convert p_b^{HH} and p_c^{LL} into

Table A.4: Results of the correct-sign calibration procedure. Shown for comparison are the expectations from the Monte Carlo simulation.

probability	MC	calibrated
p_b^{HH}	0.807	0.821±0.005
p_c^{LL}	0.932	0.918±0.010
p_b^{L}	0.545	0.543±0.031

values appropriate for this sample. Π_b^{LH} and Π_c^{LH} are the fractions of this sample of b and c events, respectively. They can be computed from:

$$\Pi_b^{LH} = \frac{\epsilon_b^L \epsilon_b^H R_b}{\epsilon_b^L \epsilon_b^H R_b + \epsilon_b^L \epsilon_b^H R_b} \tag{A.13}$$

$$\Pi_b^{LH} = \frac{\epsilon_c^L \epsilon_c^H R_c}{\epsilon_b^L \epsilon_b^H R_b + \epsilon_b^L \epsilon_b^H R_b} \tag{A.14}$$

using the calibrated efficiencies. Again, because this sample is ∼90% b, the value of p_b^L can be extracted using the known p_b^{HH} with only a small correction needed for the c background. This ability to constrain the correct-sign probability of the b background under the L tag is very important for the measurement of A_c. Otherwise, the systematic errors associated with such a significant background could be quite sizable if this number were taken from the simulation.

As for the efficiency calibration, in practice these correct-sign probabilities are determined using a simultaneous fit to all three of the opposite-sign fractions. The results of the correct-sign probability calibration are shown in Table A.4. Also shown are the expections from the simulation, which again are in very good agreement.

In contrast to the efficiency ϵ_c^H, the correct-sign probability p_c^H for the c background under the H tag cannot be calibrated from the data. Therefore, another approach must be used to constrain it. Estimating p_c^H from the simulation would be difficult, as it is likely quite dependent upon non-Gaussian tails in the tracking resolution. Instead, a simple argument is used to constrain $p_c^H \leq 0.5$.

The statement that $p_c^H \leq 0.5$ implies that Q_{tag} for the c background under the H tag will be predominantly negative for quark hemispheres rather than positive (wrong-sign). One way for c event hemispheres to leak into the H-tagged sample is when all of the correct tracks are selected, but M_{hem} is incorrectly calculated, for example if the missing neutral p_T is misestimated. These will always be wrong-sign since the c quark is positive while the b quark is negative. Another source is when the c event hemisphere track list includes an incorrect track from the IP. For neutral c hadrons, the misattached track should be more-or-less randomly charged, so these should have $p_c^H \sim 0.5$. For charged c hadrons, the extra track can either be oppositely-charged to the hadron, producing net charge zero and rejection of the vertex, or the same charge as the hadron, leaving the vertex wrong-sign. For more than one misattached track the pattern holds that there are always more ways to get a wrong-sign charged vertex. Therefore, p_c^H can be constrained in $[0, 0.5]$, equivalent to $p_c^H = 0.25 \pm 0.14$ for a uniform distribution. This is in good agreement with the value of 0.30 indicated by the simulation. The value $p_c^H = 0.25$ is used in both the calibration procedure and in the likelihood fit for A_b, with the uncertainty of ± 0.14 used to set systematic errors on A_c and A_b.

A.3 A_c Fit Parameters

What will be needed for the likelihood fit for A_c are the purity and correct-sign probability for the event types used in the fit. In the case of A_c these are XL (single-tagged) and LL (double-tagged), where in the LL subsample the events with same-sign Q_{tag} values are discarded.

Table A.5: Single-tag and double-tag purities Π_f^s and Π_f^d used in the A_c fit. The quoted errors are due only to the statistical uncertainties of the calibrated quantities. Also shown are the Monte Carlo expectations.

flavor	MC Π_f^s	calibrated Π_f^s	MC Π_f^d	calibrated Π_f^d
c	0.8519	0.8355±0.0058	0.9810	0.9751±0.0025
b	0.1312	0.1470±0.0058	0.0190	0.0249±0.0025
uds	0.0169	0.0175	0	0

The three single-tagged flavor purities Π_f^s for the A_c fit can be computed from:

$$\Pi_c^s = \frac{\epsilon_c^L(1-\xi_c^L\epsilon_c^L-\epsilon_c^H)R_c}{\epsilon_c^L(1-\xi_c^L\epsilon_c^L-\epsilon_c^H)R_c+\epsilon_b^L(1-\epsilon_b^L-\epsilon_b^H)R_b+\epsilon_{uds}^L(1-R_c-R_b)} \tag{A.15}$$

$$\Pi_b^s = \frac{\epsilon_b^L(1-\epsilon_b^L-\epsilon_b^H)R_b}{\epsilon_c^L(1-\xi_c^L\epsilon_c^L-\epsilon_c^H)R_c+\epsilon_b^L(1-\epsilon_b^L-\epsilon_b^H)R_b+\epsilon_{uds}^L(1-R_c-R_b)} \tag{A.16}$$

$$\Pi_{uds}^s = \frac{\epsilon_{uds}^L(1-R_c-R_b)}{\epsilon_c^L(1-\xi_c^L\epsilon_c^L-\epsilon_c^H)R_c+\epsilon_b^L(1-\epsilon_b^L-\epsilon_b^H)R_b+\epsilon_{uds}^L(1-R_c-R_b)} \tag{A.17}$$

using the calibrated efficiencies and the correlation parameter ξ_c^L. The two double-tagged purities (the uds contribution is assumed to be zero) are:

$$\Pi_c^d = \frac{\xi_c^L(\epsilon_c^L)^2[(p_c^{LL})^2+(1-p_c^{LL})^2]R_c}{\xi_c^L(\epsilon_c^L)^2[(p_c^{LL})^2+(1-p_c^{LL})^2]R_c+(\epsilon_b^L)^2[(p_b^L)^2+(1-p_b^L)^2]R_b} \tag{A.18}$$

$$\Pi_b^d = \frac{(\epsilon_b^L)^2[(p_b^L)^2+(1-p_b^L)^2]R_b}{\xi_c^L(\epsilon_c^L)^2[(p_c^{LL})^2+(1-p_c^{LL})^2]R_c+(\epsilon_b^L)^2[(p_b^L)^2+(1-p_b^L)^2]R_b} \tag{A.19}$$

using the calibrated correct-sign probabilities as well to account for the dropping of the same-sign Q_{tag} events. These expressions are very similar to those used in the efficiency calibration procedure. The calculated values of Π_f^s and Π_f^d are summarized in Table A.5, along with the expectations from the simulation.

The single-tagged correct-sign probabilities P_f^s are given by:

$$P_c^s = \zeta_c^L p_c^{LL} \tag{A.20}$$

Table A.6: Single-tag and double-tag correct-sign probabilities P_f^s and P_f^d used in the A_c fit. The quoted errors are due only to the statistical uncertainties of the calibrated quantities. Also shown are the Monte Carlo expectations.

flavor	MC P_f^s	calibrated P_f^s	MC P_f^d	calibrated P_f^d
c	0.9251	0.9117±0.0097	0.9946	0.9921±0.0021
b	0.548	0.543±0.032	0.610	0.586±0.063

$$P_b^s = p_b^L \tag{A.21}$$

where the calibrated values of p_c^{LL} and p_b^L are used, and the factor ζ_c^L is inserted to convert the p_c^{LL} calibrated from double-tagged events into a value suitable for single-tags. The double-tagged correct-sign probabilities P_f^d are computed from:

$$P_c^d = \frac{(p_c^{LL})^2}{(p_c^{LL})^2 + (1 - p_c^{LL})^2} \tag{A.22}$$

$$P_b^d = \frac{(p_b^L)^2}{(p_b^L)^2 + (1 - p_b^L)^2} \tag{A.23}$$

again using the calibrated values of p_c^{LL} and p_b^L. The calculated values of P_f^s and P_f^d are summarized in Table A.6, along with the expectations from the simulation.

A.4 A_b Fit Parameters

The events used in the A_b fit are XH and LH (single-tagged), and HH (double-tagged), where in the LH events the Q_{tag} in the L hemisphere is ignored and the HH events with same-sign Q_{tag} values are discarded.

The flavor purities for the A_b fit are computed in the same way as for the A_c fit. The

Table A.7: Single-tag and double-tag purities Π_f^s and Π_f^d used in the A_b fit. The quoted errors are due only to the statistical uncertainty of the calibrated efficiencies. Also shown are the Monte Carlo expectations.

flavor	MC Π_f^s	calibrated Π_f^s	MC Π_f^d	calibrated Π_f^d
b	0.9764	0.9724±0.0071	0.9999	0.9998±0.0002
c	0.0169	0.0210±0.0071	0.0001	0.0002±0.0002
uds	0.0067	0.0066	0	0

mixed-LH-tagged events are treated as single-tagged events here.

$$\Pi_b^s = \frac{\epsilon_b^H(1-\xi_b^H\epsilon_b^H)R_b}{\epsilon_b^H(1-\xi_b^H\epsilon_b^H)R_b + \epsilon_c^H(1-\epsilon_c^H)R_c + \epsilon_{uds}^H(1-R_b-R_c)} \quad \text{(A.24)}$$

$$\Pi_c^s = \frac{\epsilon_c^H(1-\epsilon_c^H)R_c}{\epsilon_b^H(1-\xi_b^H\epsilon_b^H)R_b + \epsilon_c^H(1-\epsilon_c^H)R_c + \epsilon_{uds}^H(1-R_b-R_c)} \quad \text{(A.25)}$$

$$\Pi_{uds}^s = \frac{\epsilon_{uds}^H(1-R_b-R_c)}{\epsilon_b^H(1-\xi_b^H\epsilon_b^H)R_b + \epsilon_c^H(1-\epsilon_c^H)R_c + \epsilon_{uds}^H(1-R_b-R_c)} \quad \text{(A.26)}$$

$$\Pi_b^d = \frac{\xi_b^H(\epsilon_b^H)^2[(p_b^{HH})^2+(1-p_b^{HH})^2]R_b}{\xi_b^H(\epsilon_b^H)^2[(p_b^{HH})^2+(1-p_b^{HH})^2]R_b + (\epsilon_c^H)^2[(p_c^H)^2+(1-p_c^H)^2]R_c} \quad \text{(A.27)}$$

$$\Pi_c^d = \frac{\xi_c^H(\epsilon_c^H)^2[(p_c^{HH})^2+(1-p_c^{HH})^2]R_c}{\xi_b^H(\epsilon_b^H)^2[(p_b^{HH})^2+(1-p_b^{HH})^2]R_b + (\epsilon_c^H)^2[(p_c^H)^2+(1-p_c^H)^2]R_c} \quad \text{(A.28)}$$

The calculated values of Π_f^s and Π_f^d are summarized in Table A.7, along with the expectations from the simulation.

The correct-sign probabilities P_f^s are also computed as for A_c.

$$P_b^s = \zeta_b^H p_b^{HH} \quad \text{(A.29)}$$

$$P_c^s = p_c^H \quad \text{(A.30)}$$

$$P_b^d = \frac{(p_b^{HH})^2}{(p_b^{HH})^2+(1-p_b^{HH})^2} \quad \text{(A.31)}$$

$$P_c^d = \frac{(p_c^H)^2}{(p_c^H)^2+(1-p_c^H)^2} \quad \text{(A.32)}$$

using the calibrated value of p_b^{HH}, the constrained value of $p_c^H = 0.25$, and the factor ζ_b^H to

Table A.8: Single-tag and double-tag correct-sign probabilities P_f^s and P_f^d used in the A_b fit. The quoted errors are due only to the statistical uncertainty of the calibrated probabilities. Also shown are the Monte Carlo expectations.

flavor	MC P_f^s	calibrated P_f^s	MC P_f^d	calibrated P_f^d
b	0.8033	0.8168±0.0049	0.9459	0.9545±0.0029
c	0.303	0.25	0.086	0.10

convert p_b^{HH} into a value suitable for single-tagged events. The calculated values of P_f^s and P_f^d are summarized in Table A.8, along with the expectations from the simulation.

Appendix B

Tagging Correlations

It is useful to investigate the sources of the tagging correlations ξ_f^t and the single/double correct-sign probability corrections ζ_f^t, to ensure that they are well-modeled in the simulation and so that appropriate systematic errors can be evaluated. A procedure will be described that allows the estimation of the contribution from an individual source. The significant sources will be enumerated, and a completeness test will be presented showing that these sources account for the total effect. Procedures to estimate the systematic uncertainties for each source will also be described.

B.1 Source Estimation

To estimate the contribution from a source, each hemisphere of the event is characterized by a variable x_i $(i = 1, 2)$ which probes that source. For example, x_i could be the energy of the heavy hadron in hemisphere i.

For the tagging correlations ξ_f^t, the necessary items are a parameterization $\epsilon_f^t(x)$ of the tag efficiency for all f event hemispheres, the normalized distribution $N_f(x)$ of x in all f event hemispheres, and the normalized distribution $N_f^t(x)$ of x in f event hemispheres opposite those tagged as t. The correlation due to a particular source can then be computed from:

$$\xi^t_{f,x} = \frac{\int \epsilon^t_f(x) N^t_f(x)dx}{\int \epsilon^t_f(x) N_f(x)dx} = \frac{\int \epsilon^t_f(x) N^t_f(x)dx}{\epsilon^t_f} \tag{B.1}$$

where $\xi^t_{f,x}$ is the correlation due only to the source probed by x.

For the correct-sign probability corrections ζ^t_f, the ingredients are a parameterization $p^t_f(x)$ of the correct-sign probability in all t-tagged f event hemispheres, the normalized distribution $N^{tt}_f(x)$ of x in t-tagged f event hemispheres opposite those tagged as t, and the normalized distribution $N^{t\not{t}}_f(x)$ of x in t-tagged f event hemispheres opposite those not tagged as t. The single/double correction due to a particular source can then be computed from:

$$\zeta^t_{f,x} = \frac{\int p^t_f(x) N^{t\not{t}}_f(x)dx}{\int p^t_f(x) N^{tt}_f(x)dx} \tag{B.2}$$

where $\zeta^t_{f,x}$ is the single/double correction due only to the source probed by x.

B.2 Sources

Four significant sources have been found and are detailed below.

B.2.1 CRID uptime

For the L tag, the efficiency depends upon whether the CRID is active. When the CRID is on the efficiency will be higher, as there is a second way (Q_K) to sign the tag. Therefore, if one hemisphere has been L tagged there is a greater chance that the other will also be tagged, since in these events the CRID is more often active. The ingredients for this source are shown in Figure B.1, where $x = 1$ if the CRID is active and $x = 0$ when it is turned off.

Figure B.1: Parameterizations and distributions used in estimating the contributions from CRID uptime. Top row is for the L tag, bottom row is for the H tag.

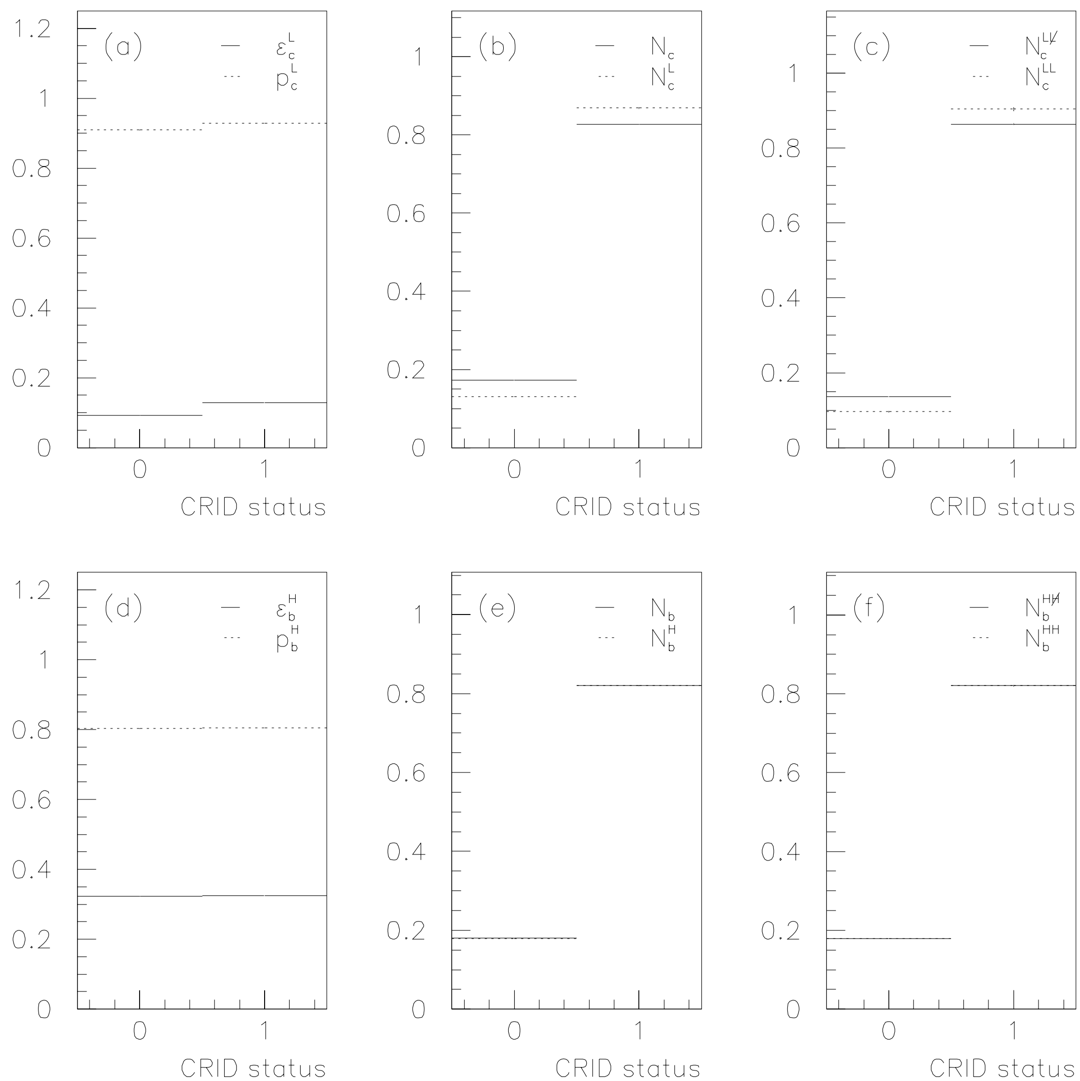

B.2.2 Same-hemisphere Hadron Production

The most important source, particularly for the single/double corrections, is events which have both heavy hadrons produced in the same hemisphere with respect to the thrust axis. These are caused by the emission of energetic gluon radiation and suppressed by the cut on the thrust magnitude, but still present in the sample. The ingredients for this source are shown in Figure B.2, where x is the number of heavy hadrons in a hemisphere.

B.2.3 Hadron Energy Correlation

The energies of the two heavy hadrons in the event are correlated through the emission of gluon radiation. The ingredients for this source are shown in Figure B.3, where x is the energy of the heavy hadron in a hemisphere. In order to avoid overestimating this effect the events with both hadrons in the same hemisphere are removed before estimating this source.

B.2.4 Polar Angle Correlation

The two hadrons generally are produced back-to-back in polar angle, which introduces a tagging correlation due to the limited acceptance of the detector. The ingredients for this source are shown in Figure B.4, where x is the cosine of the polar angle of the heavy hadron in the hemisphere.

B.3 Correlation Source Results

The contributions to ξ_f^t and ζ_f^t from each source are shown in Table B.1. The sum of the four contributions is also compared to the totals obtained directly from the simulation, and seen to be in good agreement in all cases.

Figure B.2: Parameterizations and distributions used in estimating the contributions from same-hemisphere hadron production. Top row is for the L tag, bottom row is for the H tag.

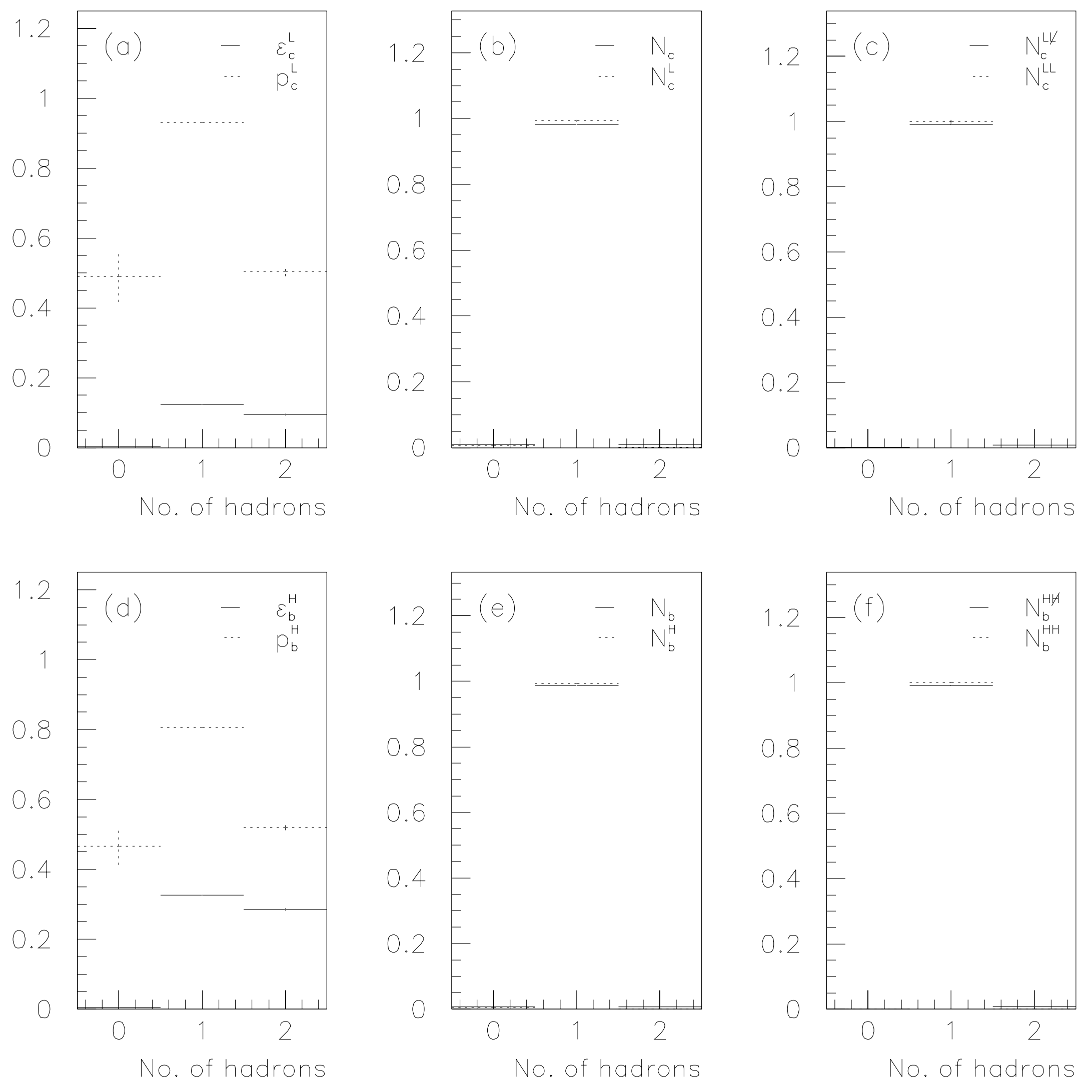

Figure B.3: Parameterizations and distributions used in estimating the contributions from hadron energy correlation. Top row is for the L tag, bottom row is for the H tag.

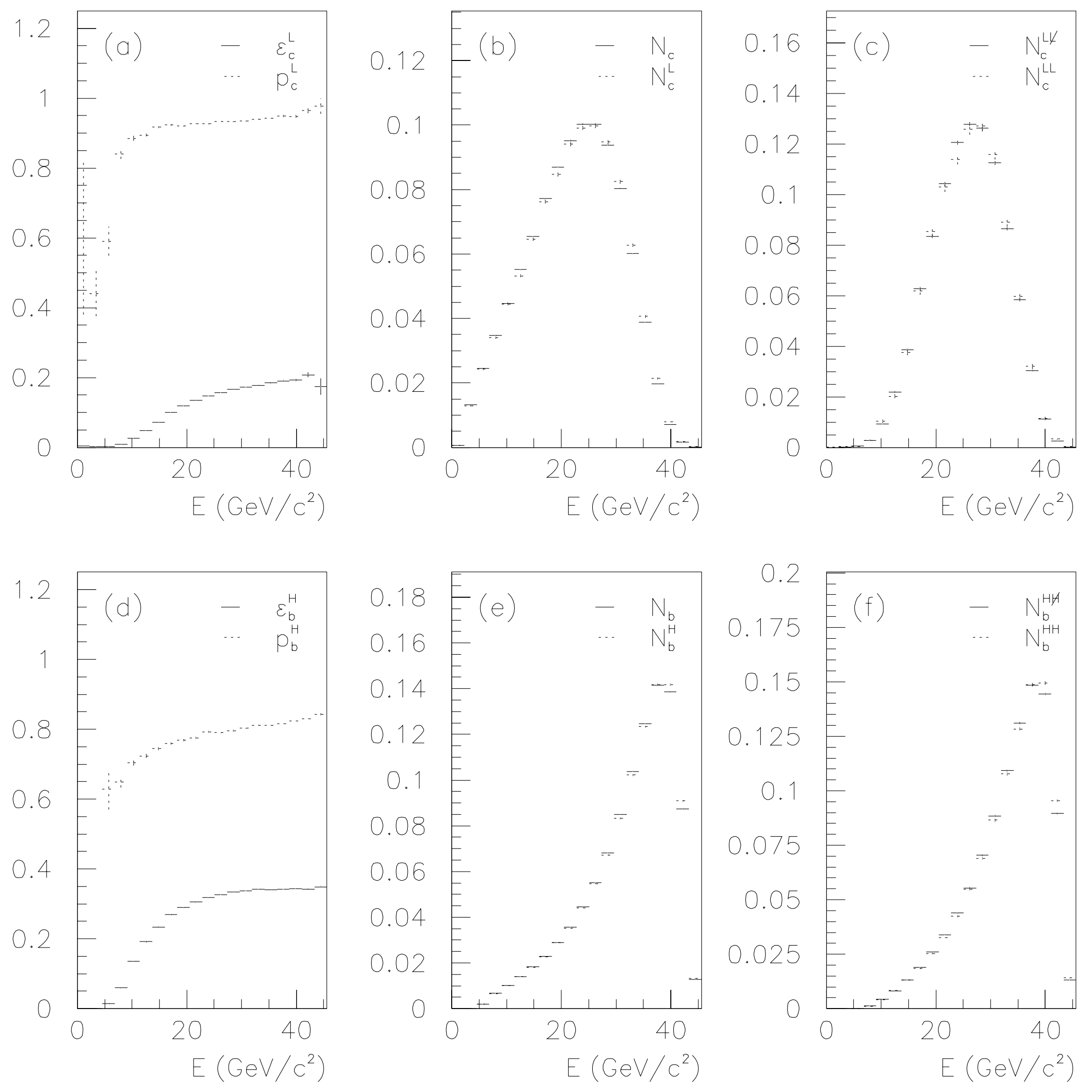

Figure B.4: Parameterizations and distributions used in estimating the contributions from polar angle correlation. Top row is for the L tag, bottom row is for the H tag.

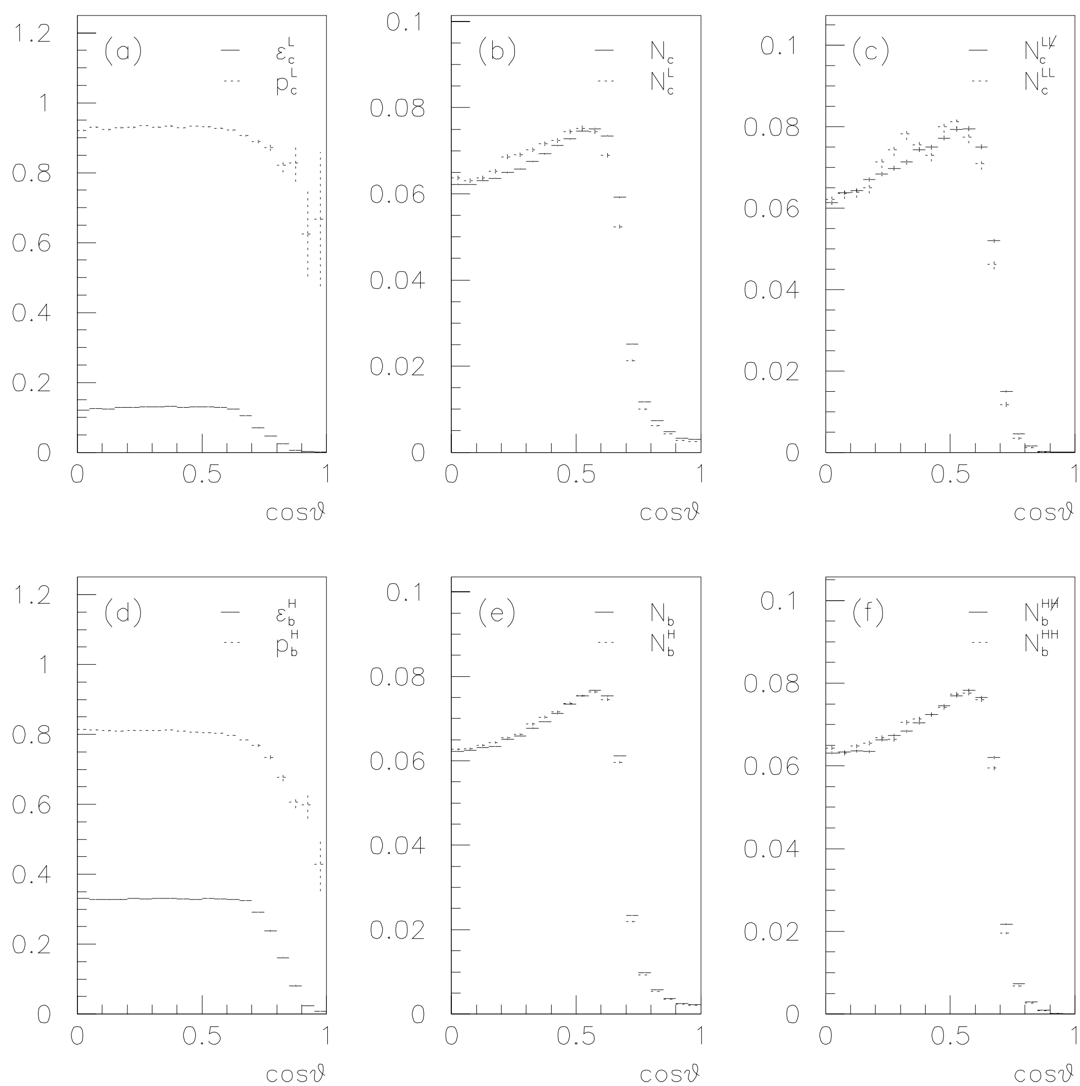

Table B.1: Summary of the contributions of the correlation sources, along with their sums. Also shown for comparison are the direct determinations of the correlation parameters.

source	$\xi^L_{c,x}-1$ (%)	$\xi^H_{b,x}-1$ (%)	$\zeta^L_{c,x}-1$ (%)	$\zeta^H_{b,x}-1$ (%)
CRID uptime	1.20	0.00	-0.08	-0.00
same-hemisphere hadrons	0.38	0.16	-0.35	-0.30
hadron energy correlation	0.74	0.05	-0.02	-0.05
polar angle correlation	0.70	0.09	-0.05	-0.04
sum	3.02	0.30	-0.50	-0.39
direct	2.91±0.70	0.45±0.19	-0.69±0.15	-0.50±0.11

B.4 Systematic Uncertainties

For the four significant sources, it is desirable to verify that the simulation is properly modeling the effects, and to set reasonable variations for the purposes of estimating systematic errors. For the CRID uptime, this involves simply checking that the simulated CRID-on fraction is the same as in the data. The polar angle contributions are assumed to be strictly detector effects, which are already included in the tracking efficiency and resolution systematic errors. This leaves the same-hemisphere hadrons and hadron energy sources, which depend upon the JETSET parton shower model. Because these have never been measured, techniques for constraining them from the data has been developed. These techniques are not true measurements but only simple checks.

B.4.1 Same-hemisphere Hadron Production

The SLD simulation indicates that 2.82%(2.45%) of $c(b)$ events have both heavy hadrons in the same hemisphere. To check the simulation against the data, samples of three-jet events were selected in both. The Durham algorithm [56] was used, with parameter $y = 0.015$. Charged tracks were used as input, and each jet was required to have $|\cos\theta_{JET}| < 0.75$ to permit tagging. No cut on the thrust magnitude T was imposed. The secondary vertex search and track attachment procedure was performed on the set of tracks assigned to each

Figure B.5: Distributions of ϕ_{12}.

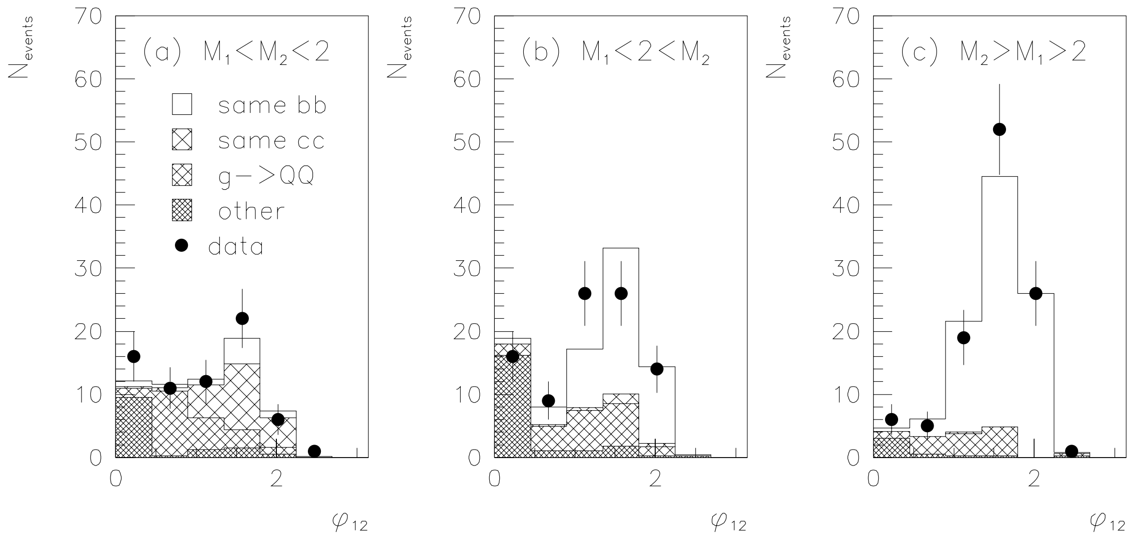

of the three jets, and the p_t-corrected mass M_{jet} was computed for each jet with a secondary vertex. Events with two jets in the same hemisphere w.r.t. the thrust axis $\hat{t}$, with $M_{jet} > 0.5$ GeV/c^2 in both, and with no secondary vertex in the third jet were considered candidates for same-hemiphere heavy hadron production. To separate c from b the events were split into three classes (M_1 is the lesser of the two M_{jet}): $M_1 < M_2 < 2$, $M_1 < 2 < M_2$, and $M_2 > M_1 > 2$. Within each of these classes the angle ϕ_{12} between the two found secondary vertices gives additional information about the type of event. Four types were considered: same-hemisphere primary $c\bar{c}$ production, same-hemisphere primary $b\bar{b}$ production, events with a $g \to c\bar{c}$ or $g \to b\bar{b}$ pair, and "other" which are mostly one B decay which has been split into two jets by the jet finder.

Distributions of ϕ_{12} for each of the four event types were obtained from the simulation and normalized by the total number of three-jet events in the data. A fit to the data ϕ_{12} distributions was performed to find scale factors for each component. The fitted and data ϕ_{12} distributions are shown in Figure B.5, and the results of the fit are given in Table B.2.

The "other" rate is consistent with the data, and the $g \to c\bar{c}, b\bar{b}$ rate is consistent with

Table B.2: Results of the fit to the ϕ_{12} distributions.

event type	$s = N_{fit}/N_{MC}$
same hemisphere $b\bar{b}$	0.82±0.09
same hemisphere $c\bar{c}$	1.15±0.37
event with $g \to c\bar{c}, b\bar{b}$	1.57±0.42
other	1.14±0.24

the adjustment required to match the simulation to the current world average rates. For the same hemisphere $c\bar{c}$ rate, the simulated rate was varied by ±40% to estimate a systematic error. Because the Monte Carlo rate for same hemisphere $b\bar{b}$ events is not as consistent with the data, a conservative variation of ±30% was applied to the simulated rate.

B.4.2 Hadron Energy Correlation

The SLD simulation generates heavy hadrons with energy correlation $\gamma_E = \langle E_1 E_2 \rangle / \langle E \rangle^2 = 1.014$, for both c and b events. This is in excellent agreement with an $\mathcal{O}(\alpha_s^2)$ calculation [57]. Appropriate uncertainties were determined by comparing the simulation and data. Samples of double-tagged events were selected, with the charged vertex momentum P_{hem} used as an energy estimate. The quantity $\gamma_P = \langle P_1 P_2 \rangle / \langle P \rangle^2$ was computed for both the simulation and the data, and the results compared. To isolate c events, both hemispheres were required to have $y_{hem} < 0.3$. This tighter cut relative to the L-tag is used because b background biases the extracted γ_P. For b events a cut of $y_{hem} > 0.85$ was used. The values of γ_P observed in the Monte Carlo and data are summarized in Table B.3. The Monte Carlo is in good agreement with the data, although the errors are large and the tagging efficiency and energy resolution significantly dilute the observed correlation. In order to vary the observed Monte Carlo γ_P values within the uncertainties on the data values, the true Monte Carlo correlations γ_E were varied by ±0.026 for c and ±0.003 for b. These variations were then used to estimate systematic errors for A_c and A_b.

Table B.3: The $\gamma_P - 1$ correlation parameters observed in the Monte Carlo and data.

	$y_{hem} < 0.3$	$y_{hem} > 0.85$
Monte Carlo $\gamma_P - 1$ (%)	0.46±0.17	0.72±0.06
data $\gamma_P - 1$ (%)	0.52±0.43	0.69±0.13

Appendix C

The SLD Collaboration

Kenji Abe,[15] Koya Abe,[24] T. Abe,[21] I. Adam,[21] H. Akimoto,[21] D. Aston,[21]
K.G. Baird,[11] C. Baltay,[30] H.R. Band,[29] T.L. Barklow,[21] J.M. Bauer,[12]
G. Bellodi,[17] R. Berger,[21] G. Blaylock,[11] J.R. Bogart,[21] G.R. Bower,[21] J.E. Brau,[16]
M. Breidenbach,[21] W.M. Bugg,[23] D. Burke,[21] T.H. Burnett,[28] P.N. Burrows,[17]
A. Calcaterra,[8] R. Cassell,[21] A. Chou,[21] H.O. Cohn,[23] J.A. Coller,[4]
M.R. Convery,[21] V. Cook,[28] R.F. Cowan,[13] G. Crawford,[21] C.J.S. Damerell,[19]
M. Daoudi,[21] N. de Groot,[2] R. de Sangro,[8] D.N. Dong,[21] M. Doser,[21] R. Dubois,[21]
I. Erofeeva,[14] V. Eschenburg,[12] S. Fahey,[5] D. Falciai,[8] J.P. Fernandez,[26] K. Flood,[11]
R. Frey,[16] E.L. Hart,[23] K. Hasuko,[24] S.S. Hertzbach,[11] M.E. Huffer,[21] X. Huynh,[21]
M. Iwasaki,[16] D.J. Jackson,[19] P. Jacques,[20] J.A. Jaros,[21] Z.Y. Jiang,[21]
A.S. Johnson,[21] J.R. Johnson,[29] R. Kajikawa,[15] M. Kalelkar,[20] H.J. Kang,[20]
R.R. Kofler,[11] R.S. Kroeger,[12] M. Langston,[16] D.W.G. Leith,[21] V. Lia,[13] C. Lin,[11]
G. Mancinelli,[20] S. Manly,[30] G. Mantovani,[18] T.W. Markiewicz,[21] T. Maruyama,[21]
A.K. McKemey,[3] R. Messner,[21] K.C. Moffeit,[21] T.B. Moore,[30] M. Morii,[21]
D. Muller,[21] V. Murzin,[14] S. Narita,[24] U. Nauenberg,[5] H. Neal,[30] G. Nesom,[17]
N. Oishi,[15] D. Onoprienko,[23] L.S. Osborne,[13] R.S. Panvini,[27] C.H. Park,[22]
I. Peruzzi,[8] M. Piccolo,[8] L. Piemontese,[7] R.J. Plano,[20] R. Prepost,[29]
C.Y. Prescott,[21] B.N. Ratcliff,[21] J. Reidy,[12] P.L. Reinertsen,[26] L.S. Rochester,[21]
P.C. Rowson,[21] J.J. Russell,[21] O.H. Saxton,[21] T. Schalk,[26] B.A. Schumm,[26]
J. Schwiening,[21] V.V. Serbo,[21] G. Shapiro,[10] N.B. Sinev,[16] J.A. Snyder,[30]
H. Staengle,[6] A. Stahl,[21] P. Stamer,[20] H. Steiner,[10] D. Su,[21] F. Suekane,[24]

A. Sugiyama,[15] S. Suzuki,[15] M. Swartz,[9] F.E. Taylor,[13] J. Thom,[21] E. Torrence,[13] T. Usher,[21] J. Va'vra,[21] R. Verdier,[13] D.L. Wagner,[5] A.P. Waite,[21] S. Walston,[16] A.W. Weidemann,[23] E.R. Weiss,[28] J.S. Whitaker,[4] S.H. Williams,[21] S. Willocq,[11] R.J. Wilson,[6] W.J. Wisniewski,[21] J.L. Wittlin,[11] M. Woods,[21] T.R. Wright,[29] R.K. Yamamoto,[13] J. Yashima,[24] S.J. Yellin,[25] C.C. Young,[21] H. Yuta.[1]

(The SLD Collaboration)

[1] *Aomori University, Aomori , 030 Japan,*
[2] *University of Bristol, Bristol, United Kingdom,*
[3] *Brunel University, Uxbridge, Middlesex, UB8 3PH United Kingdom,*
[4] *Boston University, Boston, Massachusetts 02215,*
[5] *University of Colorado, Boulder, Colorado 80309,*
[6] *Colorado State University, Ft. Collins, Colorado 80523,*
[7] *INFN Sezione di Ferrara and Universita di Ferrara, I-44100 Ferrara, Italy,*
[8] *INFN Lab. Nazionali di Frascati, I-00044 Frascati, Italy,*
[9] *Johns Hopkins University, Baltimore, Maryland 21218-2686,*
[10] *Lawrence Berkeley Laboratory, University of California, Berkeley, California 94720,*
[11] *University of Massachusetts, Amherst, Massachusetts 01003,*
[12] *University of Mississippi, University, Mississippi 38677,*
[13] *Massachusetts Institute of Technology, Cambridge, Massachusetts 02139,*
[14] *Institute of Nuclear Physics, Moscow State University, 119899, Moscow Russia,*
[15] *Nagoya University, Chikusa-ku, Nagoya, 464 Japan,*
[16] *University of Oregon, Eugene, Oregon 97403,*
[17] *Oxford University, Oxford, OX1 3RH, United Kingdom,*
[18] *INFN Sezione di Perugia and Universita di Perugia, I-06100 Perugia, Italy,*
[19] *Rutherford Appleton Laboratory, Chilton, Didcot, Oxon OX11 0QX United Kingdom,*
[20] *Rutgers University, Piscataway, New Jersey 08855,*
[21] *Stanford Linear Accelerator Center, Stanford University, Stanford, California 94309,*
[22] *Soongsil University, Seoul, Korea 156-743,*
[23] *University of Tennessee, Knoxville, Tennessee 37996,*
[24] *Tohoku University, Sendai 980, Japan,*
[25] *University of California at Santa Barbara, Santa Barbara, California 93106,*
[26] *University of California at Santa Cruz, Santa Cruz, California 95064,*
[27] *Vanderbilt University, Nashville,Tennessee 37235,*
[28] *University of Washington, Seattle, Washington 98105,*
[29] *University of Wisconsin, Madison,Wisconsin 53706,*
[30] *Yale University, New Haven, Connecticut 06511.*

Bibliography

[1] T. D. Lee and C. N. Yang, "Question of parity conservation in weak interactions," *Phys. Rev.* **104** (1956) 254–258.

[2] C. S. Wu, E. Ambler, R. W. Hayward, D. D. Hoppes, and R. P. Hudson, "Experimental test of parity conservation in beta decay," *Phys. Rev.* **105** (1957) 1413–1414.

[3] R. L. Garwin, L. M. Lederman, and M. Weinrich, "Observations of the failure of conservation of parity and charge conjugation in meson decays: The magnetic moment of the free muon," *Phys. Rev.* **105** (1957) 1415–1417.

[4] F. J. Hasert *et al.*, "Search for elastic muon neutrino electron scattering," *Phys. Lett.* **B46** (1973) 121–124.

[5] C. Y. Prescott *et al.*, "Parity non-conservation in inelastic electron scattering," *Phys. Lett.* **B77** (1978) 347–352.

C. Y. Prescott *et al.*, "Further measurements of parity nonconservation in inelastic electron scattering," *Phys. Lett.* **B84** (1979) 524.

[6] A. Argento *et al.*, "Electroweak asymmetry in deep inelastic muon - nucleon scattering," *Phys. Lett.* **B120** (1983) 245.

[7] W. Heil *et al.*, "Improved limits on the weak, neutral, hadronic axial vector coupling constants from quasielastic scattering of polarized electrons," *Nucl. Phys.* **B327** (1989) 1–31.

[8] P. A. Souder *et al.*, "Measurement of parity violation in the elastic scattering of polarized electrons from C_{12}," *Phys. Rev. Lett.* **65** (1990) 694–697.

[9] C. S. Wood *et al.*, "Measurement of parity nonconservation and an anapole moment in cesium," *Science* **275** (1997) 1759.

[10] P. A. Vetter, D. M. Meekhof, P. K. Majumder, S. K. Lamoreaux, and E. N. Fortson, "Precise test of electroweak theory from a new measurement of parity nonconservation in atomic thallium," *Phys. Rev. Lett.* **74** (1995) 2658–2661.

[11] R. Carr *et al.*, "A precision measurement of the weak mixing angle in Møller scattering," SLAC-PROPOSAL-E-158, 1997.

[12] S. L. Glashow, "Partial symmetries of weak interactions," *Nucl. Phys.* **22** (1961) 579–588.

[13] S. Weinberg, "A model of leptons," *Phys. Rev. Lett.* **19** (1967) 1264–1266.

[14] A. Salam in *Elementary Particle Theory*, N. Svartholm, ed., p. 367. Almqvist and Wiksell, Stockholm, 1968.

[15] F. Halzen and A. D. Martin, *Quarks and Leptons: an introductory course in modern particle physics.* Wiley, 1984.

[16] D. Griffiths, *Introduction to Elementary Particles.* Harper and Row, 1987.

[17] **Super-Kamiokande** Collaboration, Y. Fukuda *et al.*, "Evidence for oscillation of atmospheric neutrinos," *Phys. Rev. Lett.* **81** (1998) 1562–1567.

[18] **SNO** Collaboration, Q. R. Ahmad *et al.*, "Measurement of the charged current interactions produced by B_8 solar neutrinos at the Sudbury Neutrino Observatory,".

[19] P. W. Higgs, "Broken symmetries, massless particles and gauge fields," *Phys. Lett.* **12** (1964) 132–133.

P. W. Higgs, "Broken symmetries and the masses of gauge bosons," *Phys. Rev. Lett.* **13** (1964) 508–509.

[20] P. Clarke, "An introduction to cross-sections and asymmetries measurable using polarized beams in high-energy e^+e^- colliders," RAL-90-055, 1990.

[21] **Particle Data Group** Collaboration, D. E. Groom *et al.*, "Review of particle physics," *Eur. Phys. J.* **C15** (2000) 1.

[22] "SLAC linear collider conceptual design report," SLAC-R-229, 1980.

[23] T. Limberg, P. Emma, and R. Rossmanith, "The north arc of the SLC as a spin rotator." Presented at 1993 Particle Accelerator Conference (PAC 93), Washington, DC, 17-20 May 1993.

[24] **SLD** Collaboration, K. Abe *et al.*, "A high-precision measurement of the left-right Z boson cross-section asymmetry," *Phys. Rev. Lett.* **84** (2000) 5945–5949.

[25] H. R. Band, P. C. Rowson, and T. R. Wright, "The positron polarization (POSIPOL) experiments: T-419," SLD Note 268, 2000.

[26] H. R. Band, G. Mitchell, R. Prepost, and T. R. Wright, "A Møller polarimeter for high energy electron beams," *Nucl. Instrum. Meth.* **A400** (1997) 24–33.

[27] **SLD** Collaboration, "SLD design report," SLAC-R-273, 1984.

[28] K. Abe *et al.*, "Design and performance of the SLD vertex detector, a 307 Mpixel tracking system," *Nucl. Instrum. Meth.* **A400** (1997) 287–343.

[29] M. D. Hildreth *et al.*, "Performance of the SLD central drift chamber," *IEEE Trans. Nucl. Sci.* **42** (1995) 451.

M. J. Fero *et al.*, "Performance of the SLD central drift chamber," *Nucl. Instrum. Meth.* **A367** (1995) 111–114.

[30] P. Billoir, "Track fitting with multiple scattering: A new method," *Nucl. Instr. Meth.* **A225** (1984) 352.

[31] M. Cavalli-Sforza *et al.*, "Construction and testing of the SLD Cerenkov ring imaging detector," *IEEE Trans. Nucl. Sci.* **37** (1990) 1132–1141.

[32] T. Sjostrand, "High-energy physics event generation with PYTHIA 5.7 and JETSET 7.4," *Comput. Phys. Commun.* **82** (1994) 74–90.

[33] P. Burrows and H. Masuda, "An optimised QCD parameter set for the JETSET 7.4 Monte Carlo program," SLD Physics Note 36, 1995.

[34] B. Andersson, G. Gustafson, G. Ingelman, and T. Sjostrand, "Parton fragmentation and string dynamics," *Phys. Rept.* **97** (1983) 31.

[35] C. Peterson, D. Schlatter, I. Schmitt, and P. Zerwas, "Scaling violations in inclusive e^+e^- annihilation spectra," *Phys. Rev.* **D27** (1983) 105.

[36] **CLEO** Collaboration, "QQ - the CLEO event generator," http://www.lns.cornell.edu/public/CLEO/soft/QQ.

[37] R. Brun, F. Bruyant, M. Maire, A. C. McPherson, and P. Zanarini, "GEANT: Detector description and simulation tool," CERN-DD/EE/84-1, 1987.

[38] P. N. Burrows, H. Park, K. T. Pitts, and J. M. Yamartino, "Estimate of combined triggering and selection efficiency for hadronic events," SLD Note 229, 1993.

[39] B. Denby, "Neural networks in high energy physics: A ten year perspective," *Comput. Phys. Commun.* **119** (1999) 219.

[40] A. Zell, G. Mamier, M. Vogt, N. Mache, R. Hübner, S.Doering, *et al.*, "SNNS user manual, version 4.1," Universität Stuttgart, Fakultät Informatik, Report No. 6/95, 1995. See http://www-ra.informatik.uni-tuebingen.de/SNNS/.

[41] D. J. Jackson, "A topological vertex reconstruction algorithm for hadronic jets," *Nucl. Instrum. Meth.* **A388** (1997) 247–253.

[42] J. L. Wittlin, *A Measurement of the Time Dependence of $B_d - \bar{B}_d$ Mixing with Kaon Tagging*. PhD thesis, University of Massachusetts, 2001.

[43] S. Catani and M. H. Seymour, "Corrections of $O(\alpha_s^2)$ to the forward-backward asymmetry," *JHEP* **07** (1999) 023.

[44] **LEP Heavy Flavor Working Group** Collaboration, D. Abbaneo *et al.*, "QCD corrections to the forward-backward asymmetries of c and b quarks at the Z pole," *Eur. Phys. J.* **C4** (1998) 185–191.

[45] **LEP Electroweak Working Group** Collaboration, D. Abbaneo *et al.*, "A combination of preliminary electroweak measurements and constraints on the Standard Model," CERN-EP-2000-016, 2000.

[46] D. Bardin *et al.*, "ZFITTER v.6.21: A semi-analytical program for fermion pair production in e^+e^- annihilation," *Comput. Phys. Commun.* **133** (2001) 229–395.

[47] **LEP Electroweak Working Group** Collaboration, D. Abbaneo *et al.*, "A combination of preliminary electroweak measurements and constraints on the Standard Model," Summer 2001 edition, in preparation. See http://lepewwg.web.cern.ch/LEPEWWG/.

[48] **LEP Heavy Flavor Working Group** Collaboration, D. Abbaneo *et al.*, "Input parameters for the LEP/SLD electroweak heavy flavour results for Summer 1998 conferences," LEPHF/98-01, 1998.

[49] **SLD** Collaboration, K. Abe *et al.*, "Measurement of A_b and A_c from the left-right forward-backward asymmetry of leptons in hadronic events at the Z^0 resonance," *Phys. Rev. Lett.* **74** (1995) 2895–2899.

SLD Collaboration, K. Abe *et al.*, "Direct measurement of A_b and A_c at the Z^0 pole using a lepton tag," *Phys. Rev. Lett.* **83** (1999) 3384–3389.

[50] **SLD** Collaboration, K. Abe *et al.*, "Measurement of A_c with charmed mesons at SLD," *Phys. Rev.* **D63** (2001) 032005.

[51] **SLD** Collaboration, K. Abe *et al.*, "Measurement of A_b from the left-right forward-backward asymmetry of b quark production in Z^0 decays using a momentum weighted track charge technique," *Phys. Rev. Lett.* **74** (1995) 2890–2894.

[52] **SLD** Collaboration, K. Abe *et al.*, "Direct measurement of A_b in Z^0 decays using charged kaon tagging," *Phys. Rev. Lett.* **83** (1999) 1902–1907.

[53] H. Burkhardt and B. Pietrzyk, "Update of the hadronic contribution to the QED vacuum polarization," LAPP-EXP-2001-03, 2001.

[54] A. D. Martin, J. Outhwaite, and M. G. Ryskin, "A new determination of the QED coupling $\alpha(m_Z^2)$ lets the Higgs off the hook," *Phys. Lett.* **B492** (2000) 69–73.

[55] **LEP Higgs Working Group** Collaboration, "Search for the Standard Model Higgs boson at LEP," LHWG Note/2001-03, 2001.

[56] S. Catani, Y. L. Dokshitzer, M. Olsson, G. Turnock, and B. R. Webber, "New clustering algorithm for multi-jet cross-sections in e^+e^- annihilation," *Phys. Lett.* **B269** (1991) 432–438.

[57] P. Nason and C. Oleari, "Next-to-leading-order corrections to momentum correlations in $Z \to b\bar{b}$," *Phys. Lett.* **B407** (1997) 57–60.